공학박사 학위논문

Photophysical Studies of Photoinduced Charge Generation in Organic Solar Cells using Time-Resolved Spectroscopy

시간 분해 분광법을 이용한 유기태양전지의 광유도 전하 생성에 대한 광물리적 연구

2021 년 8 월

서울대학교 대학원

재료공학부

정 혜 연

Photophysical Studies of Photoinduced Charge Generation in Organic Solar Cells using Time-Resolved Spectroscopy

A THESIS SUBMITTED IN PARTIAL FULFILLMENT OF
THE REQUIREMENTS FOR THE DEGREE OF
DOCTOR OF PHILOSOPHY
IN ENGINEERING AT THE GRADUATE SCHOOL OF
SEOUL NATIONAL UNIVERSITY

AUGUST 2021

By
Hae Yeon Chung

Supervisor
Prof. Soo Young Park

Photophysical Studies of Photoinduced Charge Generation in Organic Solar Cells using Time-Resolved Spectroscopy

시간 분해 분광법을 이용한 유기태양전지의 광유도 전하 생성에 대한 광물리적 연구

지도 교수 박 수 영

이 논문을 공학박사 학위논문으로 제출함

2021 년 8 월

서울대학교 대학원

재료공학부

정 혜 연

정혜연의 공학박사 학위논문을 인준함

2021 년 7 월

위 원 장 _____ 이 태 우

부위원장 _____ 박 수 영

위 원 _____ 김 동 호

위 원 _____ 이 관 형

위 원 _____ 권 민 상

Abstract

Photophysical Studies of Photoinduced Charge Generation in Organic Solar Cells using Time-Resolved Spectroscopy

Hae Yeon Chung

Department of Materials Science and Engineering

The Graduate School

Seoul National University

Organic semiconducting materials have attracted a lot of attention as an alternative to the silicon-based semiconductors due to the various advantages such as low cost fabrication, flexibility, chemical versatility and so on. Based on their advantages of organic semiconductors, various optoelectronic applications have been developed, of which organic solar cells (OSCs) have drawn significant interest as a promising device for the next generation of energy conversion during last the two decades. The structure of OSCs consists of a stack of multi-layers between two electrodes, of which the light absorbing photoactive layer is the bulk heterojunction (BHJ) of the donor (D) and acceptor (A) materials for obtaining high performance OSCs. During the operation of OSCs, each step in the photoinduced processes such as light absorption, charge transfer, charge transport and recombination in the photoactive layer has a great influence on the efficiency of devices, which are affected by several factors such as the optical and electrical properties of organic semiconducting materials, energy levels, and D/A blend

morphology.

In particular, photoinduced charge generation in the photoactive layer has a significant effect on the photocurrent in OSCs. Despite the importance of the charge separation process, there is still a lack of a comprehensive study of photophysical processes of charge separation and still room for the spectroscopic study on the charge separation mechanism and its effect on the performance of photovoltaic devices. Hence, in this research, the photophysical study was performed on the photoinduced charge separation mechanism of OSCs according to various material structures using time-resolved spectroscopy. Using various donor and acceptor organic semiconducting materials, the effects on the charge separation and following device performances were investigated, and the structural characteristics of materials required to implement high efficiency OSCs were explored.

First, to confirm the efficient way of assembling electron-donating and accepting moieties on the push-pull type small molecule donor materials, two triad donor molecules were synthesized and characterized. ADA and DAD type triad donor molecules using indolo[3,2-b]indole (IDID) and diketopyrrolopyrrole (DPP) as electron-donating and accepting units, respectively, were used with fullerene acceptor ($PC_{61}BM$) in OSCs. The structural differences between ADA and DAD lead to different interactions with surrounding materials and the following the symmetry-breaking charge transfer characteristics. Consequently, the ADA type small molecule donor material exhibited stronger intramolecular charge transfer (ICT) characteristics due to its spatially more

delocalized lowest unoccupied molecular orbital (LUMO). Much enhanced polaron generation and reduced charge carrier recombination were exhibited at the D/A interface, resulting in the higher short-circuit current (J_{SC}) and power conversion efficiency (PCE) in the ADA:$PC_{61}BM$ devices than DAD:$PC_{61}BM$ OSCs. (Chapter 2)

Next, to understand the charge separation mechanism in polymer solar cells (PSCs) in the view point of the ICT characteristics of excitons and the role of excess energy, push-pull type copolymer (PTB7) and homopolymer (P3HT) were used as a donor polymer with highly crystalline nonfullerene acceptor (NIDCSEO3) in PSCs. PTB7 exhibited delocalized excitons with ICT characteristics due to the alternating electron donating and accepting units, and therefore, ultrafast charge separation through the hot charge transfer (CT) state is dominant pathway for the polaron generation at the D/A interface. On the other hand, P3HT exhibited delocalized excitons which relaxed to the polaron pair state within ultrafast time range. Namely, the charge separation of P3HT:NIDCSEO3 is the combined system of hot and relaxed charge generation through the polaron pair and relaxed CT states. Consequently, PTB7:NIDCSEO3 PSC exhibited higher device performances with hot exciton dissociation dominant charge separation, which is favorable for the photocurrent generation due to the suppressed charge recombination through the relaxed CT state. (Chapter 3)

Lastly, I compared the blend morphology and the excited state dynamics to determine the effect of the polymer aggregation property on the device performances in PSCs by using two push-pull type polymers (PBDCS, PBDS) with different aggregation

properties and two acceptors (fullerene acceptor, $PC_{71}BM$, and nonfullerene acceptor, ITIC). Blend morphology differs significantly depending on the presence of aggregation promotor of the polymer (β-cyano groups in PBDCS) and aggregating and percolating properties of acceptors. Therefore, the excited state dynamics and following device performances are also greatly influenced by the chemical structure of donor and acceptor materials. PBDCS-based PSCs exhibited delayed charge generation with suppressed charge recombination due to the pure domain system, leading to high photovoltaic performances with the PCEs of 8.75 and 7.81% for PBDCS:$PC_{71}BM$ and PBDCS:ITIC PSCs, respectively. On the other hand, PBDS-based PSCs exhibited largely different excited state dynamics and photovoltaic properties depending on the acceptor materials with the PCEs of 5.00 and 0.76% for PBDS:$PC_{71}BM$ and PBDS:ITIC PSCs, respectively. In particular, PBDS:ITIC PSC exhibited ultrafast charge generation with greatly enhanced charge recombination due to the extremely intermixed blend morphology, resulting in poor device performance. These results indicate that the blend morphology has a remarkably important effect on the device properties of PSCs, and the polymer possessing aggregating property is a key factor for the ideal blend morphology for high efficiency PSCs. (Chapter 4)

Keyword: organic semiconductor, organic solar cells, transient absorption spectroscopy, photoinduced charge separation, charge recombination, small molecule donor, polymer aggregation, intramolecular charge transfer characteristics

Student Number: 2015-30185

Contents

List of Tables

List of Figures

Chapter 1. Introduction

1.1. Organic semiconducting materials

Organic semiconducting materials have been interested with the several advantages such as low cost, flexibility, and easy processability for the solution processing for the device fabrication compared to the inorganic semiconductors. Organic semiconducting materials are mostly composed of electronically bound carbon (C) and hydrogen (H) atoms, and often contain other atoms such as nitrogen (N), sulfur (S), oxygen (O), and halogen (F, Cl) atoms. Since the electrical conductivity in polyacetylene was discovered by Shirakawa, MacDiarmid, and Heeger in the 1970s, there has been increasing interest in organic semiconductors. [1-2] And with the development of organic semiconducting materials, three researchers won the Nobel Prize in the 2000s. The rapid development of organic semiconducting materials has opened broad opportunities for organic electronics. Furthermore, as the organic semiconductors can be applied to a variety of industrial field, organic semiconducting materials with various optical and electronic properties suitable for application to the organic optoelectronic devices, such as organic light-emitting diodes (OLEDs), [3-4] organic solar cells (OSCs), [5-8] and organic field-effect transistors (OFETs) [9-12] have been designed and synthesized. Despite the development of organic materials, the demand for novel materials showing better

performance is continuously required due to the lower efficiency than silicon-based devices, and new materials with superior optical and electronic properties are being developed through various design rules. In addition, research on the development of organic materials is also being conducted through the study on the device physics of various organic optoelectronic devices.

1.1.1. Electronic properties of π-conjugated organic materials

π-conjugated organic materials are composed of the alternating single and double bonds between carbon atoms and exhibit electronic conductivity due to π-bonding between carbon atoms. The carbon atom in the ground state has an electronic configuration of $1s^2 2s^2 2p^2$. Carbon atom can form single, double, or triple bonds with another carbon atoms, and in an organic materials, the atomic orbitals are mixed together to form molecular hybrid states such as sp^3, sp^2, sp hybridized orbitals. For example, in methane, CH_4, the carbon atom may form the sp^3 hybridized orbitals combined by three 2p orbitals with one 2s orbital, possessing tetrahedrally coordinated structure and forming sigma (σ)-bond with hydrogen atoms. On the other hand, hybridized sp^2 orbital is formed by combining two 2p orbitals and one 2s orbital, possessing equivalent energy state and shape of hybridized orbitals. Unhybridized p_z orbital of the carbon atom is perpendicular to the triangular sp^2 orbital plane, and the pi (π)-bond is formed due to the

overlap of the unhybridized p_z orbitals, resulting in the electron wave function delocalization and the electrical conductivity in organic semiconducting materials. The mixing of a 2s orbital and a 2p orbital of the same atom also creates the hybridization of atomic orbitals, forming two sp hybrid orbitals, where two sp orbitals have a linear arrangement with the angle of 180° between two orbitals.

Hückel theory can explain the formation of molecular orbitals and determine the energy of the π-molecular orbitals in a conjugated system. When the unhybridized p_z orbitals overlap, the combination of atomic orbitals creates molecular orbitals, yielding the formation of two energy levels (a π bonding orbital and a π^* antibonding orbital) and delocalized π-electrons through the conjugated backbone. The accumulation of π bonding brings the highest occupied molecular orbital (HOMO) and the lowest unoccupied molecular orbital (LUMO) with the energy difference (bandgap, E_g) between HOMO and LUMO energy levels. Upon the absorption of a photon with the energy higher than bandgap, an exciton is formed with Coulombically bound electron and hole pair. The bandgap between HOMO and LUMO is the minimum energy required for the excitation of ground state chromophore, and determined by the distribution of delocalized electron cloud, or the conjugation length through the backbone of organic molecules. The conjugation length is controlled by several functional groups substituted to the backbone structure and the amount of the planarization of the backbone structure. Furthermore, intermolecular or interchain coupling in solid state also affects the electron

cloud in the molecule and following the HOMO, LUMO energy levels and bandgap energy of the organic materials. In order of 1-3 eV of bandgap, organic materials exhibit semiconducting properties, where the orbital bandgap for the silicon is 1.1 eV. [13-14]

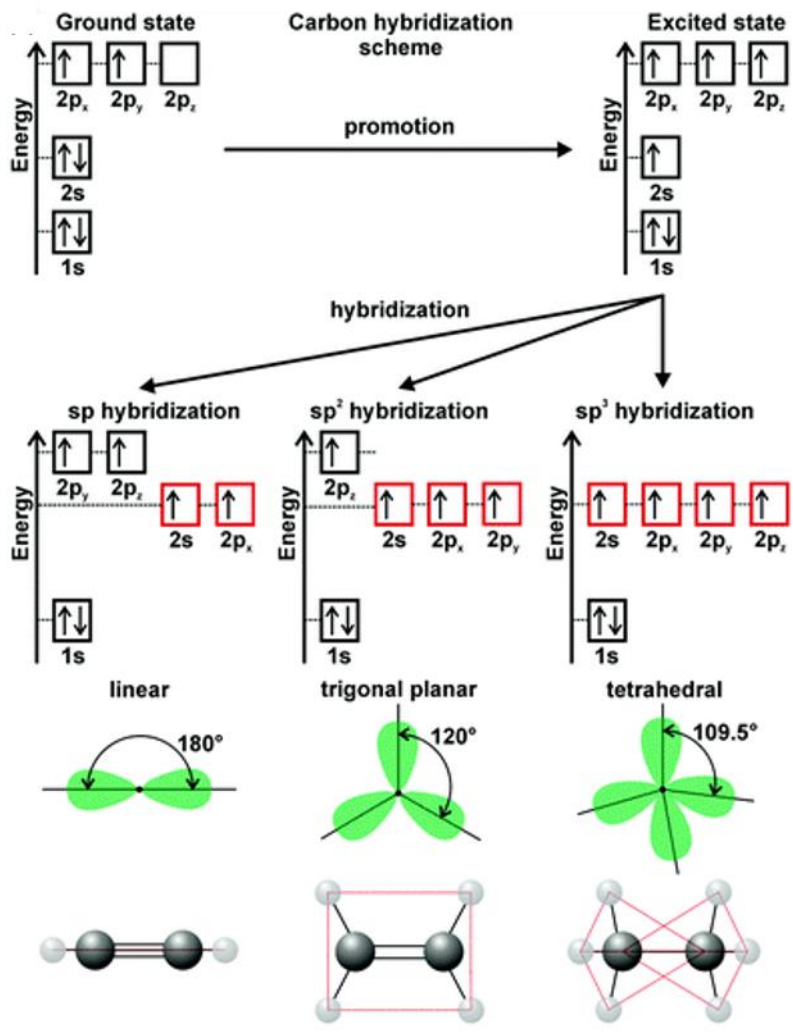

Figure 1-1 Schematic description of sp, sp^2, and sp^3 hybridization in carbon atoms. [15]

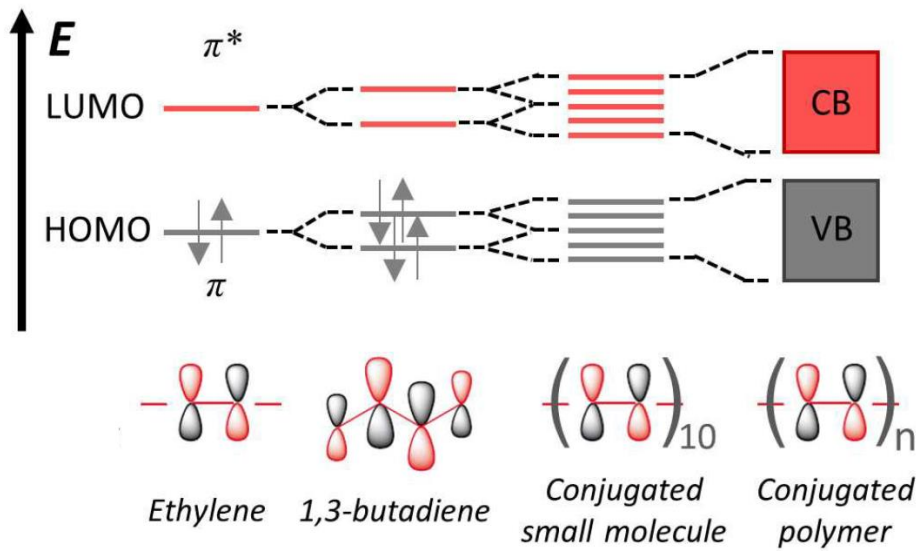

Figure 1-2 An extension of molecular orbitals to long conjugated polymers. [16]

1.1.2. Typical donor and acceptor materials

Researches on the development of organic semiconducting materials have been conducted for decades based on the requirement of high performance optoelectronic devices. Homopolymers such as poly(3-hexylthiophene) (P3HT) and poly(2-methoxy-5-(2-ethylhexyloxy)-1,4-phenylenevinylene) (MEH-PPV) have been widely used for the organic optoelectronics for decades. [17-20] In particular, P3HT has been used as the model compound for the OSCs since the first synthesis of regioregular P3HT because of their advantages such as high crystallinity and high mobility. [21-22] Recently, D-A type (push-pull) organic materials consisting of electron-donating and accepting units have been developed for easy modification of energy levels and light absorbing property. The D-A structure induces the hybridization of the molecular orbital between donor and acceptor units, resulting in the low bandgap energy, which makes it easy to use in various optoelectronic devices. For the polymer and/or small molecule donor materials, several characteristics are required for obtaining high performance OSCs: low bandgaps for the broad absorption range, crystalline properties for the high charge carrier mobility, and appropriate HOMO/LUMO energy levels for efficient charge transfer with the high value of V_{OC}. The development of donor materials has been focused on satisfying these requirements. On the other hand, while the electron donating materials have been actively developed in previous decades, research has been conducted on nonfullerene

acceptor materials possessing various structures rather than fullerene-based acceptor materials in recent years. Compared to fullerene acceptors, newly developed nonfullerene acceptors exhibit easier synthetic routes, tunable optical and electrical properties with superior thermal and photostability. Such developments of donor and acceptor organic materials improve the device performances by changing various optical and electronic properties of the organic photoactive layer used in OSCs. Commonly used donor and acceptor materials showing high photovoltaic efficiencies are as shown in Figure 1-4, 1-5, and 1-6.

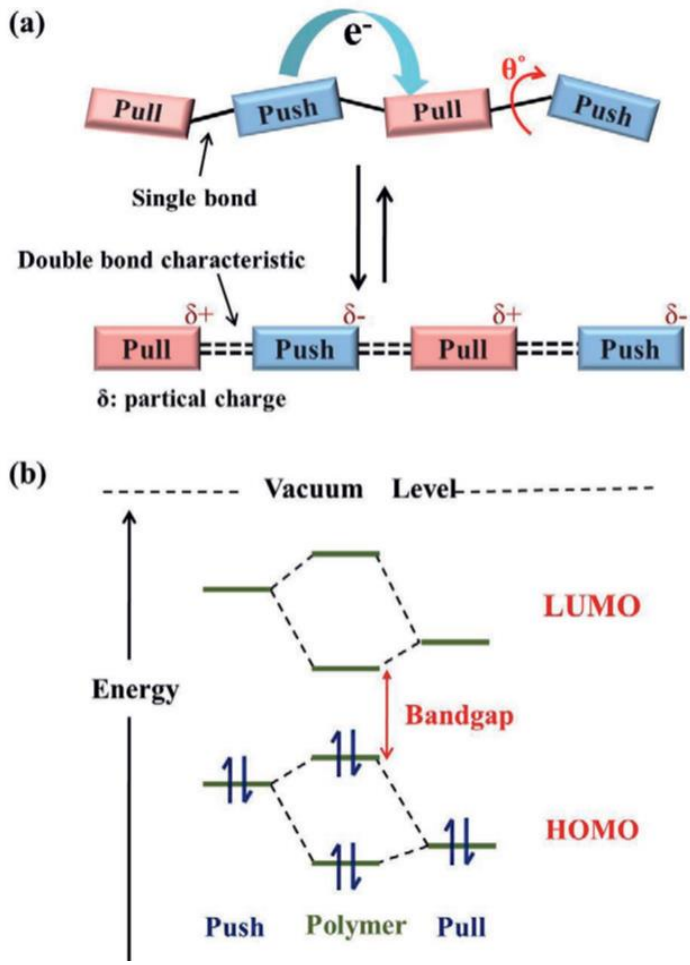

Figure 1-3 (a) Delocalization of electrons and (b) energy levels of push and pull units and the band gap of a push-pull polymer. [14]

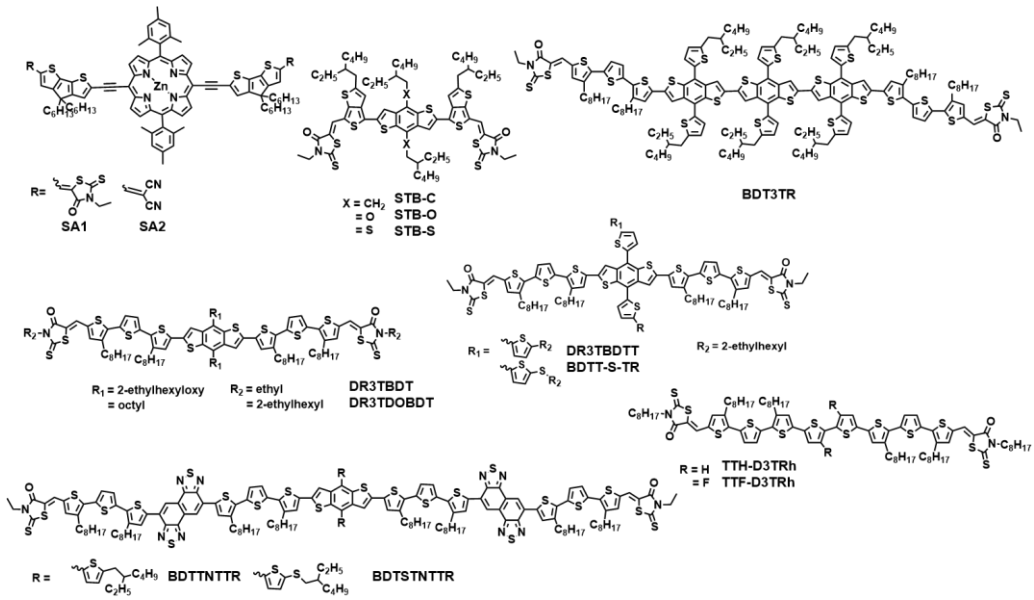

Figure 1-4 Molecular structures of small molecule donors.

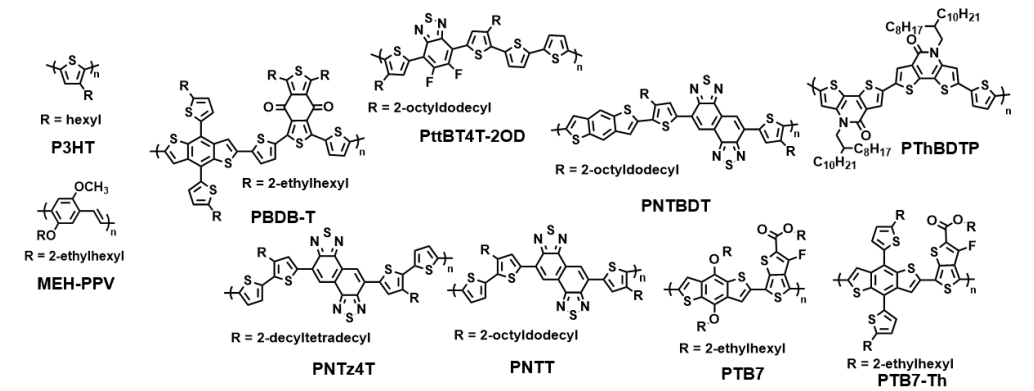

Figure 1-5 Molecular structures of polymer donors.

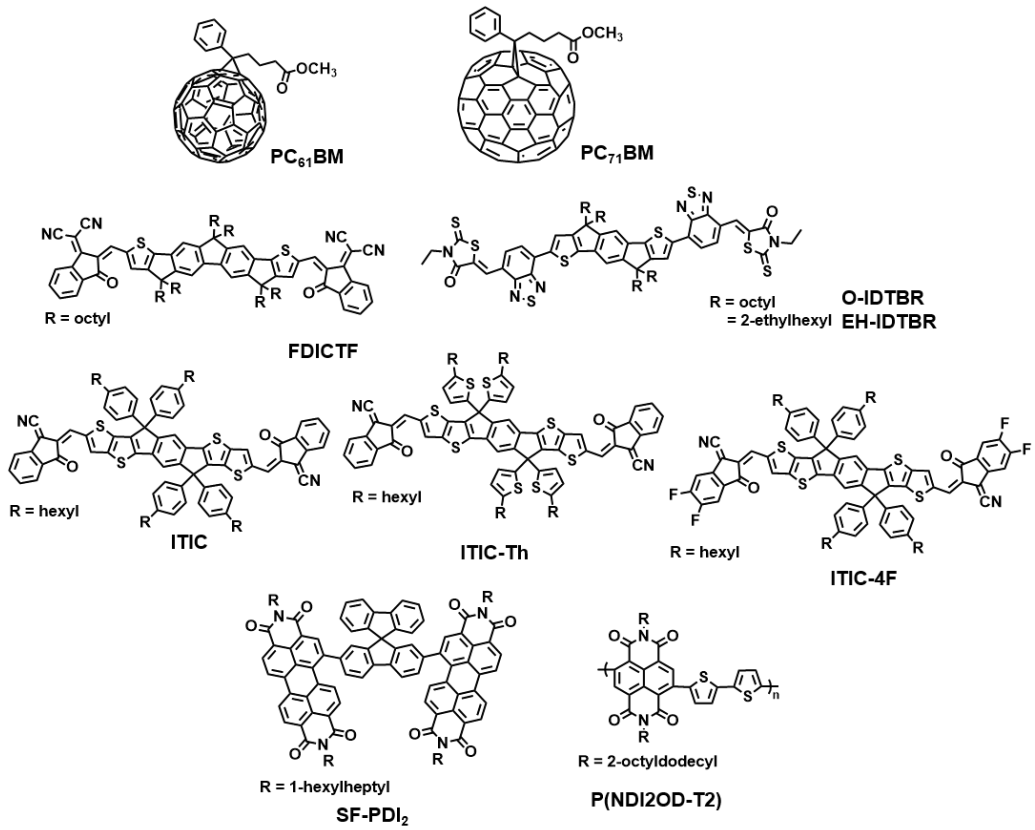

Figure 1-6 Molecular structure of fullerene and nonfullerene acceptors.

1.2. Organic solar cells

The demand for alternative and renewable energy sources rather than fossil fuels has led to the development of photovoltaic devices. The photovoltaic effect is a physical process that generates the voltage or current from the sunlight in a photovoltaic cell. This phenomenon was discovered by the French physicist, E. Becquerel in 1839. [23] After that, silicon-based photovoltaics have been developed for a long time since 1954, and crystalline silicon solar cells have been used in commercial markets with high efficiency of over 26%. [24] However, due to the limitations of silicon-based solar cells such as high price and weight, the need to develop new technologies such as organic photovoltaic devices has been raised. In line of this trend, OSC has been studied based on a number of advantages such as low price, easy processability, transparency and mechanical flexibility compared to silicon-based solar cells. Significant progress has been made through extensive research on OSCs in various respects, achieving power conversion efficiencies (PCEs) of over 18%. [25] However, the efficiency of OSCs is still lower than that of silicon-based solar cells, and research is still needed from various perspectives on organic material designs and device architectures.

1.2.1. Device architecture

Due to the strongly bound electron-hole pair, the electric field of the two electrodes is not sufficient to generate exciton dissociation, and the single layer structure of OSC does not effectively work and has very low efficiencies (<1%). [26] The bilayer OSC has two layers of donor and acceptor materials between the electrodes, and the exciton dissociation occurs at the interface of donor and acceptor layers. However, the bilayer structure OSCs exhibited also low efficiencies (~1 %) because the exciton diffusion length is about 10 nm in organic materials, and the excitons cannot be effectively diffused to the electrodes. [27] Therefore, bulk heterojunction (BHJ) type OSC structures are used for efficient exciton dissociation and diffusion in the photoactive layer of OSCs, where the donor and acceptor materials are mixed with the nanoscale phase separation. [28] BHJ OSCs are composed of a structure in which several layers are stacked on the transparent substrate, and there are two configurations: a conventional and inverted device structure using an ITO-based electrode. The conventional structure of OSC is composed of glass/ITO/hole transport layer (HTL)/photoactive layer/electron transport layer (ETL)/Al using low work function metal as a top electrode, while the inverted structure of OSC consists of glass/ITO/ETL/photoactive layer/HTL/Ag using high work function metal as a top electrode. Interlayers are adopted between the electrode and photoactive layer for interface engineering and efficient charge transport. In general, metal oxide such as V_2O_5, MoO_3, WO_3, NiO) and organic layer PEDOT:PSS are used as HTL, while metal oxide such as TiOx, ZnO and low work function metal/metal compound (Ca or LiF) are used as ETL for more efficient electron extraction. With these

architecture of OSCs, charge carriers separated from the excitons in photoactive layer can transport in the opposite direction through the interlayers and be collected at the electrodes that generates photocurrent in the circuit.

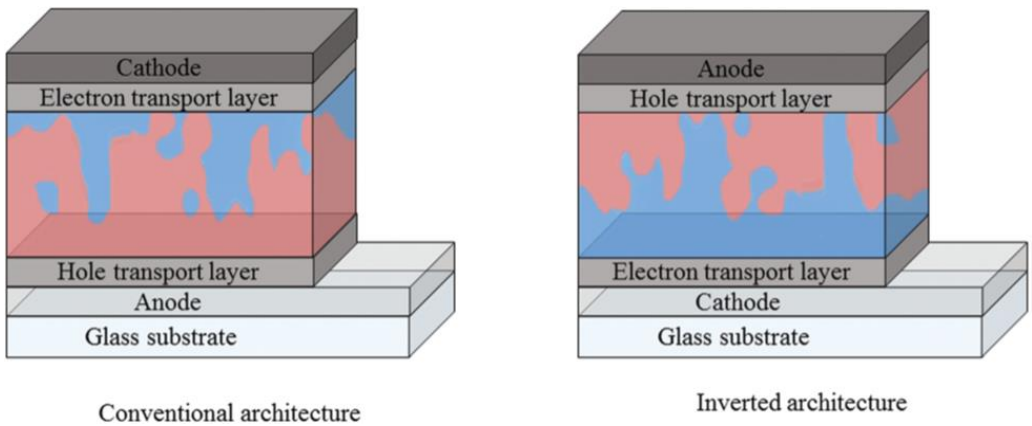

Figure 1-7 Conventional and inverted architectures of bulk heterojunction organic solar cells. [29]

1.2.2. Device characterization

The performance of OSC is characterized by the photocurrent–voltage (*J*–*V*) curve, and the power conversion efficiency (PCE) is affected by the parameters such as the short-circuit current (J_{SC}), open-circuit voltage (V_{OC}) and fill factor (FF) as following equation:

$$\text{PCE } (\eta_e) = \frac{P_{max}}{P_{in}} \times 100\% = \frac{J_{SC} \times V_{OC} \times FF}{P_{in}} \times 100\%$$

, where P_{in} is the incident light power density (commonly, AM 1.5 standardized with the 100 mW/cm^2), and P_{max} is the output power density at the maximum power. [30] Each parameter is influenced by several factors. First, the J_{SC} is the current density at zero bias, which is greatly affected by the optical property of the photoactive layer. When the photoactive layer has high extinction coefficient over a wide wavelength range, a large number of photons are generated with the enhanced light absorption property and the excited state population increases. In addition, donor:acceptor (D:A) blend morphology is also very important for the J_{SC} property as the higher charge generation efficiency at the D/A interface in BHJ and higher charge transport efficiency within the hole and electrode channels result in higher photocurrent in the photovoltaic device.

The V_{OC} is the maximum voltage at zero current, which is influenced by the energy of donor and acceptor materials in the photoactive layer, mainly determined by the HOMO level of the donor and the LUMO level of the acceptor. Furthermore, as the

energetic disorder of BHJ is larger, the distribution of density of state (DOS) is broadened, reducing the V_{OC} in OSCs. In addition, the energy state of CT has recently been found to have a great influence on the V_{OC}, so it is very important to reduce the energy loss originated from radiative/non-radiative recombination.

The FF represents how close the *J*–*V* curve is to a square-shape, which is defined by following equation:

$$\mathrm{FF} = \frac{J_{MP} \times V_{MP}}{J_{SC} \times V_{OC}}$$

, where J_{MP} and V_{MP} represent the current density and voltage at the maximum power point. [30] Furthermore, FF is affected by series resistance (R_s) and shunt resistance (R_{sh}). Therefore, it is necessary to reduce the current leakage by decreasing R_s and increasing R_{sh} by using an appropriate buffer layer between photoactive layer and electrodes. Furthermore, it is also important to increase the charge carrier mobility by increasing the crystallinity of organic materials or forming ideal blend film morphology.

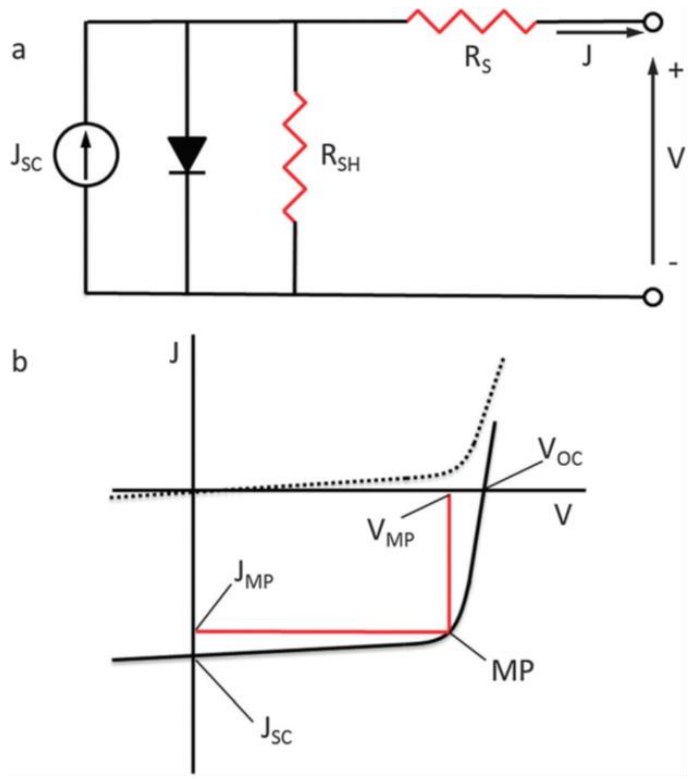

Figure 1-8 (a) Equivalent circuit model for organic solar cell and (b) the current density–voltage (*J*–V) curves of an organic solar cell (⋯: dark, ─: illuminated). [30]

1.2.3. Photophysical processes of organic solar cells

In order to generate electrical current from sunlight, photovoltaic device is required to absorb photon energy and convert photons to free charge carriers to move to the electrodes that generate photocurrent. The operating processes of the OSCs are as follows: i) light absorption and exciton diffusion, ii) exciton dissociation and charge transfer, iii) charge transport and iv) charge recombination.

For the absorption of organic molecules, the molar extinction coefficient is determined by the wave function overlap between the ground and excited electronic states. After photon absorption, excitons are formed according to the molar extinction coefficient of donor and acceptor materials in the photoactive layer and the excitons diffuse to reach the D/A interface. At the interface, exciton dissociation occurs and a Coulombically bound interfacial charge transfer (CT) state is formed through charge transfer between donor and acceptor materials. In the CT state, electron and hole are bound by Coulomb binding energy, where charge carriers exist in each donor and acceptor domain. Free charge carriers are generated by overcoming the binding energy, *V*, as following equation:

$$\mathrm{V} = \frac{e^2}{4\pi\varepsilon_r\varepsilon_0 r}$$

, where e, ε_r, ε_0, and r represent the charge of an electron, dielectric constant of the surrounding medium, permittivity of vacuum, and the electron-hole separation distance.

[31] Otherwise, electron and hole geminately recombine to the ground state. Free charge carriers generated through exciton dissociation transport through the donor and acceptor channels to the electrode. The charge transport ability of BHJ is significantly influenced by the electron and hole mobilities and the blend morphology. Closely packed molecules and highly ordered region are beneficial for the charge transport, and moreover, photocurrent due to efficient charge extraction at the electrode. [32] The recombination of separated free charge carriers is nongeminate recombination. When the charge carriers generated from different excitons meet each other, electron and hole recombine to the ground state, limiting the photocurrent and adversely affecting the device performance.

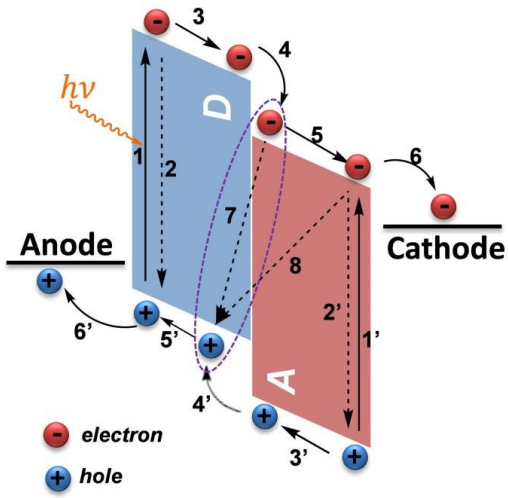

Figure 1-9 The operation principle of organic solar cells: light absorption and exciton formation (1, 1'); intramolecular electron-hole recombination (2, 2'); exciton diffusion (3, 3'); generation of charge transfer (CT) states and CT state dissociation into free charge carriers (4, 4'); charge transport (5, 5'); charge collection at the electrodes (6, 6'); geminate and non-geminate charge recombination (7, 8). [33]

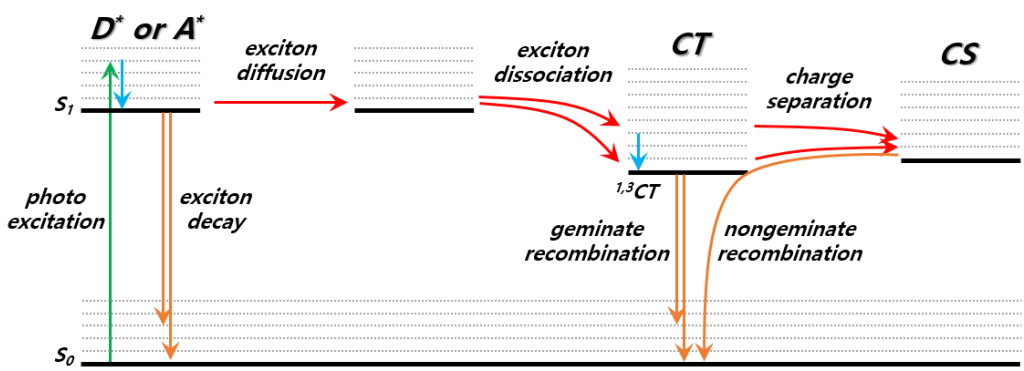

Figure 1-10 Schematic energy diagram of photoinduced charge generation in organic solar cells.

As described above, the operation of OSC is determined by several steps, and high device performance is achieved when charge transfer, transport and extraction occur effectively with suppressed charge recombination. The internal quantum efficiency (IQE) can be presented by the product of the efficiency of each step of operation of OSCs as following equation,

$$\mathrm{IQE} = \eta_{ED} \times \eta_{CT} \times \eta_{CD} \times \eta_{CC}$$

, where η_{ED}, η_{CT}, η_{CD}, η_{CC} represent the efficiencies of exciton diffusion to the D/A interface, charge transfer at the D/A interface, charge dissociation into free charge carriers and the charge collection to the electrodes, respectively. [34]

1.2.4. Models of charge separation and recombination

Considering the kinetic competition between the charge separation and thermal relaxation, there are two theoretical frameworks for the charge separation of OSCs. [35] Firstly, the Onsager-Braun charge separation model describes the process by which the charge separation and geminate recombination are kinetically competing processes. The hot charge transfer states generated by the exciton dissociation are relaxed to the electronically and vibrationally lowest charge transfer states within ultrafast time range (~100 fs). In the relaxed charge transfer states, some fraction of the electron and hole pair separates into free charge carriers. Otherwise, electron and hole geminately

recombine to the ground state. The population change in accordance with the time for each state can be expressed as the following formula:

$$dCT/dt = -k_{CT\rightarrow GS}CT - k_{CT\rightarrow SSC}CT + \gamma SSC^{\lambda+1}$$

$$dSSC/dt = k_{CT\rightarrow SSC}CT - \gamma SSC^{\lambda+1}$$

$$dGS/dt = k_{CT\rightarrow GS}\mathrm{CT}$$

, where *CT*, *SSC*, *GS* are the populations of the charge transfer state, spatially separated charges, and the ground state, $k_{i\rightarrow j}$ represents the rate for the transition from i to j, and γ and λ+1 are the rate constant and the order of the density-dependent (bimolecular) recombination.

The second mechanism is the ultrafast charge separation model, in which the ultrafast charge separation occurs from the hot charge transfer states before the relaxation within the charge transfer states with the aid of the excess energy. In this model, the charge separation occurs within the range of tens to hundreds of femtosecond, leading to the competition between the charge separation and thermal relaxation within charge transfer states. Furthermore, the yield and kinetics of geminate and nongeminate recombination are different in this model. The population change of each state is as follows:

$$dCT/dt = -k_{CT\rightarrow GS}CT$$

$$dSSC/dt = -\gamma SSC^{\lambda+1}$$

$$dGS/dt = k_{CT\rightarrow GS}CT + \gamma SSC^{\lambda+1}$$

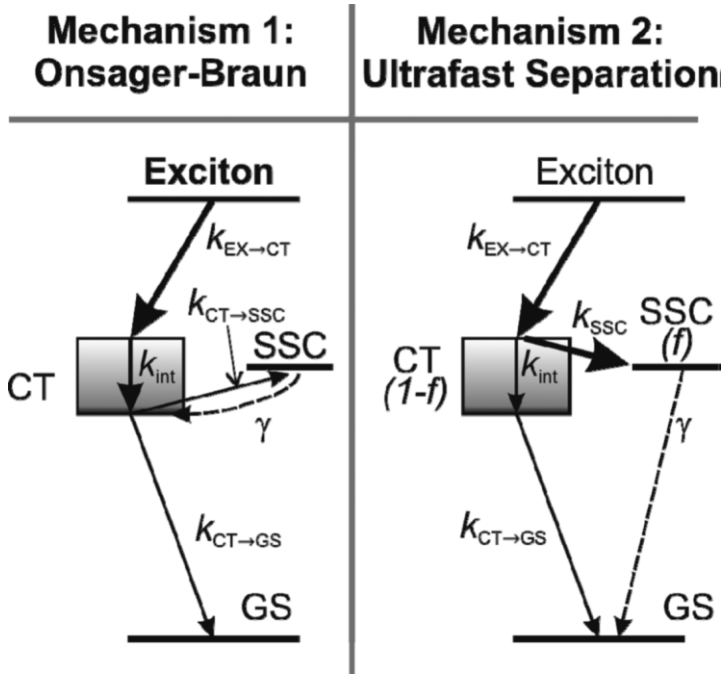

Figure 1-11 Two theoretical frameworks for the charge separation and recombination mechanisms. [35]

1.3. Ultrafast spectroscopy

The temporal scale of different steps in the operation of OSCs varies greatly with each step. [36] The term “ultrafast” refers to a process that occurs within a time range from the femtoseconds (10^{-15} s) to the picosecond (10^{-12} s). The process of exciton generation by light absorption of organic materials occurs on a time scale of femtoseconds (~10^{-15} s). Theoretically, the exciton diffusion can occur within the time range of the exciton lifetime (< 1 ns), but in general, exciton diffusion is limited by the exciton quenching due to charge transfer at the D/A interface, and in the nanoscale phase-separated blend, exciton diffusion occurs within several tens of ps (~ 10^{-11} s). [37] At the interface, exciton dissociation occurs very quickly at several tens of fs (~10^{-14} s), and the generated free charge carriers reach the electrode according to their electron and hole mobilities. Namely, the various steps during the OSC operation occur at various time periods (fs~μs). To determine the dynamics of the excited states, it is important to characterize the electronic properties of the transient excited state, and the research using the time-resolved spectroscopy is a useful and powerful technique for exploring the mechanisms of OSCs.

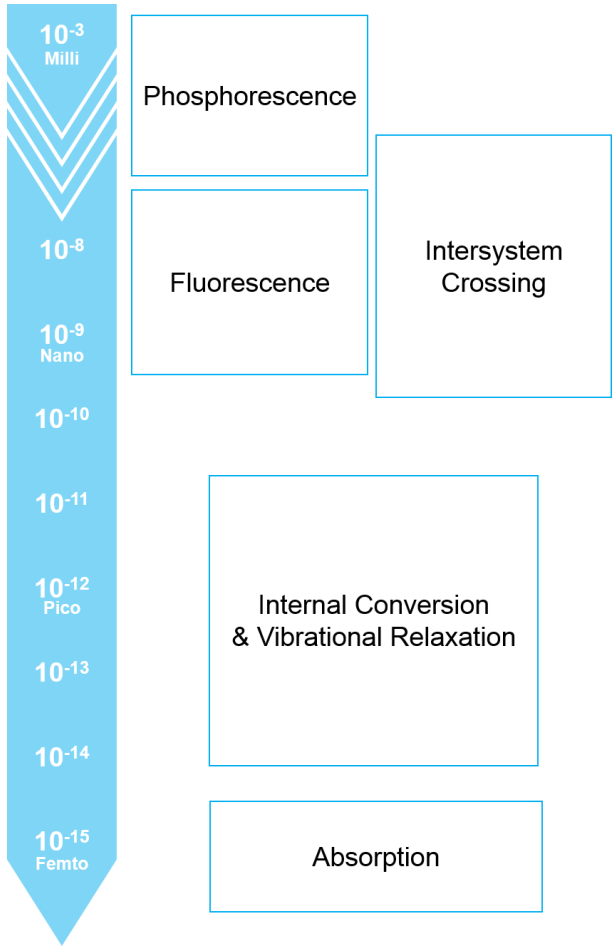

Figure 1-12 Temporal time scales for the photophysical processes in the organic solar cells.

1.3.1. Fundamentals of transient absorption spectroscopy

To explore the excited state dynamics, transient absorption (TA) spectroscopy is one of the most commonly used methods. The femtosecond transient absorption spectrometer is composed of an optical parametric amplifier (OPA) operating at 1 kHz repetition rate and an optical detection system in which two pulse lasers are used for the pump-probe method. [38] First, a pump beam of the intense laser pulse (pulse width ~ 100 fs) is used to excite the ground molecular system to the non-equilibrium state. Ultrashort laser pulses at various wavelengths can be generated, where the fundamental output of the Ti:sapphire laser is 800 nm. The photoinduced processes after the photoexcitation are measured with a white light continuum (WLC) probe beam, which is generated using an optically highly non-linear medium, such as sapphire (α-Al_2O_3) or yttrium aluminum garnet (YAG, $Y_3Al_5O_{12}$) crystals by focusing a small portion of the fundamental 800 nm pulses. Depending on the non-linear crystal and the wavelength of the seed pulse, the probe beam range can be differed. Optical properties are measured using a low intensity laser pulse (probe beam) after a variable delay time between the pump and probe beams. At each delay time, the optical properties are monitored to determine the change of the excited state population after photoexcitation, where the pump pulses were chopped using a chopper and the absorption spectra were saved alternatively with or without pump pulse.

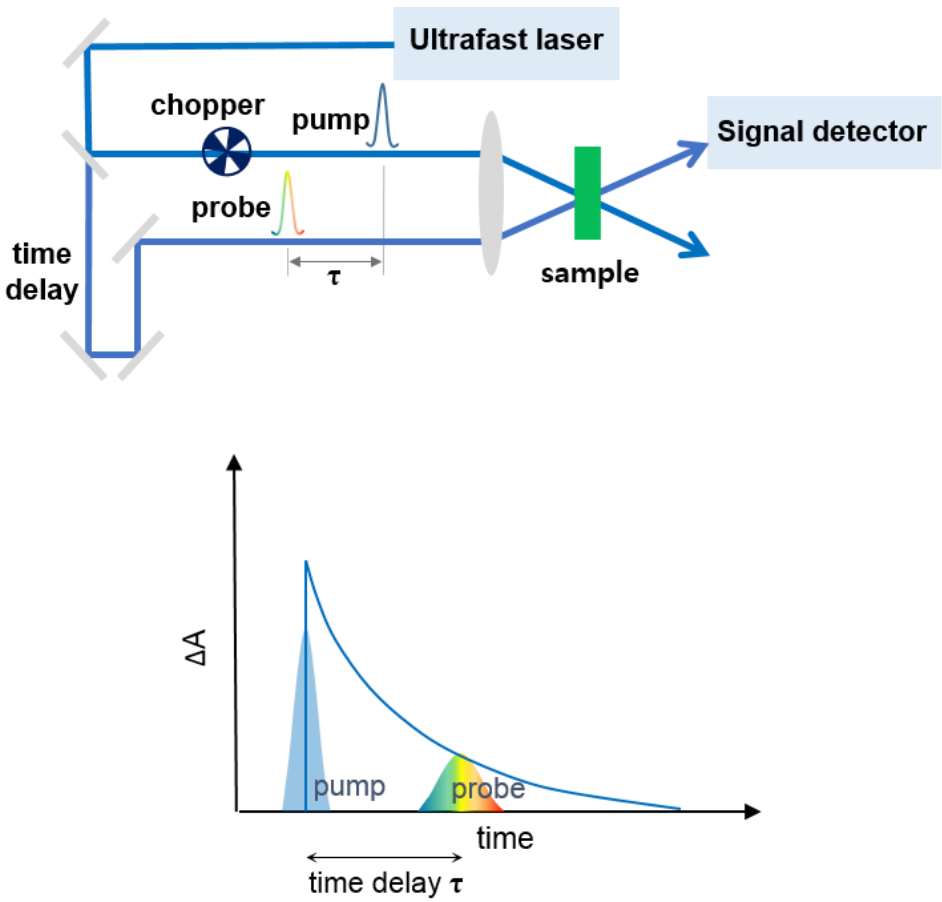

Figure 1-13 (top) schematic depiction of the transient absorption spectroscopy principle and (bottom) decay profile probed at a specific probe wavelength.

1.3.2. Signals in transient absorption spectroscopy

The signal of the TA spectroscopy is described by the change in absorption property. The absorbance at the delay time (τ) is measured by the probe beam, and the incident transmitted light, I, is determined by the Beer-Lambert law as following equation: $A(\tau) = \log(I_0/I)$. As a result of TA measurement, the difference in absorbance (ΔA) between the pump on state and pump off state can be expressed as follows:

$$\Delta A(\lambda, \tau) = \frac{A_{pump\ on}(\lambda, \tau) - A_{pump\ off}(\lambda, \tau)}{A_{pump\ off}(\lambda, \tau)}$$

The optical properties (ΔA) at each delay time consists of the overlapped three spectra: ground-state bleach (GSB), stimulated emission (SE) and excited-state absorption (ESA). [39]

After the excitation, the population of ground state molecules is depleted, resulting in a decrease in ground state absorption than before photoexcitation. Eventually, the negative signal of ΔA appears in the ground state absorption wavelength region, which refers to the ground state bleach.

The second contribution is the stimulated emission, which occurs due to the radiative decay of populated excited state to the ground state. Stimulated emission occurs in the case of an optically allowed transition that appears as a negative signal in ΔA in the same wavelength range as the fluorescence of the excited chromophore.

The third contribution of transient absorption spectra is the excited-state absorption. When the excited states are populated, they can be excited to a higher excited states. This process increases the absorption in the corresponding wavelength region, therefore, resulting in a positive signal in ΔA. Several kinds of excited states, such as higher singlet state, triplet state, CT state, and free charges, generated after photoexcitation can be tracked by analyzing their excited state absorption.

As such, the optical spectrum at each delay time is determined by the contributions. As the signal is related to the population in the excited states, the excited state dynamics can be directly monitored by analyzing the TA spectrum and decay profiles of each species.

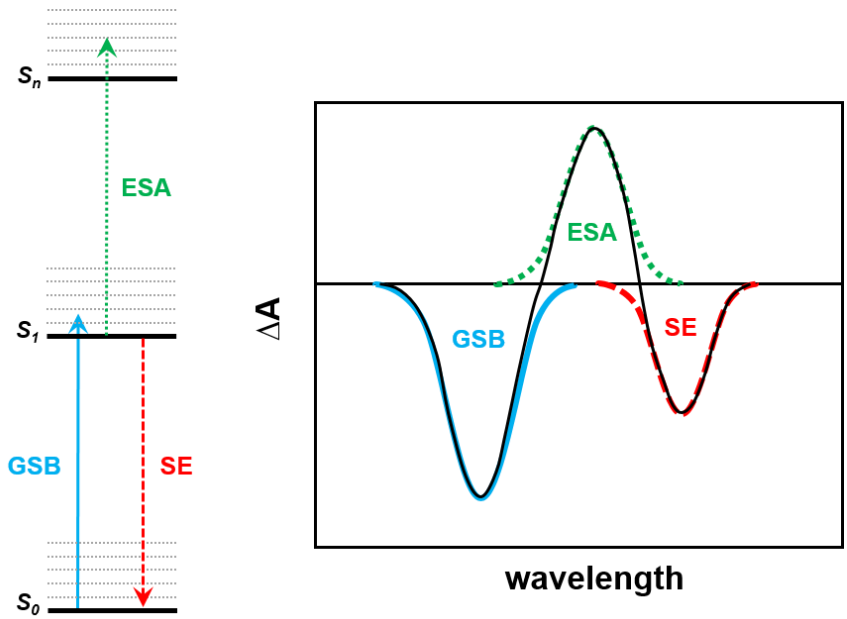

Figure 1-14 (left) Transitions of the ground state bleach (GSB), stimulated emission (SE) and excited state absorption (ESA) and (right) contributions to the transient absorption (ΔA) spectrum.

1.4. Research objective and contents of thesis

In this chapter, an overview of organic semiconducting materials, OSCs, and TA spectroscopy was given. In recent decades, the development of high efficiency OSCs has been conducted along with the development of donor and acceptor using various organic semiconducting materials. Although various factors that affect device efficiency has been studied, there are still rooms for the dynamics of charge generation in the photoactive layer through the spectroscopic analysis and the design rules for the organic semiconducting materials.

In this respect, I will analyze the various charge generation and recombination mechanisms in the photoactive layer using the time-resolved spectroscopy, and propose the detailed relationship between the molecular design of donor and acceptor materials and the device performance in the viewpoint of the photoinduced charge generation and recombination.

In Chapter 2, the intramolecular charge transfer (ICT) characteristics due to the structural difference between the two triad donor materials using the same donor (IDID) and acceptor (DPP) units, and the resulting charge generation at the interface will be presented. Delocalized LUMO and abundant electron density at end-capping DPP moieties of ADA induce stronger ICT characteristics. Due to the stronger ICT characterstics of ADA, larger amount of polaron generation and higher J_{sc} were shown

in ADA:$PC_{61}BM$ OSCs than DAD:$PC_{61}BM$ OSC, indicating ADA as a favorable donor architecture in IDID-DPP systems.

In Chapter 3, the effect of excess energy and the ICT characteristics of polymer excitons on the generation of charge carriers at the interface will be presented when D-A type copolymer and homopolymer donor materials are used with nonfullerene acceptor. PTB7:NIDCSEO3 blend system exhibited temperature independent polaron generation dynamics, indicating hot charge separation dominant pathway due to the delocalized PTB7 exciton with ICT characteristics, and suppressed geminate recombination in PSC. On the other hand, P3HT:NIDCSEO3 system exhibited combined hot and cold charge separation processes due to the ultrafast relaxation to polaron pair and relaxed CT states despite the formation of delocalized P3HT excitons, and P3HT:NIDCSEO3 PSC exhibited a larger degree of geminate recombination and lower J_{SC}. Not only the delocalized state but also the displacement of delocalized charge carriers is important for the charge separation via hot CT state and suppressed geminate recombination in PSCs.

In Chapter 4, the analysis of blend morphology and following device performances will be investigated using two donor – two acceptor system using polymers possessing different aggregation properties with fullerene and nonfullerene acceptors, and the structural characteristics of polymers will be proposed which is required to obtain high efficiency OSCs through the charge generation and recombination in each blend morphology. Strong aggregation property of PBDCS and poor miscibility between PBDCS and acceptors lead to larger domains and the resulting slower charge generation

at the D/A interface in PBDCS:$PC_{71}BM$ and PBDCS:ITIC blends than PBDS blends. However, with suppressed bimolecular/trap-assisted recombination, PBDCS-based PSCs exhibited higher photovoltaic efficiency with higher J_{sc} in both fullerene and nonfullerene acceptor PSCs, indicating the importance of polymer aggregation in the blend morphology, and the following favorable exciton and polaron dynamics in PSCs.

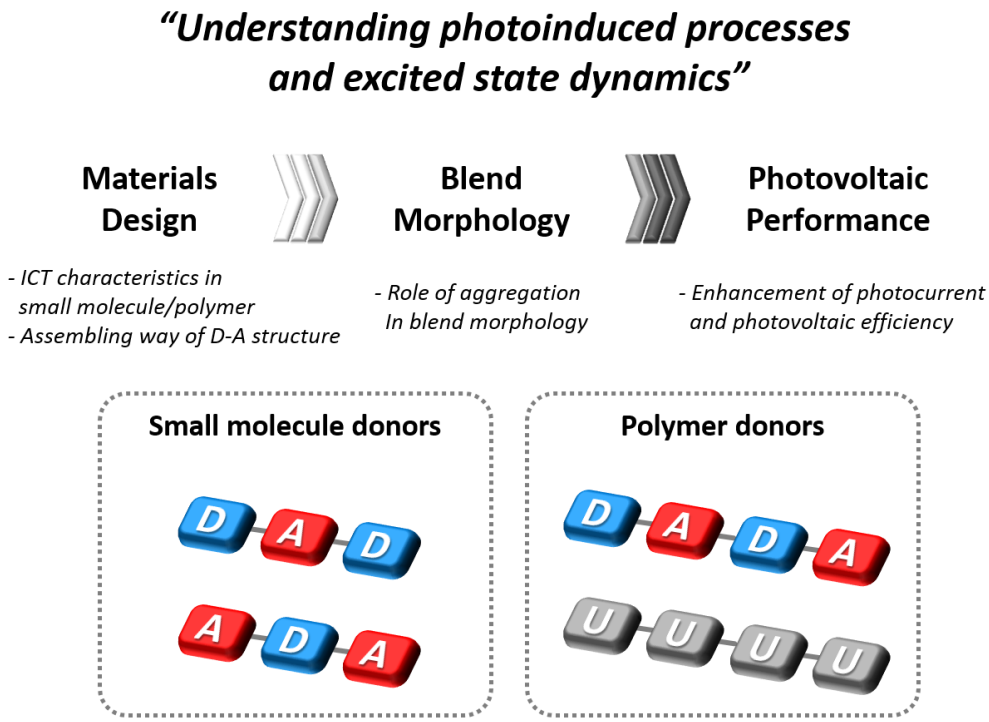

Figure 1-15 Research objective of this thesis.

1.5. References

[1] Shirakawa, H.; Louis, E. J.; MacDiarmid, A. G.; Chiang, C. K.; Heeger, A. J., Synthesis of Electrically Conducting Organic Polymers: Halogen Derivatives of Polyacetylene, (Ch). Journal of the Chemical Society, *Chemical Communications* **1977**, 578-580.

[2] Chiang, C. K.; Fincher, C. R.; Park, Y. W.; Heeger, A. J.; Shirakawa, H.; Louis, E. J.; Gau, S. C.; MacDiarmid, A. G., Electrical Conductivity in Doped Polyacetylene. *Physical Review Letters* **1977**, *39*, 1098-1101.

[3] Burroughes, J. H.; Bradley, D. D. C.; Brown, A. R.; Marks, R. N.; Mackay, K.; Friend, R. H.; Burns, P. L.; Holmes, A. B., Light-Emitting Diodes Based on Conjugated Polymers. *Nature* **1990**, *347*, 539-541.

[4] Kraft, A.; Grimsdale, A. C.; Holmes, A. B., Electroluminescent Conjugated Polymers—Seeing Polymers in a New Light. *Angewandte Chemie International Edition* **1998**, *37*, 402-428.

[5] Sariciftci, N. S.; Smilowitz, L.; Heeger, A. J.; Wudl, F., Photoinduced Electron Transfer from a Conducting Polymer to Buckminsterfullerene. *Science* **1992**, *258*, 1474.

[6] Brabec, C. J.; Sariciftci, N. S.; Hummelen, J. C., Plastic Solar Cells. *Advanced Functional Materials* **2001**, *11*, 15-26.

[7] Coakley, K. M.; McGehee, M. D., Conjugated Polymer Photovoltaic Cells. *Chemistry of Materials* **2004**, *16*, 4533-4542.

[8] Günes, S.; Neugebauer, H.; Sariciftci, N. S., Conjugated Polymer-Based Organic Solar Cells. *Chemical Reviews* **2007**, *107*, 1324-1338.

[9] Tsumura, A.; Koezuka, H.; Ando, T., Macromolecular Electronic Device: Field-Effect Transistor with a Polythiophene Thin Film. *Applied Physics Letters* **1986**, *49*, 1210-1212.

[10] Horowitz, G., Organic Field-Effect Transistors. *Advanced Materials* **1998**, *10*, 365-377.

[11] Bao, Z.; A. Rogers, J.; E. Katz, H., Printable Organic and Polymeric Semiconducting Materials and Devices. *Journal of Materials Chemistry* **1999**, *9*, 1895-1904.

[12] Minemawari, H.; Yamada, T.; Matsui, H.; Tsutsumi, J. y.; Haas, S.; Chiba, R.; Kumai, R.; Hasegawa, T., Inkjet Printing of Single-Crystal Films. *Nature* **2011**, *475*, 364-367.

[13] Deibel, C.; Dyakonov, V., Polymer–Fullerene Bulk Heterojunction Solar Cells. *Reports on Progress in Physics* **2010**, *73*, 096401.

[14] Su, Y.-W.; Lan, S.-C.; Wei, K.-H., Organic Photovoltaics. *Materials Today* **2012**, *15*, 554-562.

[15] Tuček, J.; Błoński, P.; Ugolotti, J.; Swain, A. K.; Enoki, T.; Zbořil, R., Emerging Chemical Strategies for Imprinting Magnetism in Graphene and Related 2d Materials for Spintronic and Biomedical Applications. *Chemical Society Reviews* **2018**, *47*, 3899-3990.

[16] Griffith, M. J.; Cottam, S.; Stamenkovic, J.; Posar, J. A.; Petasecca, M., Printable Organic Semiconductors for Radiation Detection: From Fundamentals to Fabrication and Functionality. *Frontiers in Physics* **2020**, *8:22*.

[17] Lenes, M.; Wetzelaer, G.-J. A. H.; Kooistra, F. B.; Veenstra, S. C.; Hummelen, J. C.; Blom, P. W. M., Fullerene Bisadducts for Enhanced Open-Circuit Voltages and Efficiencies in Polymer Solar Cells. *Advanced Materials* **2008**, *20*, 2116-2119.

[18] Zhao, G.; He, Y.; Li, Y., 6.5% Efficiency of Polymer Solar Cells Based on Poly(3-Hexylthiophene) and Indene-C(60) Bisadduct by Device Optimization. *Adv Mater* **2010**, *22*, 4355-8.

[19] Sariciftci, N. S.; Braun, D.; Zhang, C.; Srdanov, V. I.; Heeger, A. J.; Stucky, G.; Wudl, F., Semiconducting Polymer-Buckminsterfullerene Heterojunctions: Diodes, Photodiodes, and Photovoltaic Cells. *Applied Physics Letters* **1993**, *62*, 585-587.

[20] Liu, J.; Shi, Y.; Yang, Y., Solvation-Induced Morphology Effects on the Performance of Polymer-Based Photovoltaic Devices. *Advanced Functional Materials* **2001**, *11*, 420-424.

[21] Chen, T. A.; Rieke, R. D., The First Regioregular Head-to-Tail Poly(3-Hexylthiophene-2,5-Diyl) and a Regiorandom Isopolymer: Nickel Versus Palladium Catalysis of 2(5)-Bromo-5(2)-(Bromozincio)-3-Hexylthiophene Polymerization. *Journal of the American Chemical Society* **1992**, *114*, 10087-10088.

[22] McCullough, R. D., The Chemistry of Conducting Polythiophenes. *Advanced Materials* **1998**, *10*, 93-116.

[23] Williams, R., Becquerel Photovoltaic Effect in Binary Compounds. *The Journal of Chemical Physics* **1960**, *32*, 1505-1514.

[24] Yoshikawa, K., et al., Exceeding Conversion Efficiency of 26% by Heterojunction Interdigitated Back Contact Solar Cell with Thin Film Si Technology. *Solar Energy Materials and Solar Cells* **2017**, *173*, 37-42.

[25] Liu, Q., et al., 18% Efficiency Organic Solar Cells. *Science Bulletin* **2020**, *65*, 272-275.

[26] Chamberlain, G. A., Organic Solar Cells: A Review. *Solar Cells* **1983**, *8*, 47-83.

[27] Tang, C. W., Two-Layer Organic Photovoltaic Cell. *Applied Physics Letters* **1986**, *48*, 183-185.

[28] Halls, J. J. M.; Walsh, C. A.; Greenham, N. C.; Marseglia, E. A.; Friend, R. H.; Moratti, S. C.; Holmes, A. B., Efficient Photodiodes from Interpenetrating Polymer Networks. *Nature* **1995**, *376*, 498-500.

[29] Wadsworth, A.; Moser, M.; Marks, A.; Little, M. S.; Gasparini, N.; Brabec, C. J.; Baran, D.; McCulloch, I., Critical Review of the Molecular Design Progress in Non-Fullerene Electron Acceptors Towards Commercially Viable Organic Solar Cells. *Chemical Society Reviews* **2019**, *48*, 1596-1625.

[30] Mazzio, K. A.; Luscombe, C. K., The Future of Organic Photovoltaics. *Chemical Society Reviews* **2015**, *44*, 78-90.

[31] Clarke, T. M.; Durrant, J. R., Charge Photogeneration in Organic Solar Cells. *Chemical Reviews* **2010**, *110*, 6736-6767.

[32] Li, Y.; Sonar, P.; Murphy, L.; Hong, W., High Mobility Diketopyrrolopyrrole (Dpp)-Based Organic Semiconductor Materials for Organic Thin Film Transistors and Photovoltaics. *Energy & Environmental Science* **2013**, *6*, 1684-1710.

[33] Wang, K.; Yi, C.; Liu, C.; Hu, X.; Chuang, S.; Gong, X., Effects of Magnetic Nanoparticles and External Magnetostatic Field on the Bulk Heterojunction Polymer Solar Cells. *Scientific Reports* **2015**, *5*, 9265.

[34] Guo, J.; Ohkita, H.; Benten, H.; Ito, S., Charge Generation and Recombination Dynamics in Poly(3-Hexylthiophene)/Fullerene Blend Films with Different Regioregularities and Morphologies. *Journal of the American Chemical Society* **2010**, *132*, 6154-6164.

[35] Howard, I. A.; Mauer, R.; Meister, M.; Laquai, F., Effect of Morphology on Ultrafast Free Carrier Generation in Polythiophene:Fullerene Organic Solar Cells. *Journal of the American Chemical Society* **2010**, *132*, 14866-14876.

[36] Hedley, G. J.; Ruseckas, A.; Samuel, I. D. W., Light Harvesting for Organic Photovoltaics. *Chemical reviews* **2017**, *117*, 796-837.

[37] Mikhnenko, O. V.; Blom, P. W. M.; Nguyen, T.-Q., Exciton Diffusion in Organic Semiconductors. *Energy & Environmental Science* **2015**, *8*, 1867-1888.

[38] Berera, R.; van Grondelle, R.; Kennis, J. T. M., Ultrafast Transient Absorption Spectroscopy: Principles and Application to Photosynthetic Systems. *Photosynthesis Research* **2009**, *101*, 105-118.

[39] Ruckebusch, C.; Sliwa, M.; Pernot, P.; de Juan, A.; Tauler, R., Comprehensive Data Analysis of Femtosecond Transient Absorption Spectra: A Review. *Journal of Photochemistry and Photobiology C: Photochemistry Reviews* **2012**, *13*, 1-27.

Chapter 2.

Spectroscopic Studies on Intramolecular Charge-Transfer Characteristics in Small-Molecule Organic Solar Cell Donors: A Case Study on ADA and DAD Triad Donors

2.1. Introduction

Solution-processed organic solar cells (OSCs) have been intensively investigated as a competitive technology of green energy with low cost of fabrication, light weight, and great mechanical flexibility. [1-2] In the past few decades, significant efforts have been devoted to the molecular design, device structure optimization and morphology control, achieving a higher power conversion efficiency (PCE) over 17% in polymer solar cells (PSCs). [3-7] However, because of the concern in batch-to-batch reproducibility of polymers, PSCs are yet to be elaborated for mass production. On the other hand, small-molecule OSCs (SMOSCs) have also gained attention because of several benefits of small molecule materials, such as synthetic reproducibility from easy synthesis and purification and a greater tendency to self-assemble for charge transport. [8-11] With the material development of small molecule donors (SMDs), the performance of SMOSCs has also been increased to a high PCE over 14%. [12-19] Irrespective of PSCs or

SMOSCs, photoactive layers in them are based on the bulk-heterojunction (BHJ) comprising separate donor and acceptor materials. Thus, their material design are important, and over the decades, investigations into the efficient design of donor materials have led to a remarkable development of OSCs. [20-23] Particularly, the state-of-the-art donor materials, irrespective of polymers and small molecules, are all composed of alternating electron donating (D) and electron accepting (A) building blocks, which can induce intramolecular charge transfer (ICT) characteristics. Such a D-A structure is considered to be the most efficient strategy based on several advantages such as easy control of the energy levels and absorption spectrum, and the achievement of low bandgap energy by selecting appropriate donor and acceptor units. [24-30]

OSC operation is a complex mechanism, which is affected by various factors. Especially, the BHJ morphology of photoactive layers is a major parameter that determines the OSC performances, and the interpenetrating network with nanoscale phase separation is very important for efficient exciton diffusion, charge transfer (CT) and charge collection in OSCs. [31-33] With the remarkable increase in the performance of OSCs, numerous efforts have been focused on the importance of the mixed morphology and the interfacial CT state between donor and acceptor molecules in the active layer. However, when the blend films synthesized by controlling the processing conditions have a similar morphology, the intrinsic property of the donor material itself may play an important role in the photovoltaic properties. In this regard, there is still a lack of comprehensive research to explore the actual role of the ICT process within the

donor molecules and its effect on the photophysical processes at the donor/acceptor interface. To date, a few articles have dealt with the spectroscopic investigation of ICT characteristics of polymeric donor molecules. For instance, Szarko et al. showed that charge generation occurs through both intra- and inter-molecular CT in the PTB7:$PC_{71}BM$ system. [28] Rolczynski et al. reported that local ICT character in the PTBF donor polymer has a significant effect on the exciton dissociation and charge separation in PTBF:$PC_{71}BM$ BHJ devices. [29] On the other hand, Carsten et al. reported that internal dipole moment along the polymer chain controls the charge transfer and recombination rate in BHJ films. [30] It was demonstrated that the ICT characteristics of D-A type donor polymers lowers the exciton binding energy and facilitates the exciton dissociation, and intermolecular charge transfer/separation at the donor/acceptor interface, and furthermore, retards charge carrier recombination in the blend films. [34-35] In this work, we wanted to understand how the ICT characteristics are controlled by the different D-A architectures in SMDs and also their substantial effect on the CT and recombination at the donor/acceptor interface in BHJs. From this perspective, we provide a case study with the most commonly used triad architectures in SMOSCs, A-D-A and D-A-D structures, to model the photophysical processes in molecules, and furthermore, their structural effect on charge separation and charge recombination in BHJ donor/acceptor interface. During the operation of the OSCs, the PCE depends on three dominant parameters, short-circuit current (J_{SC}), open-circuit voltage (V_{OC}), and fill factor (FF), and much effort has been devoted to enhance these parameters. [36-41]

J_{SC} is the current that travels along the solar cells when the voltage across the device is zero. In the working mechanism of OSCs, J_{SC} is greatly influenced by the light absorption as well as the exciton dissociation/CT process. [30,42] Thus, ICT character plays a crucial role in J_{SC} in the OSCs. Therefore, we investigated the correlation between the ICT character and J_{SC} for different ADA and DAD triads.

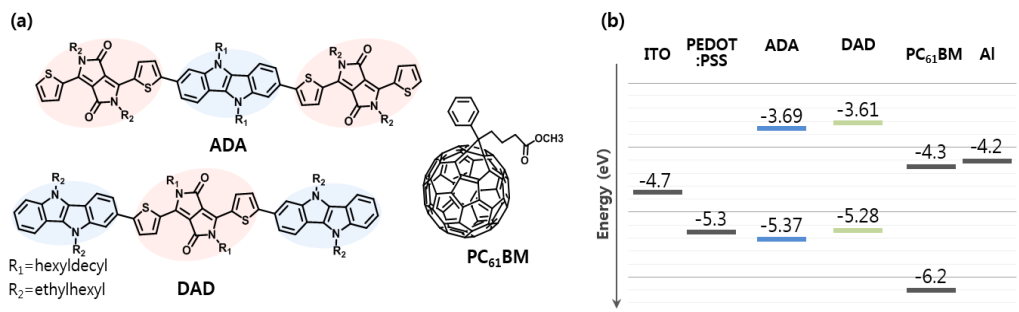

Figure 2-1 (a) Molecular structures and (b) energy levels of ADA, DAD and $PC_{61}BM$.

In the present work, we designed two small molecules of ADA and DAD triad structures to pay our attention to the effect of the triad architecture on the ICT character. For these triad molecules, indolo[3,2-b]indole (IDID) and diketopyrrolopyrrole (DPP) with virtually identical highest occupied molecular orbital (HOMO) energy levels were used as the D and A moieties, respectively (see Figure 2-1). By selecting the D and A pairs of identical HOMO levels, ICT characters of different triads could be properly compared using the identical absorption spectra and delocalized ground-state electron distribution (*vide infra*). Owing to the strong electron donating property of IDID and

electron accepting property of DPP, their derivatives have formerly been investigated as organic semiconducting materials for optoelectronic applications such as organic light-emitting diodes (OLEDs), organic field-effect transistors (OFETs), perovskite solar cells, and OSCs. [43-46] Furthermore, donor materials composed of IDID and DPP were indeed reported for SMOSCs with PCE of 2.45% and PSCs with PCE of 3.0%. [47-48]

Comparing the electronic distribution and excited state ICT characteristics of ADA and DAD triad molecules, and their effect on the photovoltaic properties, we could deduce which architecture is favorable for maximizing ICT character in donor material and suitable for achieving high performance SMOSCs using the IDID-DPP system with a similar blend morphology of photoactive layers. From steady-state optical properties and density functional theory (DFT) calculations, it was found that ADA has a higher molar extinction coefficient and higher oscillator strength than DAD because of large HOMO-lowest unoccupied molecular orbital (LUMO) overlap with the delocalized HOMO and LUMO. Furthermore, based on Lippert-Mataga analysis and time-resolved spectroscopic data, we came to a conclusion that ADA exhibits stronger ICT character in the excited state than DAD, beneficial to high photocurrent generation in OSCs. Strong ICT character of ADA is attributed to larger interactions with the surrounding polar environment in the excited state because of the more delocalized LUMO orbitals and the higher electronegativity and abundance of electrons on end-capping DPP moieties. Transient absorption measurements for blend films were conducted to prove that charge separation and collection are more efficient in ADA:$PC_{61}BM$ than in

DAD:$PC_{61}BM$, achieving higher J_{SC} and PCE values of ADA:$PC_{61}BM$ device cells.

2.2. Experimental Section

2.2.1. Spectroscopic characterization

UV–vis absorption spectra were measured with a UV-1650 PC (Shimadzu) spectrometer. Photoluminescence emission spectra were measured using a Felix32 QM-40 (Photo Technology International) and a Cary Eclipse (Varian) fluorescence spectrophotometer; the emission spectra were corrected for the sensitivity of the photomultiplier.

The femtosecond time-resolved transient absorption (fs-TA) spectrometer consisted of Optical Parametric Amplifiers (Palitra, Quantronix) pumped by a Ti:sapphire regenerative amplifier system (Integra-C, Quantronix) operating at 1 kHz repetition rate and an optical detection system. The generated OPA pulses, which were used as pump pulses, had a pulse width of ~ 100 fs and an average power of 100 mW in the range 550-690 nm. White light continuum (WLC) probe pulses were generated using a sapphire window by focusing on a small portion of the fundamental 800 nm pulses, and were picked off using a quartz plate before entering to the OPA. The time delay between pump and probe beams was carefully controlled by making the pump beam travel along a

variable optical delay (ILS250, Newport). Intensities of the spectrally dispersed WLC probe pulses are monitored using a high Speed spectrometer (Ultrafast Systems). To obtain the time-resolved transient absorption difference signal at a specific time, the pump pulses were chopped at 500 Hz and absorption spectra intensities were saved alternately with or without pump pulses. Typically, 6000 pulses were used to excite samples to obtain the fs-TA spectra at a particular delay time. The polarization angle between the pump and probe beam was set at a magic angle (54.7°) using a Glan-laser polarizer with a half-wave retarder in order to prevent polarization-dependent signals. The cross-correlation fwhm in pump-probe experiments was less than 200 fs and chirp of the WLC probe pulses was measured to be 800 fs in the 450-850 nm region.

2.2.2. Electrochemistry

The HOMO level was calculated from the cyclic voltammetry measurements obtained using a 273A (Princeton Applied Research) with a one-component electrolysis cell consisting of a platinum working electrode, a platinum wire counter-electrode, and a quasi Ag^{+}/Ag electrode as a reference electrode. Measurements were performed in a 0.5mM acetonitrile solution with tetrabutylammonium tetrafluoroborate as the supporting electrolyte at a scan rate of 100 mV/s. Each oxidation potential was calibrated

using ferrocene as a reference. The LUMO level was calculated from the edge of the absorption spectra and the HOMO level from cyclovoltammetry measurement.

2.2.3. Quantum chemical calculation

Theoretical molecular orbital calculation was carried out with (TD)DFT using the Gaussian09 program package at the B3LYP/6-31G(d,p) level to characterize optimized ground and excited-state geometry and electron density of HOMO and LUMO states. In optimized ground-state geometry, the alkyl groups of the molecules were simplified to methyl groups to reduce the cost of calculations. The electronic excitations at the optimized ground-state geometries were calculated using TDDFT at the B3LYP/6-31G(d,p) level to explore the electronic distribution of the excited state.

2.2.4. Device fabrication

The OSCs in this study were fabricated by the following method. Patterned ITO glass substrates were cleaned in an ultrasonic bath with trichloroethylene, acetone, isopropyl alcohol, for 10 min, respectively, and then exposed to UV/O_3 treatment for 20 min. PEDOT : PSS (Clevios P VP.AI 4083, Heraeus) was then spin-coated on to the substrate at 5000 rpm for 30 s to a thickness of 40 nm and then the film was dried at 150 °C for

20 min. Subsequently, the active layer films were spin-coated (1500 rpm for 40 s for ADA and 2000 rpm for 40 s for DAD) using the ADA (or DAD):$PC_{61}BM$ blended solution stirred over 12 h at 30 °C to obtain a thickness of around 80 nm in a N_2-filled glovebox. Al electrodes were deposited via thermal evaporation in a vacuum chamber with a thickness of 100 nm, followed by post-annealing at 110 °C for 3min for ADA and at 90 °C for 5 min for DAD.

The current density–voltage (*J–V*) characteristics of the solar cells were measured with a Keithley 4200 source measurement unit. The solar cell performances were characterized under AM 1.5G condition with an illumination intensity of 100 mW/cm^2 generated using an Oriel Sol 3A solar simulator. *J-V* characteristics of the cells with illumination were measured with 0.09 cm^2 of effective active area defined by aperture.

Incident photon to current conversion efficiency (IPCE) was measured using an Oriel QE/IPCE measurement Kit composed of a 300 W Xenon lamp, a monochromator, an order sorting filter wheel, the Merlin lock-in amplifier, and a chopper.

2.3. Result and Discussion

Herein, to pay our attention to the effect of the triad architecture on the electronic distribution and the ICT character, we have chosen IDID and DPP as the electron donating and accepting moieties, respectively, because they have almost identical

HOMO energy levels. The rationale of such a peculiar design is to make the HOMO of the ADA and DAD triads delocalized over the whole structure. The molecules were synthesized through the synthetic procedure according to the previously reported procedures. [43,45,49] Because of the six branched alkyl side chains (hexyldecyl chains on core units and ethylhexyl chains on terminal units), both target materials were highly soluble in common organic solvents such as chloroform and chlorobenzene, which are widely used solvents in the fabrication of OSCs.

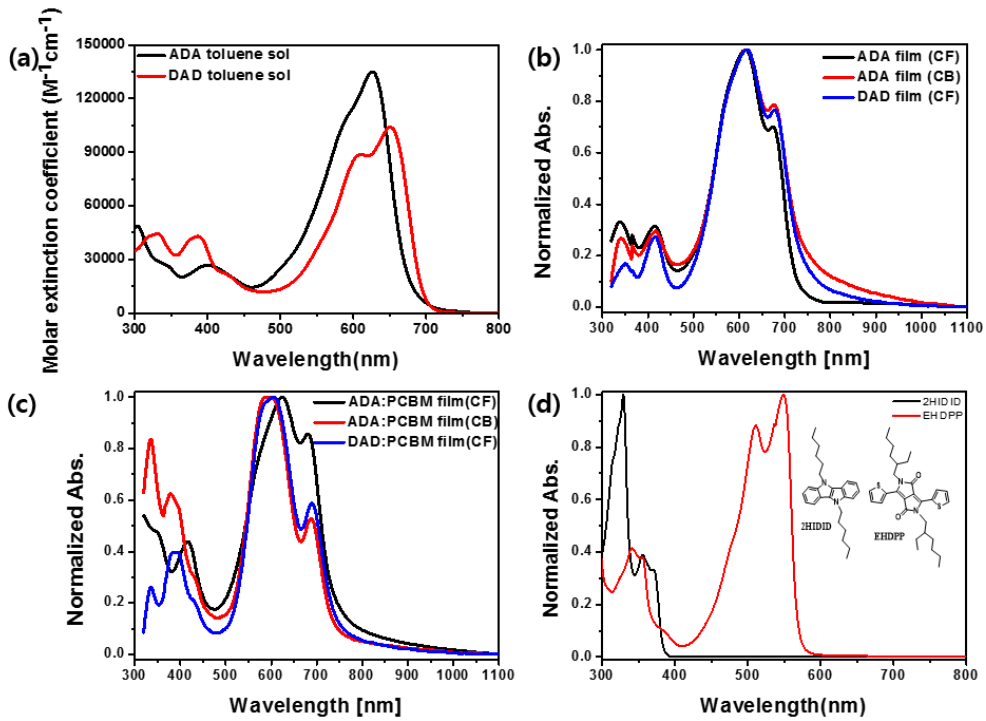

Figure 2-2 Molar extinction coefficients of ADA (black) and DAD (red) in toluene solution, and normalized UV/vis absorption spectra of (b) donor (ADA, DAD) neat films and (c) donor (ADA, DAD):acceptor ($PC_{61}BM$) blend films using chloroform and chlorobenzene solvents with the same spin coating condition with the optimized device cells and (d) Normalized absorption spectra of 2HIDID (donor moiety) and EHDPP (acceptor moiety) in toluene solution.

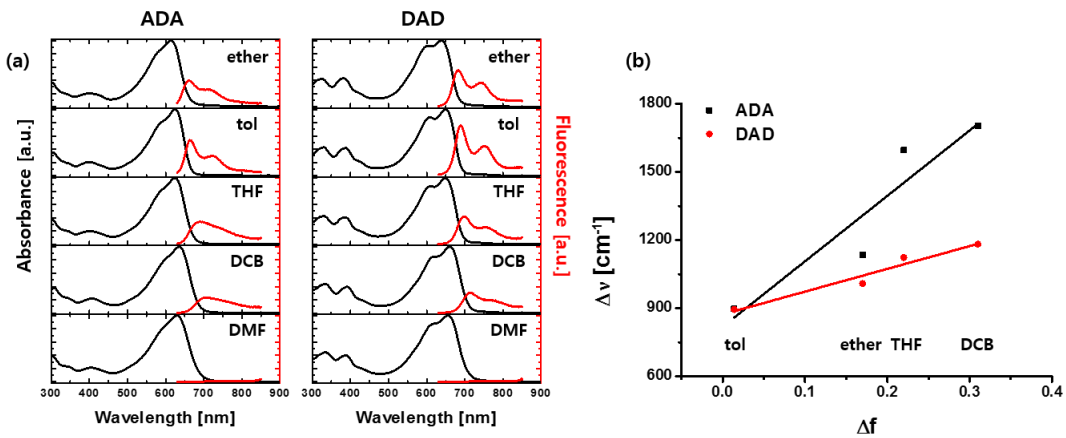

Figure 2-3 (a) Steady-state absorption and fluorescence spectra of ADA (left) and DAD (right) in various solvents (ether, toluene, tetrahydrofuran, dichlorobenzene, dimethylformamide) and (b) Lippert-Mataga plot of ADA (black) and DAD (red) solutions using four solvents (ether, toluene, tetrahydrofuran, dichlorobenzene).

Table 2-1 Photoluminescence quantum yield (PLQY) of various solutions of ADA and DAD.

	Toluene (tol)	Diethyl ether (ether)	Tetrahydrofuran (THF)	1,2-Dichlorobenzene (DCB)	N,N-Dimethylformamide (DMF)
ADA	15.6%	12.9%	10.6%	7.0%	-
DAD	13.4%	11.8%	8.8%	7.3%	-

Figure 2-2 shows (a) the molar extinction coefficients of ADA and DAD in toluene and the normalized UV-vis absorption spectra of the (b) donor (ADA, DAD) neat films and (c) donor (ADA, DAD):acceptor ($PC_{61}BM$) blend films. Compared to the absorption spectra of alkylated donor (2HIDID) and acceptor (EHDPP) moieties in toluene, ADA and DAD show strong absorption in the 550-700 nm region, which is absent in the absorption spectra of both 2HIDID and EHDPP solutions. This strong absorption originates from the vertical $S_0 \rightarrow S_1$ transition with ICT character. ADA shows extremely high molar extinction coefficients with a maximum value of 134,900 M^{-1} cm^{-1} at 626 nm, while DAD exhibits relatively weaker light absorption strength than ADA with a maximum value of 104,000 M^{-1} cm^{-1} at 650 nm because of the relatively smaller oscillator strength. Both the absorption spectra of ADA and DAD films show broad and red-shifted absorption spectra compared to solution state ones because of inhomogeneous broadening with the formation of aggregation originating from π-π stacking and strong intermolecular interactions between neighboring molecules in the solid state.

To further investigate the ICT characteristics in the solution state, the photoluminescence properties were examined in several solvents with different polarities [toluene, 1,2-dichlorobenzene (DCB), diethyl ether, tetrahydrofuran (THF), and dimethylformamide (DMF) solutions] as shown in Figure 2-3(a). In nonpolar solvents (toluene and diethyl ether), the fluorescence spectra of both molecules are shown in 650-850 nm region with two emission bands. However, in polar solvents (THF and DMF)

and a halogenated solvent (DCB), strong solvatochromism appears with a bathochromic shift and fluorescence quenching indicating strong ICT properties. ADA shows a larger extent of bathochromic shift and fluorescence quenching in the photoluminescence spectra because of stronger stabilization of the excited state in polar solvents attributed to its stronger dipolar ICT character than DAD. [50-52] The photoluminescence quantum yields (PLQYs) of various solutions with different solvent polarities were measured using an integrating sphere (Table 2-1). The decrease in the PLQY is due to the stabilization of the transferred charge within the molecules in the polar medium. [53-55] Because ADA strongly interacts with the polar solvent, its PLQY is much decreased compared to DAD, indicative of the strong ICT character of ADA. To explore the excited state ICT character, the Lippert–Mataga analysis was employed. The Lippert–Mataga equation shows the relationship between the Stokes shift and solvent polarity and is an efficient tool to analyze the effect of the solvent polarity on the difference in the dipole moment of chromophores between the ground and excited states, described as follows

$$\Delta\nu = \nu_{abs} - \nu_{em} = \frac{2\Delta f}{hca^3}\left(\Delta\mu_{ge}\right)^2 + const. \quad \text{(eqn.1)}$$

, where $\Delta\nu$ is the Stokes shift, h is the Planck constant, c is the velocity of light, $\Delta\mu_{ge}$ is the difference between the dipole moments of the excited state and the ground state, and a is the radius of the Onsager cavity around the fluorophore. [56-60] Δf is the orientation polarizability, defined with the dielectric constant (ε), and the refraction index (n) of the solvent using the following equation:

$$\Delta f = \frac{(\varepsilon-1)}{(2\varepsilon+1)} - \frac{(n^2-1)}{(2n^2+1)} \text{ (eqn.2)}$$

Figure 2-3(b) shows the Lippert-Mataga plots of $\Delta\nu$ versus Δf for ADA and DAD. By fitting the plots with the Lippert–Mataga equation (eqn. 1), the slope is expressed by the term of $\frac{2(\Delta\mu_{ge})^2}{hca^3}$, and the slope values are 2,881 cm^{-1} and 1,002 cm^{-1} for ADA and DAD, respectively. The slope of ADA is nearly 3 times as large as the slope of DAD, while the Onsager cavity radius of ADA is only slightly longer than that of DAD. (Onsager cavity radius is 7.14 and 6.91 Å for ADA and DAD, respectively.) Consequently, the dipole moment change between the ground and excited states, $\Delta\mu_{ge}$, is 10.2 D for ADA, which is much larger than that of DAD, 5.73 D. Because the dipole moments of both compounds in the ground states are almost zero due to their centrosymmetric structure, the absorption spectra in various solutions with different solvent polarities do not show a large red-shift compared to the fluorescence spectra of the solutions. Thus, the dipole moment change obtained from the Lippert-Mataga equation originates from the excited state dipole moment, most probably indicating photoinduced charge localization on one branch of the compounds with the symmetry-broken charge distribution and polar nature of the excited states. [53,61-67] Hence, strong solvatochromism and a large dipole moment change indicate a stronger excited state ICT character in ADA than DAD. In the photovoltaic system, the polarized excited state and localized charge distribution lead to the strong ICT character in the molecule, reducing the exciton binding energy and facilitating charge separation at the

donor/acceptor interface in blend films. [35,68-74] Therefore, ICT character is the key factor influencing photocurrent in BHJ OSCs.

To evaluate the energy levels of the triad ADA and DAD, the electrochemical properties of compounds were measured by cyclic voltammetry as shown in Figure 2-4. The HOMO levels of both triad molecules were determined by the oxidation onset of cyclic voltammograms, and optical bandgaps were estimated from the edge of the absorption spectra. Thus, the LUMO levels were estimated by subtracting the optical bandgaps from the HOMO levels (Table 2-2). The HOMO and LUMO levels are -5.37 eV and -3.69 eV for ADA, and -5.28 eV and -3.61 eV for DAD, respectively. Because of the difference in the molecular structure, DAD possesses more IDID donor moieties than ADA, which results in easier oxidation and by extension higher-lying HOMO level in DAD. The cyclic voltammetry results are consistent with DFT calculations that DAD exhibits larger electron donating property with higher-lying HOMO and LUMO levels than ADA. The HOMO levels of both compounds are suitable for efficient charge separation in BHJ OSCs obtained using $PC_{61}BM$ as an electron acceptor. However, ADA exhibits a deeper HOMO level than DAD because of its molecular architecture, which is beneficial to obtain higher V_{OC} in the OSCs.

Table 2-2 Optical, electrochemical, and thermal properties of ADA and DAD.

	$\lambda_{abs,sol}$ [a] (nm)	$\lambda_{abs,film}$ [b] (nm)	$\lambda_{onsets,film}$ [b] (nm)	B_g [c] (eV)	E_{HOMO} [d] (eV)	E_{LUMO} [e] (eV)	T_m [f] (℃)	T_d [g] (℃)
ADA	304,398,626	311,418, 620,670	734	1.68	-5.40	-3.72	222.8	389.4
DAD	371,386,402, 441,606,650	331,387, 608,690	742	1.67	-5.28	-3.61	174.7	400.9

a) Measured in toluene solution of concentration of $1x10^{-5}$ M.

b) Spin-coated 0.5wt% using 1,2-dichloroethane solution.(1000 rpm/30s)

c) Optical band gap was obtained from absorption edge

d) Calculated by equation : $E_{HOMO}=[-(E_{onset}-E_{ferrocene})-4.8]$

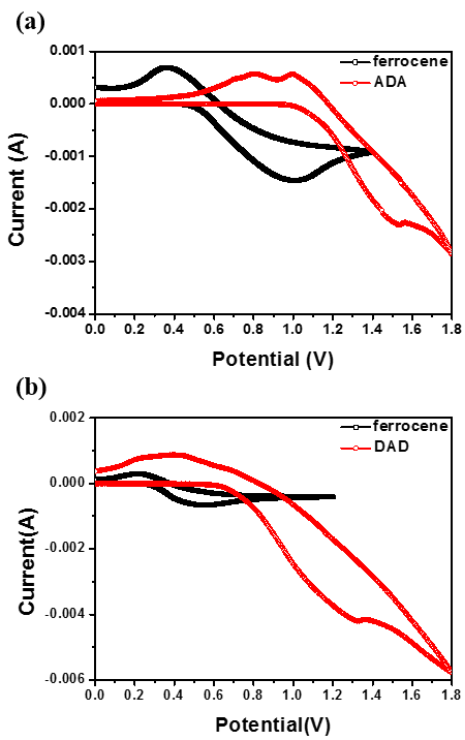

Figure 2-4 The cyclic voltammograms of (a) ADA (red) in film and ferrocene (black) and (b) DAD (red) in film and ferrocene (black) with TBATFB in acetonitrile as the supporting electrolyte.

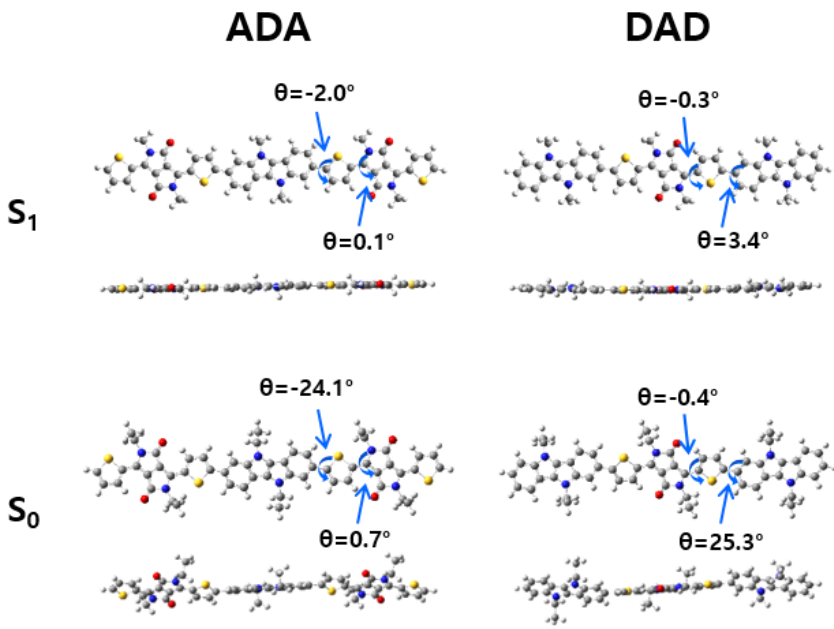

Figure 2-5 The calculated optimized ground and excited state geometry of ADA and DAD (alkyl side groups are substituted with methyl groups) using Gaussian 09 at the B3LYP/6-31G(d,p) levels. (upper: top view, lower: side view).

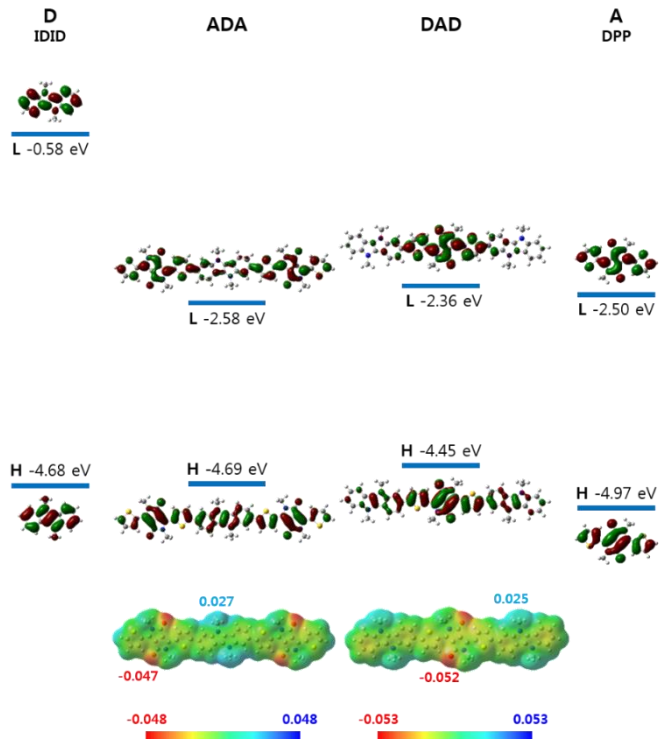

Figure 2-6 (Top) Frontier molecular orbitals and calculated energy levels of ADA and DAD with IDID (D) and DPP (A) units and (bottom) molecular electrostatic potential (ESP) surface of ADA and DAD at the level of B3LYP/6-31G(d,p). (isodensity surface is defined as ρ=0.0004).

Table 2-3 Computed parameters (dominant transition character, oscillator strength, and transition dipole moments) of main $S_0 \rightarrow S_1$ transition of ADA and DAD from TDDTF calculation.

	Bg	State	Transition and composition	f	μ_{tr}(Debye)
ADA	2.10 eV	$S_0 \rightarrow S_1$	H → L (99%)	2.1522	2.6606
DAD	2.09 eV	$S_0 \rightarrow S_1$	H → L (99%)	2.0481	2.5822

Theoretical molecular orbital calculations were carried out using DFT method and Gaussian09 at the B3LYP/6-31G(d,p) level to characterize the optimized geometry and electron density of the HOMO and LUMO states. ADA and DAD (methyl groups are substituted for hexyldecyl and ethylhexyl groups for simplicity) exhibit twisted backbone structures with the dihedral angles of 24-26° between IDID and DPP moieties in the optimized geometry in the ground state, while they exhibit almost planar structure with smaller dihedral angles of 0-5° in the excited state. (Figure 2-5).

As shown in Figure 2-6, the HOMO orbitals are evenly delocalized throughout the entire IDID-DPP backbones in both triad molecules as we intentionally designed by adopting D and A structures of similar HOMO energy. However, the LUMO orbitals of ADA and DAD are slightly different, as the LUMO of ADA is spatially more delocalized than that of DAD. This is attributed to the ICT characteristics in the optical transition. In the LUMO of ADA, electron clouds are evenly spread over the end-capping DPP moieties, and also some electron clouds exist on the core IDID, while the LUMO of DAD is much more localized on the core DPP moiety. The delocalization of the LUMO stabilizes more the energy level of ADA. In order to explain orbital overlap in ADA and DAD, electron donating and electron accepting strengths of IDID and DPP moieties are important. The electron donating strength of DPP is comparable to that of IDID and the HOMOs of both IDID and DPP contribute to those of triad molecules, resulting in the delocalized HOMO levels in ADA and DAD. On the other hand, the electron accepting strength is much stronger in DPP than in IDID, resulting in a smaller contribution of

IDID to the LUMOs of ADA and DAD. As predicted from the TDDFT results, the main absorption with $S_0 \rightarrow S_1$ transition is composed of HOMO→LUMO transitions in both ADA and DAD, and the orbital overlap between the HOMO and LUMO is larger in ADA than in DAD. The orbital overlap is related to the transition dipole moment between two states and, by extension, the oscillator strength. Large orbital overlap of ADA with the delocalized HOMO and LUMO brings about larger oscillator strength and consequently stronger light absorbing ability of ADA. (Table 2-3) High light absorbing property with large oscillator strength is a crucial factor in the photovoltaic properties of OSCs. Therefore, because of its stronger light absorbing property, ADA has an advantage in obtaining high J_{SC} in OSCs.

To determine the charge distribution in the molecules, we computed the excited-state molecular electrostatic potential (ESP) maps through the quantum chemical calculations. As shown in Figure 2-6, red represents the region with lowest electrostatic energy with an abundance of electrons and blue represents the region with highest electrostatic energy with a relative absence of electrons. From the ESP results, electron-rich regions are nearby the oxygen atoms in DPP units, and relatively electron-deficient regions are nearby nitrogen atoms on IDID units, which is well correlated with the delocalized HOMO throughout the backbones and the LUMO on DPP units. Nitrogen atoms on IDID are alkylated and do not possess much high ESP because of the delocalized hole density and thus they are not easy to interact with solvent molecules. On the other hand, oxygen atoms on DPP are exposed to the environment and possess lowest ESP with localized

electron density and can thus easily interact with positive charges in the surrounding environment. Excited state symmetry-breaking charge distribution to give the static dipole moment in centrosymmetric molecules can originate from the fluctuation and instantaneous orientation of solvent molecules, which produce the asymmetric interactions including dipolar, quadrupolar, H-bonding and halogen-bonding between each arm of the solute and solvent molecules. Therefore, asymmetric ICT character could be induced even in the symmetric triad molecules (quadrupolar or octupolar systems) because of different solvent interactions with each branch of triad molecules. In the viewpoint of the potential energy surface, fast interconversion between two minimum energy states retains symmetry of the charge distribution in nonpolar solvents. However, in a polar medium, polar solvation induces slower interconversion and the polar ICT character of the symmetry broken state is frozen. [53,61-67] Consequently, large negative ESP of end-capping DPP units with a delocalized LUMO in ADA results in a favorable interaction between ADA and positive charges of solvent molecules and thus in a higher extent of electron cloud shift, which is likely relevant to the dipolar ICT state in ADA amplifying the extent of asymmetry in charge distribution. As a result, centrosymmetric triad molecules could exhibit a dipolar ICT state in the polar environment, and ADA exhibits stronger ICT character than DAD.

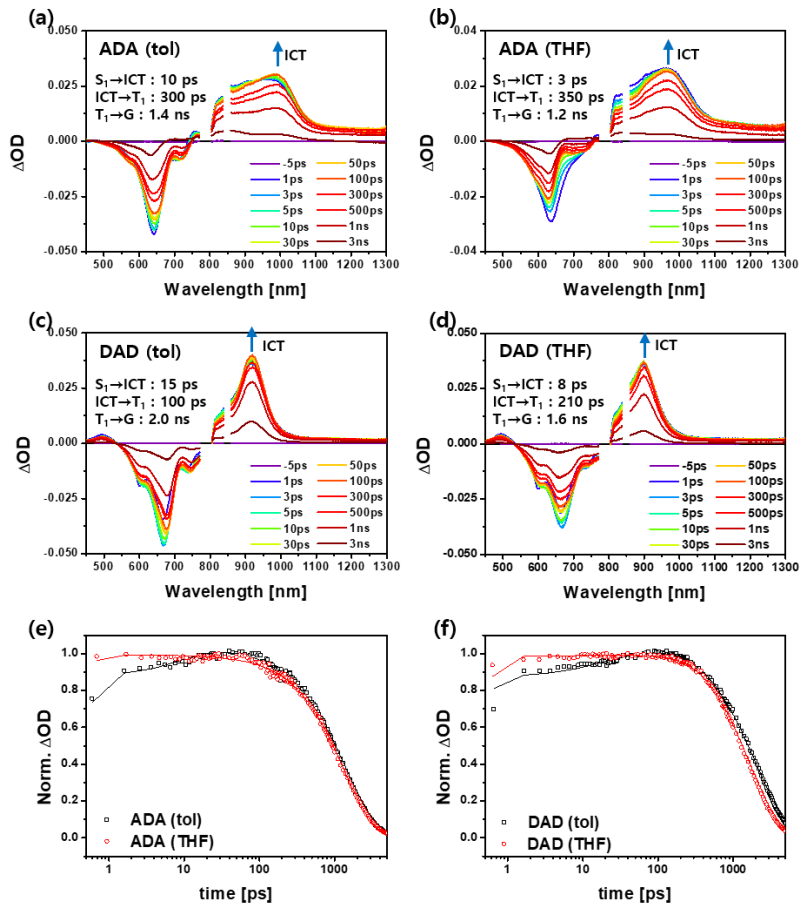

Figure 2-7 Femtosecond transient absorption spectra of ADA in (a) toluene and (b) THF solutions, and DAD in (c) toluene, and (d) THF solutions and decay profiles of ICT absorption in (e) ADA and (f) DAD solutions (The solid lines in (e), (f) are the best fits for each decay profile).

To compare the ICT properties of ADA and DAD, femtosecond transient absorption measurements were conducted in ADA and DAD solutions. The TA spectra of ADA and DAD solutions in nonpolar toluene and polar THF are shown in Figure 2-7, upon photoexcitation at 600 nm to be in resonance with the $S_0 \rightarrow S_1$ transition. The TA spectra of ADA and DAD solutions are composed of ground state bleaching (GSB) and stimulated emission (SE) overlapping with broad excited state absorption (ESA). TA spectra of ADA and DAD solutions clearly show an increase in ESA signals (maximum at 995 nm for ADA in toluene, 965 nm for ADA in THF, 915 nm for DAD in toluene, and 900 nm in DAD in THF) within several hundreds of picoseconds, suggesting the presence of locally excited S_1 (LE)→relaxed S_1 (ICT) state transition in the excited state. Decay profiles of ADA and DAD solutions were fitted with three lifetimes for global analysis with a simple sequential model (A→B→C) using the Glotaran software and the evolution-associated spectra (EAS) are shown in Figure 2-8. The $\tau 1$ component is the lifetime of the locally excited $S_1 \rightarrow$relaxed S_1 transition, and charge transfer is faster in ADA solutions than in DAD solutions. (τ_{rise}~10 ps for ADA in toluene, 3 ps for ADA in THF, 15 ps for DAD in toluene, and 8 ps for DAD in THF solutions). Especially, ADA in the THF solution exhibits the fastest CT time and a largest extent of decrease in the SE signal around 650-700 nm indicating the largest ICT character with asymmetric charge distribution in the excited state in the polar THF solution. The τ_2 component is the charge recombination time of the ICT state and τ_3 is the lifetime of long-lived species such as the triplet state.

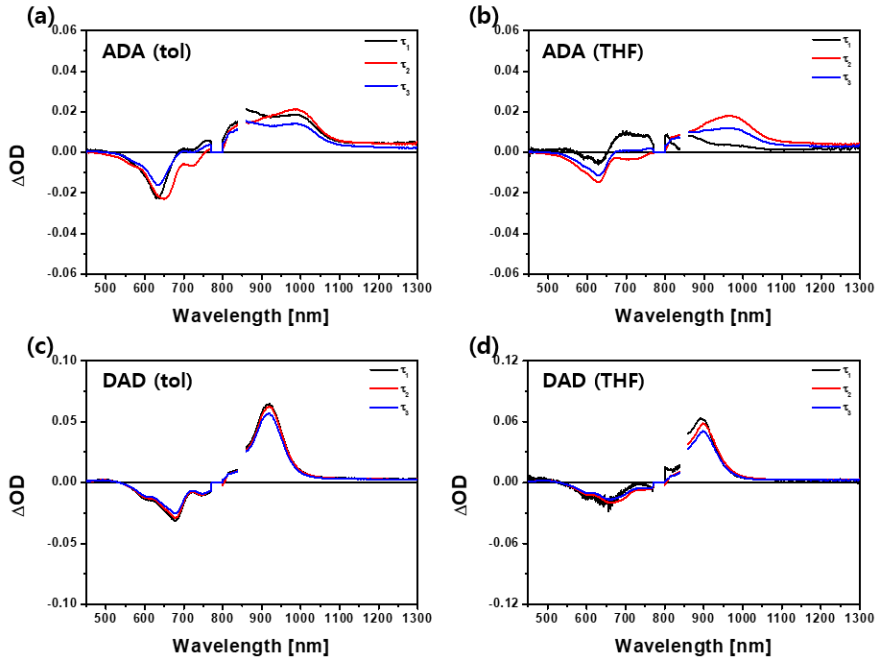

Figure 2-8 Evolution-associated spectra of ADA in (a) toluene, (b) THF, and DAD in (c) toluene, and (d) THF solutions extracted from the global analysis using Glotaran software.

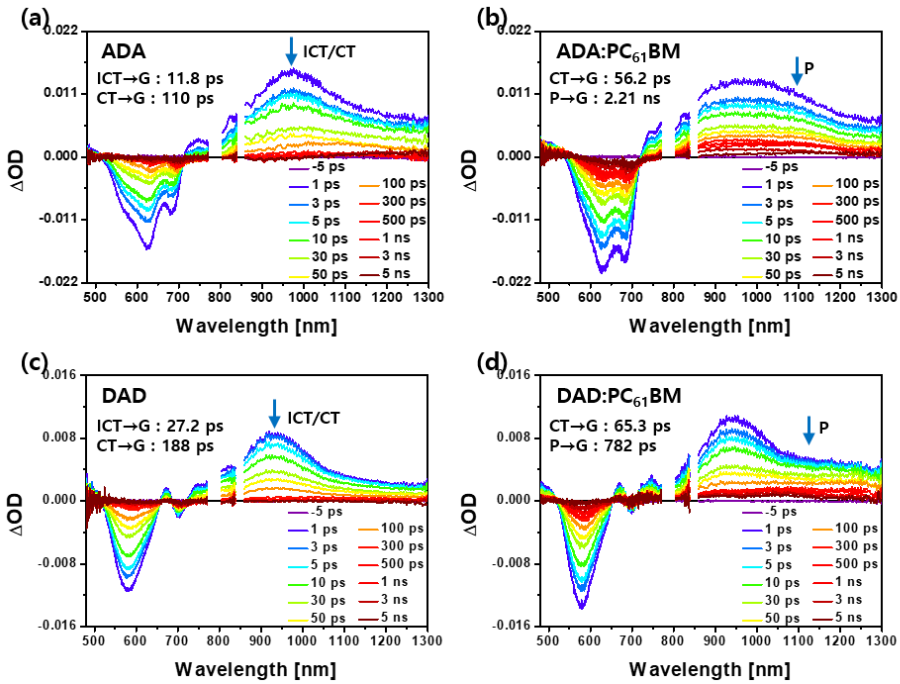

Figure 2-9 Femtosecond transient absorption spectra of (a) ADA neat film, (b) ADA:$PC_{61}BM$ blend film, (c) DAD neat film, and (d) DAD:$PC_{61}BM$ blend film.

Table 2-4 Time components of fs-TA using ADA and DAD neat films and ADA:$PC_{61}BM$ and DAD:$PC_{61}BM$ blend films by fitting the decays to the multiexponential functions[a]. All films were spin-coated using chloroform solutions.

	ADA	DAD	ADA:$PC_{61}BM$	DAD:$PC_{61}BM$
τ_1	11.8 ps (13%)	27.2 ps (21%)	56.2 ps (6.0%)	65.3 ps (22%)
τ_2	110 ps (87%)	188 ps (77%)	2.21 ns (93%)	782 ps (77%)

[a] The percentile values are the amplitudes of each exponential function.

To compare the photoinduced charge separation and recombination dynamics in the solid state, the transient absorption spectra of donor (ADA, DAD) neat films and donor (ADA, DAD):acceptor ($PC_{61}BM$) blend films were measured, which were fabricated under the same spin coating conditions as those used for the preparation of optimized device cells using chloroform solutions. Figure 2-9 shows the TA spectra of the neat films of donor (ADA and DAD) materials, and the blend films of donor (ADA and DAD) and $PC_{61}BM$ acceptor upon photoexcitation at 670 nm. The pump beam excites the donor molecules (ADA and DAD) and CT excitons are formed within 200 fs. The charge transfer process in the solid state is much faster than that in the solution state because of the direct intermolecular interactions between neighboring molecules. The TA spectra of the ADA neat films show GSB absorption in 450-700 nm, and broad ESA absorption around 700-1300 nm with the CT state absorption peak at 1000 nm. The DAD neat film exhibits TA features with GSB in 450-700 nm, and broad ESA around 700-1300 nm with the CT state absorption peak at 920 nm. For both donor neat films, fluorescence is almost quenched indicating efficient and strong CT between neighboring molecules in both ADA and DAD in the solid state which in turn results in the absence of the SE signal in the TA spectra and multi recombination components due to the amorphous film morphology.

In the blend films obtained using ADA and DAD as a donor and $PC_{61}BM$ as an acceptor molecule, the ESA spectra of the donor polaron are shown with the maximum peak at 1100 nm for ADA and 1150 nm for DAD. The presence of the donor polaron

absorption in blend films within 200 fs indicates ultrafast charge separation at the interfacial area between the donor (ADA, DAD) and a the cceptor ($PC_{61}BM$) in the blend films. Time components of the decay profile are shown in Table 2-4. Every film exhibits the exciton-exciton annihilation components, but this term is excluded for the calculation of absorption proportion for the CT state and separated charge carriers. The amount of generated polaron is analyzed by fitting the decay profile with a multiexponential decay model, where the CT state and polarons are formed on an ultrafast time scale, and decay with the CT state lifetime of tens of picoseconds and the polaron state lifetime of several nanoseconds. Finally, the amount of generated polarons is larger in the ADA:$PC_{61}BM$ film than that in the DAD:$PC_{61}BM$ film as shown in Table 2-4, and furthermore, the charge carrier lifetime is much longer in the ADA:$PC_{61}BM$ film than in DAD:$PC_{61}BM$, because of the less tightly bound electrons and holes in the BHJ film. The larger generated polarons and retarded charge carrier recombination due to strong ICT character are beneficial to the photovoltaic properties. Based on these results, we can suggest that ADA exhibits stronger ICT character than DAD after photoexcitation due to the symmetry breaking asymmetric interaction with the neighboring molecules and polar environment. Furthermore, ADA generates more electrons at the end-capping DPP units, beneficial to the CT to the $PC_{61}BM$ acceptor molecules and photocurrent generation, and slower charge carrier recombination, which is beneficial to the charge collection in OSCs. [75-76]

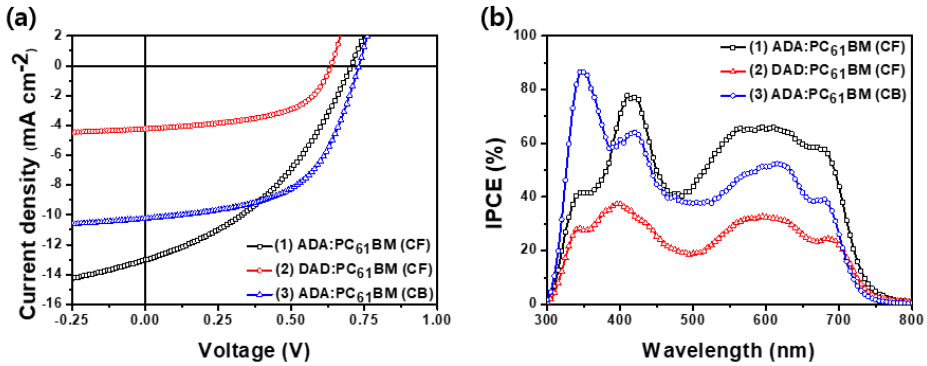

Figure 2-10 (a) Characteristic *J–V* curves and (b) IPCE spectra of solar cells fabricated from ADA:$PC_{61}BM$ in chloroform (black) and chlorobenzene (red) and DAD:$PC_{61}BM$ in chloroform (blue) illuminated under AM 1.5G, 100 mW/cm^2.

Table 2-5 Photovoltaic properties of OPV cells using blend films of ADA (or DAD):$PC_{61}BM$ spin-coated using chloroform/chlorobenzene.

Compound, blend ratio, concentration, solvent	J_{SC} (mA/cm^2)	$J_{SC,\ Cal.}$ (mA/cm^2)	V_{OC} (V)	FF (%)	PCE (%)
ADA:$PC_{61}BM$, 7:3, 20 mg/mL, Chloroform	13.02	12.50	0.71	39.1	3.61
DAD:$PC_{61}BM$, 2:1, 15 mg/mL, Chloroform	6.62	5.97	0.65	57.2	2.46
ADA:$PC_{61}BM$, 2:1, 25 mg/mL, Chlorobenzene	10.24	9.85	0.73	55.6	4.15

To demonstrate the actual effect of the ICT process in ADA and DAD as an electron donor in SMOSCs, photovoltaic devices were fabricated based on the conventional device architecture of ITO/PEDOT:PSS/ADA (or DAD):$PC_{61}BM$ blend/Al. Device optimization was conducted with different donor : acceptor compositions, solution concentrations, and spin rates for both ADA:$PC_{61}BM$ and DAD:$PC_{61}BM$ devices. Optimized photovoltaic properties are shown in Figure 2-10 and Table 2-5 with current density–voltage (*J–V*) characteristics under one sun (AM 1.5G) illumination and device performance parameters. Furthermore, AFM, BF-TEM, and HAADF-STEM measurements were conducted to analyze the morphological effect on OSCs as shown in Figure 2-11. Blend films exhibit a smooth and uniform surface with a root mean square roughness of 0.8-1.0 nm in the AFM results. In addition, STEM images also show the morphology of the blend films. The DAD:$PC_{61}BM$ blend film exhibits slightly larger domains than the ADA:$PC_{61}BM$ blend film. However, even in the larger domains in the DAD:$PC_{61}BM$ film, both blend films have interconnected network and nanoscale phase separation, favorable for exciton dissociation and charge transport, resulting in efficient and ultrafast charge separation at the interfacial area as confirmed in fs-TA measurements. In addition, two-dimensional grazing incidence wide angle X-ray scattering (2D-GIWAXS) measurements were conducted to compare the morphology of the ADA:$PC_{61}BM$ and DAD:$PC_{61}BM$ blend films. The 2D-GIWAXS images of the ADA:$PC_{61}BM$ and DAD:$PC_{61}BM$ films exhibited similar morphology with both lamellar (h00) and π-π stacking (010) peaks in the out-of-plane (q_z) and in-plane (q_{xy})

directions. (Figure 2-12) These results indicate that the edge-on and face-on crystal structures co-exist in both the ADA:$PC_{61}BM$ and DAD:$PC_{61}BM$ blend films. In addition, the DAD:$PC_{61}BM$ blend film exhibits a slightly sharper and stronger π-π stacking peak at $q_{xy,z}$ = 1.38 $Å^{-1}$ than the ADA:$PC_{61}BM$ blend filmsz because of a stronger π-π stacking effect with an ordered structure of DAD, which has the potential to favor intermolecular charge transport and enhance photocurrent. However, despite slightly stronger π-π stacking in DAD:$PC_{61}BM$, both blend films exhibit a broad distribution of the π-π and lamellar peaks along the isotropic ring in the diffraction patterns, indicating no preferential orientation. These results imply that the effect of ICT character of ADA on the enhanced J_{SC} of the ADA:$PC_{61}BM$ OSC is much more important than the morphological effect.

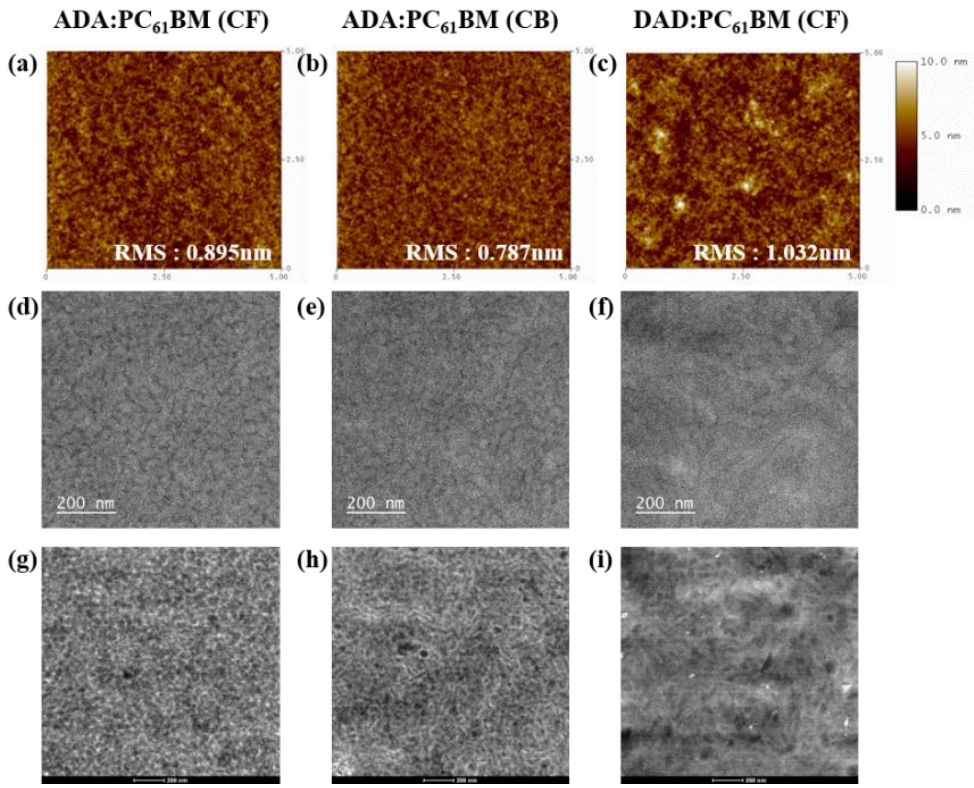

Figure 2-11 (a,b,c) Tapping mode AFM topography, (d,e,f) BF-TEM images and (g,h,i) HAADF-STEM images of the blend films fabricated using ADA:PC_{61}BM chloroform solution (7:3 w/w, 20 mg/mL, 1500 rpm), ADA:PC_{61}BM and chlorobenzene solution (2:1 w/w, 25 mg/mL, 1500 rpm) and DAD:PC_{61}BM devices fabricated using chloroform solution (2:1 w/w, 15 mg/mL, 2000 rpm).

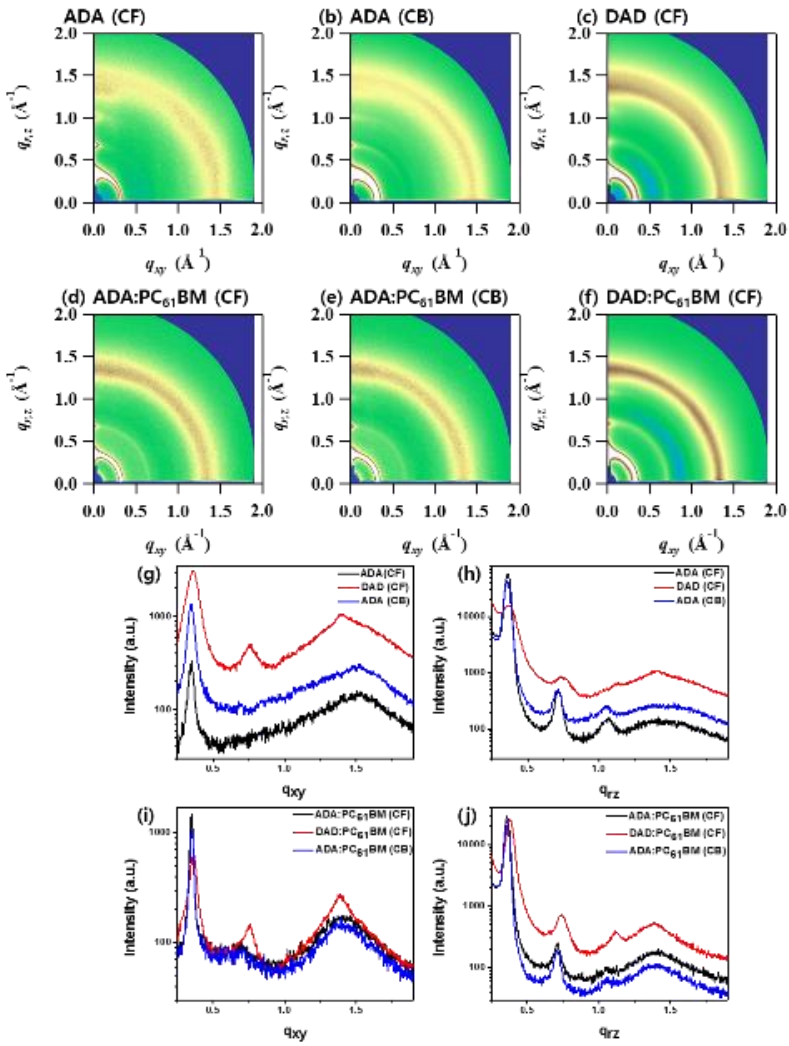

Figure 2-12 Two-dimensional grazing incidence wide angle X-ray scattering (2D-GIWAXS) images of (a) ADA and (d) ADA:$PC_{61}BM$ film spin-coated using chloroform solutions, (b) ADA and (e) ADA:$PC_{61}BM$ film spin-coated using chlorobenzene solutions and (c) DAD and (f) DAD:$PC_{61}BM$ film spin-coated using chloroform solutions. The line-cut intensities for the in-plane direction for (g) ADA and DAD neat films and (i) ADA:$PC_{61}BM$ and DAD:$PC_{61}BM$ blend films and the out-of-plane directions for (h) ADA and DAD neat films and (j) ADA:$PC_{61}BM$ and DAD:$PC_{61}BM$ blend films. (ADA neat films and ADA:$PC_{61}BM$ blend films are spin-coated using chloroform and chlorobenzene solutions.)

Compared to the ADA:$PC_{61}BM$ device, the DAD:$PC_{61}BM$ device exhibits poor performances. Because of a small amount of generated polarons due to weak ICT character and low molar extinction coefficient of DAD, J_{SC} of the DAD:$PC_{61}BM$ device is 6.62 mA/cm^2, which is considerably low compared to that of the ADA:$PC_{61}BM$ device. Furthermore, because of the higher-lying HOMO level of DAD, V_{OC} is also smaller in the DAD:$PC_{61}BM$ device than in ADA:$PC_{61}BM$ one. As a result, the photovoltaic performances of OSCs using DAD:$PC_{61}BM$ is lower than those of ADA:$PC_{61}BM$, indicating that ADA is a superior donor design compared to DAD.

After confirming the superiority of the architecture of ADA as a donor molecule in SMOSCs, device optimization was conducted using ADA:$PC_{61}BM$ combination with different spin-coating solvents. In the device spin-coated using chloroform solution, the device exhibits an extremely high J_{SC} up to 13.02 mA/cm^2 with a FF of 39.1% and a PCE of 3.61%. On the other hand, the device using chlorobenzene as a spin-coating solvent exhibits a high FF up to 55.6% with a J_{SC} of 10.24 mA/cm^2 and a PCE of 4.15%. By changing the spin-coating solvent from chloroform to chlorobenzene, there were slight difference in the device performances. In spite of lowered J_{SC}, the FF was much increased, which results in a higher PCE of 4.15%. From the AFM and TEM results, the ADA:$PC_{61}BM$ device using chlorobenzene exhibited a more interpenetrating network than the device using chloroform, which is an important element to achieve a high FF. In addition, from the fs-TA analysis, photoinduced charge separation was efficient with ultrafast CT at the donor/acceptor interface in both ADA:$PC_{61}BM$ blends, but the

proportion of polaron absorption of the ADA:$PC_{61}BM$ blend using the chlorobenzene solution was slightly lowered compared to that of the ADA:$PC_{61}BM$ blend using chloroform, which is still higher than that of the DAD:$PC_{61}BM$ blend. (Figure 2-13 and Table 2-6) Consequently, the ADA:$PC_{61}BM$ device obtained using chlorobenzene exhibits the highest PCE, confirming that ADA has great potential as a SMD structure with various spin-coating solutions in fabrication processes.

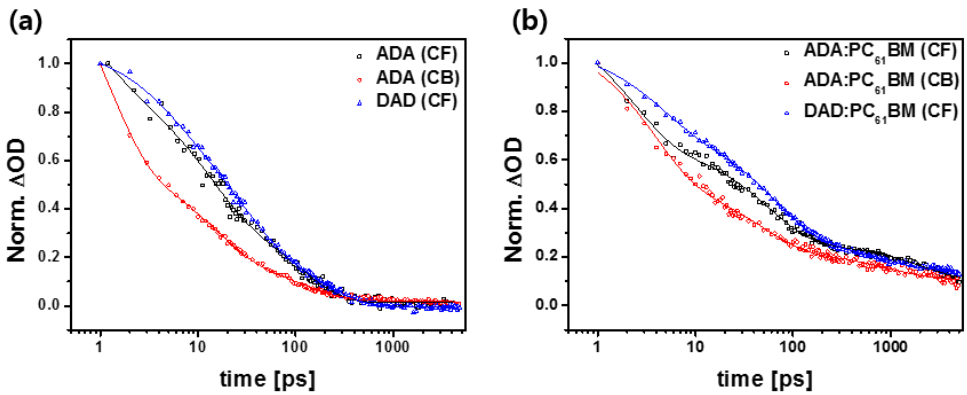

Figure 2-13 Decay profiles of donor (ADA, DAD) polaron ESA state in (a) donor neat films and (b) donor (ADA, DAD):acceptor ($PC_{61}BM$) blend films from fs-TA measurements.

Table 2-6 Time components of fs-TA using ADA neat film and ADA:$PC_{61}BM$ blend film. Both films were spin-coated using chlorobenzene solutions.

	ADA	ADA:$PC_{61}BM$
τ_1	14.2 ps (19%)	46.9 ps (10%)
τ_2	120 ps (76%)	1.00 ns (88%)

2.4. Conclusions

In conclusion, to achieve the efficient assembly of a triad SMD material using IDID donor and DPP acceptor moieties, ADA and DAD type small molecules were designed and characterized. Both ADA and DAD triad molecules show appropriate energy levels for donor materials, while ICT characters are slightly different. Based on the quantum chemical calculations, ADA exhibits stronger light absorption property than DAD because of the large orbital overlap between the delocalized HOMO and LUMO orbitals. Furthermore, strong positive solvatochromism in the steady-state optical properties and a fast CT time in the solution state fs-TA measurements confirm a strong dipolar ICT character of ADA in solution due to the spatially delocalized LUMO and abundant electron density at the end-capping DPP moieties. The transient absorption spectra of the blend films exhibit ultrafast charge separation in both ADA:$PC_{61}BM$ and DAD:$PC_{61}BM$ blend films, while the amount of generated polarons was much larger and charge carrier recombination was much slower in ADA:$PC_{61}BM$ than in the DAD:$PC_{61}BM$ blend film. As a result, solution-processed SMOSCs obtained using the ADA:$PC_{61}BM$ blend film exhibit a higher PCE, J_{SC} and V_{OC} based on strong ICT character, light absorption properties and a deeper HOMO level than DAD:$PC_{61}BM$ OSCs, confirming ADA as a favorable donor architecture in IDID-DPP OSCs.

2.5. References

[1] McDowell, C.; Abdelsamie, M.; Toney, M. F.; Bazan, G. C., Solvent Additives: Key Morphology-Directing Agents for Solution-Processed Organic Solar Cells. *Adv Mater* **2018**, *30*, 1707114.

[2] Etxebarria, I.; Ajuria, J.; Pacios, R., Solution-Processable Polymeric Solar Cells: A Review on Materials, Strategies and Cell Architectures to Overcome 10%. *Organic Electronics* **2015**, *19*, 34-60.

[3] Zhang, H.; Yao, H.; Hou, J.; Zhu, J.; Zhang, J.; Li, W.; Yu, R.; Gao, B.; Zhang, S.; Hou, J., Over 14% Efficiency in Organic Solar Cells Enabled by Chlorinated Nonfullerene Small-Molecule Acceptors. *Adv Mater* **2018**, *30*, 1800613.

[4] Che, X.; Li, Y.; Qu, Y.; Forrest, S. R., High Fabrication Yield Organic Tandem Photovoltaics Combining Vacuum- and Solution-Processed Subcells with 15% Efficiency. *Nature Energy* **2018**, *3*, 422-427.

[5] Meng, L.; Zhang, Y.; Wan, X.; Li, C.; Zhang, X.; Wang, Y.; Ke, X.; Xiao, Z.; Ding, L.; Xia, R.; et al. Organic and Solution-Processed Tandem Solar Cells with 17.3% Efficiency. *Science* **2018**, *361*, 1094-1098.

[6] Cui, Y.; Yao, H.; Zhang, J.; Zhang, T.; Wang, Y.; Hong, L.; Xian, K.; Xu, B.; Zhang, S.; Peng, J.; et al. Over 16% Efficiency Organic Photovoltaic Cells Enabled by a

Chlorinated Acceptor with Increased Open-Circuit Voltages. *Nat Commun* **2019**, *10*, 2515.

[7] Fan, B.; Zhang, D.; Li, M.; Zhong, W.; Zeng, Z.; Ying, L.; Huang, F.; Cao, Y., Achieving over 16% Efficiency for Single-Junction Organic Solar Cells. *Science China Chemistry* **2019**, *62*, 746-752.

[8] Collins, S. D.; Ran, N. A.; Heiber, M. C.; Nguyen, T.-Q., Small Is Powerful: Recent Progress in Solution-Processed Small Molecule Solar Cells. *Advanced Energy Materials* **2017**, *7*, 1602242.

[9] Kan, B.; Zhang, Q.; Li, M.; Wan, X.; Ni, W.; Long, G.; Wang, Y.; Yang, X.; Feng, H.; Chen, Y., Solution-Processed Organic Solar Cells Based on Dialkylthiol-Substituted Benzodithiophene Unit with Efficiency near 10%. *J Am Chem Soc* **2014**, *136*, 15529-15532.

[10] Kan, B.; Li, M.; Zhang, Q.; Liu, F.; Wan, X.; Wang, Y.; Ni, W.; Long, G.; Yang, X.; Feng, H.; et al. A Series of Simple Oligomer-Like Small Molecules Based on Oligothiophenes for Solution-Processed Solar Cells with High Efficiency. *J Am Chem Soc* **2015**, *137*, 3886-3893.

[11] Huo, Y.; Zhang, H.-L.; Zhan, X., Nonfullerene All-Small-Molecule Organic Solar Cells. *ACS Energy Letters* **2019**, *4*, 1241-1250.

[12] Zhou, Z.; Xu, S.; Song, J.; Jin, Y.; Yue, Q.; Qian, Y.; Liu, F.; Zhang, F.; Zhu, X., High-Efficiency Small-Molecule Ternary Solar Cells with a Hierarchical Morphology

Enabled by Synergizing Fullerene and Non-Fullerene Acceptors. *Nature Energy* **2018**, *3*, 952-959.

[13] Zhou, R.; Jiang, Z.; Yang, C.; Yu, J.; Feng, J.; Adil, M. A.; Deng, D.; Zou, W.; Zhang, J.; Lu, K.; et al. All-Small-Molecule Organic Solar Cells with over 14% Efficiency by Optimizing Hierarchical Morphologies. *Nat Commun* **2019**, *10*, 5393.

[14] Gao, K.; Jo, S. B.; Shi, X.; Nian, L.; Zhang, M.; Kan, Y.; Lin, F.; Kan, B.; Xu, B.; Rong, Q.; et al. Over 12% Efficiency Nonfullerene All-Small-Molecule Organic Solar Cells with Sequentially Evolved Multilength Scale Morphologies. *Adv Mater* **2019**, *31*, 1807842.

[15] Xu, S.; Zhou, Z.; Fan, H.; Ren, L.; Liu, F.; Zhu, X.; Russell, T. P., An Electron-Rich 2-Alkylthieno[3,4-b]thiophene Building Block with Excellent Electronic and Morphological Tunability for High-Performance Small-Molecule Solar Cells. *Journal of Materials Chemistry A* **2016**, *4*, 17354-17362.

[16] Lee, C. J.; Mitchell, V. D.; White, J.; Jiao, X.; McNeill, C. R.; Subbiah, J.; Jones, D. J., Solubilizing Core Modifications on High-Performing Benzodithiophene-Based Molecular Semiconductors and Their Influences on Film Nanostructure and Photovoltaic Performance. *Journal of Materials Chemistry A* **2019**, *7*, 6312-6326.

[17] Xiao, L.; Lai, T.; Liu, X.; Liu, F.; Russell, T. P.; Liu, Y.; Huang, F.; Peng, X.; Cao, Y., A Low-Bandgap Dimeric Porphyrin Molecule for 10% Efficiency Solar Cells with Small Photon Energy Loss. *Journal of Materials Chemistry A* **2018**, *6*, 18469-18478.

[18] Deng, D.; Zhang, Y.; Zhang, J.; Wang, Z.; Zhu, L.; Fang, J.; Xia, B.; Wang, Z.; Lu, K.; Ma, W.; et al. Fluorination-Enabled Optimal Morphology Leads to over 11% Efficiency for Inverted Small-Molecule Organic Solar Cells. *Nat Commun* **2016**, *7*, 13740.

[19] Li, M.; Gao, K.; Wan, X.; Zhang, Q.; Kan, B.; Xia, R.; Liu, F.; Yang, X.; Feng, H.; Ni, W.; et al. Solution-Processed Organic Tandem Solar Cells with Power Conversion Efficiencies >12%. *Nature Photonics* **2016**, *11*, 85-90.

[20] Ilmi, R.; Haque, A.; Khan, M. S., High Efficiency Small Molecule-Based Donor Materials for Organic Solar Cells. *Organic Electronics* **2018**, *58*, 53-62.

[21] He, X.; Yin, L.; Li, Y., Design of Organic Small Molecules for Photovoltaic Application with High Open-Circuit Voltage (*V*oc). *Journal of Materials Chemistry C* **2019**, *7*, 2487-2521.

[22] Roncali, J.; Leriche, P.; Blanchard, P., Molecular Materials for Organic Photovoltaics: Small Is Beautiful. *Adv Mater* **2014**, *26*, 3821-3838.

[23] Chen, Y.; Wan, X.; Long, G., High Performance Photovoltaic Applications Using Solution-Processed Small Molecules. *Accounts of Chemical Research* **2013**, *46*, 2645-2655.

[24] Cho, H.-H.; Kim, S.; Kim, T.; Sree, V. G.; Jin, S.-H.; Kim, F. S.; Kim, B. J., Design of Cyanovinylene-Containing Polymer Acceptors with Large Dipole Moment Change for Efficient Charge Generation in High-Performance All-Polymer Solar Cells. *Advanced Energy Materials* **2018**, *8*, 1701436.

[25] Turan, H. T.; Kucur, O.; Kahraman, B.; Salman, S.; Aviyente, V., Design of Donor-Acceptor Copolymers for Organic Photovoltaic Materials: A Computational Study. *Phys Chem Chem Phys* **2018**, *20*, 3581-3591.

[26] Casey, A.; Dimitrov, S. D.; Shakya-Tuladhar, P.; Fei, Z.; Nguyen, M.; Han, Y.; Anthopoulos, T. D.; Durrant, J. R.; Heeney, M., Effect of Systematically Tuning Conjugated Donor Polymer Lowest Unoccupied Molecular Orbital Levels Via Cyano Substitution on Organic Photovoltaic Device Performance. *Chemistry of Materials* **2016**, *28*, 5110-5120.

[27] Carsten, B.; Szarko, J. M.; Lu, L.; Son, H. J.; He, F.; Botros, Y. Y.; Chen, L. X.; Yu, L., Mediating Solar Cell Performance by Controlling the Internal Dipole Change in Organic Photovoltaic Polymers. *Macromolecules* **2012**, *45*, 6390-6395.

[28] Szarko, J. M.; Rolczynski, B. S.; Lou, S. J.; Xu, T.; Strzalka, J.; Marks, T. J.; Yu, L. P.; Chen, L. X., Photovoltaic Function and Exciton/Charge Transfer Dynamics in a Highly Efficient Semiconducting Copolymer. *Advanced Functional Materials* **2014**, *24*, 10-26.

[29] Rolczynski, B. S.; Szarko, J. M.; Son, H. J.; Liang, Y.; Yu, L.; Chen, L. X., Ultrafast Intramolecular Exciton Splitting Dynamics in Isolated Low-Band-Gap Polymers and Their Implications in Photovoltaic Materials Design. *J Am Chem Soc* **2012**, *134*, 4142-4152.

[30] Carsten, B.; Szarko, J. M.; Son, H. J.; Wang, W.; Lu, L.; He, F.; Rolczynski, B. S.; Lou, S. J.; Chen, L. X.; Yu, L., Examining the Effect of the Dipole Moment on Charge

Separation in Donor-Acceptor Polymers for Organic Photovoltaic Applications. *J Am Chem Soc* **2011**, *133*, 20468-20475.

[31] Lee, H.; Park, C.; Sin, D. H.; Park, J. H.; Cho, K., Recent Advances in Morphology Optimization for Organic Photovoltaics. *Advanced Materials* **2018**, *30*, 1800453.

[32] Zhao, F.; Wang, C.; Zhan, X., Morphology Control in Organic Solar Cells. *Advanced Energy Materials* **2018**, *8*, 1703147.

[33] Hedley, G. J.; Ward, A. J.; Alekseev, A.; Howells, C. T.; Martins, E. R.; Serrano, L. A.; Cooke, G.; Ruseckas, A.; Samuel, I. D. W., Determining the Optimum Morphology in High-Performance Polymer-Fullerene Organic Photovoltaic Cells. *Nature Communications* **2013**, *4*, 2867.

[34] Wang, Z.; Song, C.; Li, J.; Li, P.; Zhang, H., Modulation of Electron-Donating Ability in D–A–A Small Molecules for Application in Organic Solar Cells. *The Journal of Physical Chemistry C* **2018**, *123*, 1069-1081.

[35] Carlotti, B.; Cai, Z.; Kim, H.; Sharapov, V.; Madu, I. K.; Zhao, D.; Chen, W.; Zimmerman, P. M.; Yu, L.; Goodson, T., Charge Transfer and Aggregation Effects on the Performance of Planar vs Twisted Nonfullerene Acceptor Isomers for Organic Solar Cells. *Chemistry of Materials* **2018**, *30*, 4263-4276.

[36] Yan, C.; Barlow, S.; Wang, Z.; Yan, H.; Jen, A. K. Y.; Marder, S. R.; Zhan, X., Non-Fullerene Acceptors for Organic Solar Cells. Nature Reviews Materials 2018, 3, 18003.

[37] Cao, W.; Xue, J., Recent Progress in Organic Photovoltaics: Device Architecture and Optical Design. *Energy & Environmental Science* **2014**, *7*, 2123-2144.

[38] Zhang, G.; Zhang, K.; Yin, Q.; Jiang, X. F.; Wang, Z.; Xin, J.; Ma, W.; Yan, H.; Huang, F.; Cao, Y., High-Performance Ternary Organic Solar Cell Enabled by a Thick Active Layer Containing a Liquid Crystalline Small Molecule Donor. *J Am Chem Soc* **2017**, *139*, 2387-2395.

[39] Zhang, C.; Zhu, X., Thieno[3,4-b]thiophene-Based Novel Small-Molecule Optoelectronic Materials. *Acc Chem Res* **2017**, *50*, 1342-1350.

[40] Huo, Y.; Gong, X.-T.; Lau, T.-K.; Xiao, T.; Yan, C.; Lu, X.; Lu, G.; Zhan, X.; Zhang, H.-L., Dual-Accepting-Unit Design of Donor Material for All-Small-Molecule Organic Solar Cells with Efficiency Approaching 11%. *Chemistry of Materials* **2018**, *30*, 8661-8668.

[41] Yang, L.; Zhang, S.; He, C.; Zhang, J.; Yao, H.; Yang, Y.; Zhang, Y.; Zhao, W.; Hou, J., New Wide Band Gap Donor for Efficient Fullerene-Free All-Small-Molecule Organic Solar Cells. *J Am Chem Soc* **2017**, *139*, 1958-1966.

[42] Li, K.; Khlyabich, P. P.; Li, L.; Burkhart, B.; Thompson, B. C.; Campbell, J. C., Influence of Exciton Diffusion and Charge-Transfer State Dissociation Efficiency on the Short-Circuit Current Densities in Semi-Random Donor/Acceptor Polymer:Fullerene Solar Cells. *The Journal of Physical Chemistry C* **2013**, *117*, 6940-6948.

[43] Cho, I.; Park, S. K.; Kang, B.; Chung, J. W.; Kim, J. H.; Cho, K.; Park, S. Y., Design, Synthesis, and Versatile Processing of Indolo[3,2-b]indole-Based π-Conjugated Molecules for High-Performance Organic Field-Effect Transistors. *Advanced Functional Materials* **2016**, *26*, 2966-2973.

[44] Hwang, J.; Park, J.; Kim, Y. J.; Ha, Y. H.; Park, C. E.; Chung, D. S.; Kwon, S.-K.; Kim, Y.-H., Indolo[3,2-b]indole-Containing Donor–Acceptor Copolymers for High-Efficiency Organic Solar Cells. *Chemistry of Materials* **2017**, *29*, 2135-2140.

[45] Cho, I.; Jeon, N. J.; Kwon, O. K.; Kim, D. W.; Jung, E. H.; Noh, J. H.; Seo, J.; Seok, S. I.; Park, S. Y., Indolo[3,2-b]indole-Based Crystalline Hole-Transporting Material for Highly Efficient Perovskite Solar Cells. *Chem Sci* **2017**, *8*, 734-741.

[46] Ryoo, C. H.; Cho, I.; Han, J.; Yang, J. H.; Kwon, J. E.; Kim, S.; Jeong, H.; Lee, C.; Park, S. Y., Structure-Property Correlation in Luminescent Indolo[3,2-b]indole (IDID) Derivatives: Unraveling the Mechanism of High Efficiency Thermally Activated Delayed Fluorescence (TADF). *ACS Appl Mater Interfaces* **2017**, *9*, 41413-41420.

[47] Lai, Y.-Y.; Yeh, J.-M.; Tsai, C.-E.; Cheng, Y.-J., Synthesis, Molecular and Photovoltaic Properties of an Indolo[3,2-b]indole-Based Acceptor-Donor-Acceptor Small Molecule. *European Journal of Organic Chemistry* **2013**, *2013*, 5076-5084.

[48] Owczarczyk, Z. R.; Braunecker, W. A.; Garcia, A.; Larsen, R.; Nardes, A. M.; Kopidakis, N.; Ginley, D. S.; Olson, D. C., 5,10-Dihydroindolo[3,2-b]indole-Based Copolymers with Alternating Donor and Acceptor Moieties for Organic Photovoltaics. *Macromolecules* **2013**, *46*, 1350-1360.

[49] Yoon, W. S.; Park, S. K.; Cho, I.; Oh, J.-A.; Kim, J. H.; Park, S. Y., High-Mobility n-Type Organic Transistors Based on a Crystallized Diketopyrrolopyrrole Derivative. *Advanced Functional Materials* **2013**, *23*, 3519-3524.

[50] Suppan, P., Invited Review Solvatochromic Shifts: The Influence of the Medium on the Energy of Electronic States. *Journal of Photochemistry and Photobiology A: Chemistry* **1990**, *50*, 293-330.

[51] Ghoneim, N.; Suppan, P., Solvatochromic Shifts of Non-Dipolar Molecules in Polar Solvents. *Spectrochimica Acta Part A: Molecular and Biomolecular Spectroscopy* **1995**, *51*, 1043-1050.

[52] Renge, I., Refractive Index Dependence of Solvatochromism. *Journal of Photochemistry and Photobiology A: Chemistry* **2018**, *353*, 433-444.

[53] Kim, W.; Sung, J.; Grzybowski, M.; Gryko, D. T.; Kim, D., Modulation of Symmetry-Breaking Intramolecular Charge-Transfer Dynamics Assisted by Pendant Side Chains in π-Linkers in Quadrupolar Diketopyrrolopyrrole Derivatives. *J Phys Chem Lett* **2016**, *7*, 3060-3066.

[54] Zhu, H.; Li, M.; Hu, J.; Wang, X.; Jie, J.; Guo, Q.; Chen, C.; Xia, A., Ultrafast Investigation of Intramolecular Charge Transfer and Solvation Dynamics of Tetrahydro[5]-helicene-Based Imide Derivatives. *Scientific Reports* **2016**, *6*, 24313.

[55] He, G.; Zhou, L.-L.; Song, H.; Kuang, Z.; Wang, X.; Guo, Q.; Lu, H.-Y.; Xia, A., Insights into the Effect of Donor Ability on Photophysical Properties of Dihydroindeno[2,1-c]fluorene-Based Imide Derivatives. *Physical Chemistry Chemical Physics* **2018**, *20*, 7514-7522.

[56] Demissie, E. G.; Mengesha, E. T.; Woyessa, G. W., Modified Solvatochromic Equations for Better Estimation of Ground and Excited State Dipole Moments of p-

Aminobenzoicacid (PABA): Accounting for Real Shape over Hypothetical Spherical Solvent Shell. *Journal of Photochemistry and Photobiology A: Chemistry* **2017**, *337*, 184-191.

[57] Mukherjee, S.; Chattopadhyay, A.; Samanta, A.; Soujanya, T., Dipole Moment Change of NBD Group Upon Excitation Studied Using Solvatochromic and Quantum Chemical Approaches: Implications in Membrane Research. *The Journal of Physical Chemistry* **1994**, *98*, 2809-2812.

[58] Vázquez, M. E.; Blanco, J. B.; Imperiali, B., Photophysics and Biological Applications of the Environment-Sensitive Fluorophore 6-N,N-Dimethylamino-2,3-naphthalimide. *Journal of the American Chemical Society* **2005**, *127*, 1300-1306.

[59] Ricci, F.; Elisei, F.; Foggi, P.; Marrocchi, A.; Spalletti, A.; Carlotti, B., Photobehavior and Nonlinear Optical Properties of Push–Pull, Symmetrical, and Highly Fluorescent Benzothiadiazole Derivatives. *The Journal of Physical Chemistry C* **2016**, *120*, 23726-23739.

[60] He, G.; Shao, J.; Li, Y.; Hu, J.; Zhu, H.; Wang, X.; Guo, Q.; Chi, C.; Xia, A., Photophysical Properties of Octupolar Triazatruxene-Based Chromophores. *Phys Chem Chem Phys* **2016**, *18*, 6789-6798.

[61] Terenziani, F.; Painelli, A.; Katan, C.; Charlot, M.; Blanchard-Desce, M., Charge Instability in Quadrupolar Chromophores: Symmetry Breaking and Solvatochromism. *Journal of the American Chemical Society* **2006**, *128*, 15742-15755.

[62] Kim, T.; Kim, J.; Mori, H.; Park, S.; Lim, M.; Osuka, A.; Kim, D., Symmetry-Breaking Charge Transfer in the Excited State of Directly Linked Push-Pull Porphyrin Arrays. *Phys Chem Chem Phys* **2017**, *19*, 13970-13977.

[63] Kim, T.; Kim, W.; Mori, H.; Osuka, A.; Kim, D., Solvent and Structural Fluctuations Induced Symmetry-Breaking Charge Transfer in a Porphyrin Triad. *The Journal of Physical Chemistry C* **2018**, *122*, 19409-19415.

[64] Dereka, B.; Vauthey, E., Solute-Solvent Interactions and Excited-State Symmetry Breaking: Beyond the Dipole-Dipole and the Hydrogen-Bond Interactions. *J Phys Chem Lett* **2017**, *8*, 3927-3932.

[65] Dereka, B.; Rosspeintner, A.; Stezycki, R.; Ruckebusch, C.; Gryko, D. T.; Vauthey, E., Excited-State Symmetry Breaking in a Quadrupolar Molecule Visualized in Time and Space. *J Phys Chem Lett* **2017**, *8*, 6029-6034.

[66] Soderberg, M.; Dereka, B.; Marrocchi, A.; Carlotti, B.; Vauthey, E., Ground-State Structural Disorder and Excited-State Symmetry Breaking in a Quadrupolar Molecule. *J Phys Chem Lett* **2019**, *10*, 2944-2948.

[67] Mitsui, M.; Takakura, Y.; Niihori, Y.; Nakamoto, M.; Fujiwara, Y.; Kobayashi, K., Excited-State Symmetry Breaking of a Symmetrical Donor−π–Donor Quadrupolar Molecule at a Polymer/Glass Interface. *The Journal of Physical Chemistry C* **2019**, *123*, 14564-14572.

[68] Stoltzfus, D. M.; Donaghey, J. E.; Armin, A.; Shaw, P. E.; Burn, P. L.; Meredith, P., Charge Generation Pathways in Organic Solar Cells: Assessing the Contribution from the Electron Acceptor. *Chem Rev* **2016**, *116*, 12920-12955.

[69] Clarke, T. M.; Durrant, J. R., Charge Photogeneration in Organic Solar Cells. *Chemical Reviews* **2010**, *110*, 6736-6767.

[70] Ohkita, H.; Cook, S.; Astuti, Y.; Duffy, W.; Tierney, S.; Zhang, W.; Heeney, M.; McCulloch, I.; Nelson, J.; Bradley, D. D. C.; et al. Charge Carrier Formation in Polythiophene/Fullerene Blend Films Studied by Transient Absorption Spectroscopy. *Journal of the American Chemical Society* **2008**, *130*, 3030-3042.

[71] Vandewal, K.; Albrecht, S.; Hoke, E. T.; Graham, K. R.; Widmer, J.; Douglas, J. D.; Schubert, M.; Mateker, W. R.; Bloking, J. T.; Burkhard, G. F.; et al. Efficient Charge Generation by Relaxed Charge-Transfer States at Organic Interfaces. *Nat Mater* **2014**, *13*, 63-68.

[72] Grancini, G.; Maiuri, M.; Fazzi, D.; Petrozza, A.; Egelhaaf, H. J.; Brida, D.; Cerullo, G.; Lanzani, G., Hot Exciton Dissociation in Polymer Solar Cells. *Nat Mater* **2013**, *12*, 29-33.

[73] Liu, X.; Rand, B. P.; Forrest, S. R., Engineering Charge-Transfer States for Efficient, Low-Energy-Loss Organic Photovoltaics. *Trends in Chemistry* **2019**, *1*, 815-829.

[74] Bartynski, A. N.; Gruber, M.; Das, S.; Rangan, S.; Mollinger, S.; Trinh, C.; Bradforth, S. E.; Vandewal, K.; Salleo, A.; Bartynski, R. A.; et al. Symmetry-Breaking

Charge Transfer in a Zinc Chlorodipyrrin Acceptor for High Open Circuit Voltage Organic Photovoltaics. *J Am Chem Soc* **2015**, *137*, 5397-5405.

[75] Ji, Z.; Xu, X.; Zhang, G.; Li, Y.; Peng, Q., Synergistic Effect of Halogenation on Molecular Energy Level and Photovoltaic Performance Modulations of Highly Efficient Small Molecular Materials. *Nano Energy* **2017**, *40*, 214-223.

[76] Deng, D.; Yang, Y.; Zou, W.; Zhang, Y.; Wang, Z.; Wang, Z.; Zhang, J.; Lu, K.; Ma, W.; Wei, Z., Aromatic End-Capped Acceptor Effects on Molecular Stacking and the Photovoltaic Performance of Solution-Processable Small Molecules. *Journal of Materials Chemistry A* **2018**, *6*, 22077-22085.

Chapter 3.

Influence of Intramolecular Charge Transfer Character on Polaron Generation at Donor/Acceptor Interface in Polymer Solar Cells

3.1. Introduction

In polymer solar cells (PSCs), photoinduced charge separation is a very important step among the whole operating processes, and understanding the mechanism of charge separation is crucial for obtaining high performance PSCs. [1] It has been proposed that the charge separation is affected by several factors, such as the energetics and disorder at D/A interface, charge delocalization, and blend morphology of bulk heterojunction (BHJ). [2-6] In particular, the role of interfacial charge transfer (CT) state on charge generation has drawn substantial interest in understanding the mechanism of converting excitons into free charge carriers. The CT state, consisting of Coulombically bound electron and hole pair, is the result of photoinduced charge transfer at the interface of donor and acceptor materials. [7-8] Recently, it has been proposed that charge separation is greatly influenced by the energetics of CT states, leading to the different charge separation pathway through hot or relaxed (cold) CT states. Several researchers have

reported the efficient charge separation through the electronically and/or vibrationally excited and delocalized CT state. [8-12] Hot CT state refers to a loosely bound and delocalized electron-hole pair, facilitating the charge separation at D/A interface. Numerous experiments have suggested that the sufficient energy of hot CT state is beneficial for overcoming the Coulomb barrier and avoiding geminate recombination. [3,7,10-14] For instance, Grancini et al. reported that efficient charge separation occurs before the relaxation within CT states in PCPDTBT/$PC_{60}BM$ blend with the aid of hot and delocalized CT state, and Bakulin et al. also offered the clear evidence of exciton dissociation through hot CT states enabling long range charge separation. [9,12] Hot charge separation process was also supported through the temperature-independent polaron generation dynamics. [4,10] However, another scenario for the charge separation in PSCs is also proposed that the lowest (cold) CT state acts as a precursor for the charge separation because of the fast internal conversion/relaxation process, where the hot CT state is no longer important. Excitation energy independent internal quantum efficiency (IQE) of the photovoltaic device supports the hypothesis that the excess energy is not necessary for the efficient charge separation and emphasize the importance of cold CT state dissociation. [15-18] Thus, the role of hot CT state on charge separation is still unclear and subjected to the ongoing debate. At this moment, therefore, it is very important to determine whether charge separation is via hot or cold process for developing organic materials and obtaining high efficiency PSCs.

In this regard, we focused on a comparative set of polymers, push-pull type

copolymer and homopolymer, for determining the role of hot or cold CT states on the charge separation mechanism. The copolymer PTB7 exhibits an initially photoexcited exciton with intramolecular charge transfer (ICT) characteristics due to the push-pull action between neighboring building blocks, resulting in the partial electron density displacement. It is well known that the ICT characteristics in the delocalized exciton results in the weaker binding energy compared with the conventional excitonic configuration. [19-20] On the other hand, the P3HT homopolymer forms the delocalized exciton between identical repeating units with negligible ICT characteristics. [21]Therefore, such different structural aspects in donor polymers with different ICT characteristics and delocalization of exciton are expected to result in different wave function distribution and charge separation, which is yet to be established in this work. It is to be stressed that understanding the influence of polymer design on hot charge separation process is important for obtaining efficient charge separation and developing organic materials and obtaining high efficiency PSCs.

The charge separation pathway with the excess energy in the blend systems was compared using the push-pull type copolymer PTB7 possessing initially excited delocalized exciton with ICT characteristics, and homopolymer P3HT possessing delocalized exciton with negligible ICT characteristics but partly forming inter-chain polaron pair. The polaron pair in P3HT is known to have charge-transfer characteristics, however, somewhat different from the ICT excitonic characteristics in PTB7. In P3HT, polarons are generated from the hot exciton within ultrafast time scale and stabilized to

form inter-chain polaron pairs with a Coulomb interaction, while ICT state of PTB7 is originated from partial charge transfer due to the difference in electron affinity between electron-donating and accepting units. [21] Thus, the formation of polaron pair is subsequent to the hot exciton formation in P3HT. Both PTB7:NIDCSEO3 and P3HT:NIDCSEO3 blends exhibited strong π-π stacking in both D and A regions with highly crystalline NIDCSEO3 acceptor with oligo(ethylene glycol) (OEG) side chains, which is favorable for the exciton delocalization within D and A regions and following charge separation at the D/A interface. [22-27] Thus, we could induce the ideal π-π stacked blend morphology and rule out the morphological effect in comparing the charge separation in PTB7:NIDCSEO3 and P3HT:NIDCSEO3 systems, and focus our interest on the intrinsic characteristics of polymer exciton and relevant charge separation mechanism at the D/A interface. Through the temperature- and pump-dependent transient absorption measurements, different charge separation mechanisms in PTB7:NIDCSEO3 and P3HT:NIDCSEO3 were thoroughly investigated. PTB7:NIDCSEO3 blend exhibited ultrafast charge separation through the delocalized exciton state with ICT characteristics exclusively in the hot CT state. On the other hand, P3HT:NIDCSEO3 exhibited combined hot and cold charge separation processes despite the formation of delocalized exciton in P3HT, owing to the ultrafast relaxation of hot exciton of P3HT to the polaron pair state. This result suggests that the role of excess energy in charge generation in PSCs should be precisely correlated to the intrinsic excitonic character of the donor polymer.

3.2. Experimental Section

3.2.1. General

UV–vis absorption spectra were measured with a UV-1650 PC (Shimadzu) spectrometer and photoluminescence emission spectra were measured using a Felix32 QM-40 (Photo Technology International) and a Cary Eclipse (Varian) fluorescence spectrophotometer; the emission spectra were corrected for the sensitivity of the photomultiplier. The cyclic voltammetry experiments were carried out using a 273A (Princeton Applied Research) with a three electrode cell assembly including an ITO-coated glass working electrode, a platinum wire counter electrode, and a quasi Ag^{+}/Ag electrode as a reference electrode. Measurements were performed in a 0.1 M acetonitrile solution with tetrabutylammonium hexafluorophosphate (TBAHFP) as the supporting electrolyte at a scan rate of 100 mV/s. The HOMO and LUMO levels were estimated based on the onset of oxidation and reduction potential using ferrocene as a reference. The 2D-GIXD measurements were made at the 3C SAXS beam line (E=10.00 keV) in the Pohang Accelerator Laboratory (PAL) in Korea.

3.2.2. Femtosecond transient absorption spectroscopy

The femtosecond time-resolved transient absorption (fs-TA) spectrometer consisted of Optical Parametric Amplifiers (Palitra, Quantronix) pumped by a Ti:sapphire regenerative amplifier system (Integra-C, Quantronix) operating at 1 kHz repetition rate and an optical detection system. The generated OPA pulses, which were used as pump pulses, had a pulse width of ~ 100 fs and an average power of 100 mW in the range 550-690 nm. White light continuum (WLC) probe pulses were generated using a sapphire window by focusing of small portion of the fundamental 800 nm pulses which was picked off by a quartz plate before entering to the OPA. The time delay between pump and probe beams was carefully controlled by making the pump beam travel along a variable optical delay (ILS250, Newport). Intensities of the spectrally dispersed WLC probe pulses are monitored by a high Speed spectrometer (Ultrafast Systems). To obtain the time-resolved transient absorption difference signal at a specific time, the pump pulses were chopped at 500 Hz and absorption spectra intensities were saved alternately with or without pump pulse. Typically, 6000 pulses excite samples to obtain the fs-TA spectra at a particular delay time. The polarization angle between pump and probe beam was set at the magic angle (54.7°) using a Glan-laser polarizer with a half-wave retarder in order to prevent polarization-dependent signals. Cross-correlation fwhm in pump-

probe experiments was less than 200 fs and chirp of WLC probe pulses was measured to be 800 fs in the 450-850 nm region.

3.2.3. Device fabrication and characterization

Devices were fabricated to the ITO/PEDOT:PSS/active layer/Ca/Al configuration. The patterned indium tin oxide (ITO) glass substrates were cleaned in an ultrasonic bath with acetone, and isopropanol, and then exposed to a UV/O_3 for 20 min. PEDOT:PSS (Clavious P VP AI 4083) was spin-coated onto the ITO glass substrate at 5000 rpm for 30 s and the film was subsequently baked at 150 °C for 20 min. A PTB7:NIDCSEO3 (1:2.5 ratio) in chlorobenzene with 1-CN (4 vol%) solution (totally 25 mg/mL concentration) or P3HT:NIDCSEO3 (1:2.5 ratio) in chlorobenzene solution (totally 20 mg/mL concentration) was subsequently spin-coated (1500 rpm) on the PEDOT:PSS coated ITO glass to form active layer (ca. 80 nm). After drying the resulting films in a N2 glovebox at room temperature for 30 min, thermal annealing treatment was conducted on the P3HT:NIDCSOE3 device at 90 °C for 20 min. Then, Ca (6 nm) was thermally deposited on photoactive layer under a vacuum of 10^{-6} torr. Finally, Al (100 nm) was thermally deposited under a vacuum of 10^{-6} torr.

The current density–voltage (*J–V*) characteristics of the solar cells were measured suing a Keithley 4200 source measurement unit. The solar cell performances were

characterized under AM 1.5G condition with an illumination intensity of 100 mW/cm^2, as generated using an Oriel Sol3A solar simulator (Oriel model 9023A). The measurements were carried out through a shadow mask with well-defined aperture area of 0.05 cm^2 under an ambient atmosphere. The IPCE spectra of devices were examined using Oriel QE/IPCE Measurement Kit comprised of a 300 W Xe lamp, monochromater (94125), a Merlin lock-in amplifier (70104), an optical chopper under ambient conditions. A standard silicon solar cell (70356_70316NS) was used as a reference to determine the light intensity at each wavelength. A standard silicon solar cell (70356_70316NS) was used as a reference to determine the light intensity at each wavelength.

3.3. Result and Discussion

Figure 3-1 shows the chemical structures of donor and acceptor materials used in this research. Commonly used donor polymers, poly(3-fluorothienothiophenebenzodithiophene) (PTB7) and poly(3-hexythiophene) (P3HT), were used as donor materials because of their different intrinsic electronic characteristics. PTB7 has an intramolecular charge-transfer (ICT) type conjugated copolymer structure composed of BDT and TT building blocks, while P3HT is composed of hexylthiophene repeating units. This difference in chemical structures induces differences in exciton

characteristics and charge separation mechanism in organic photovoltaic devices. (*vide infra*) As an acceptor, a highly crystalline dicyanodistyrylbenzene-based nonfullerene acceptor NIDCSEO3 with OEG side chains on the NIDCS backbone was employed, of which the solubility in various aromatic solvents is excellent to give the high quality PSC devices. [25,28-29] Importantly, the π-π stacking of acceptor material and thus the crystallinity of resulting film is highly enhanced due to the flexible OEG chains, giving an ideal D:A blend morphology in the photoactive layer.

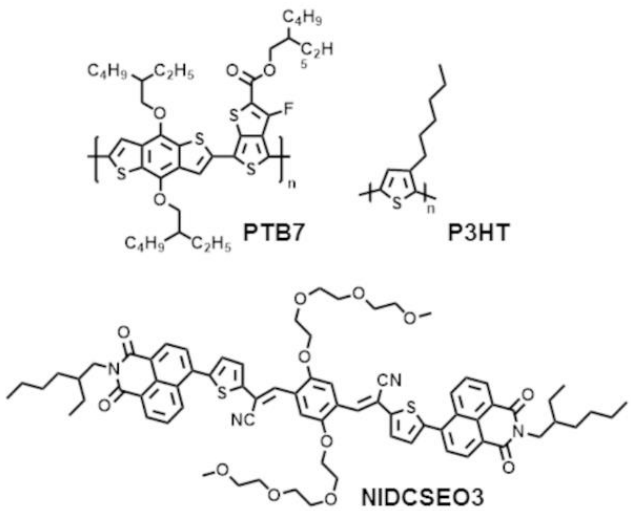

Figure 3-1 Chemical structures of PTB7, P3HT, and NIDCSEO3.

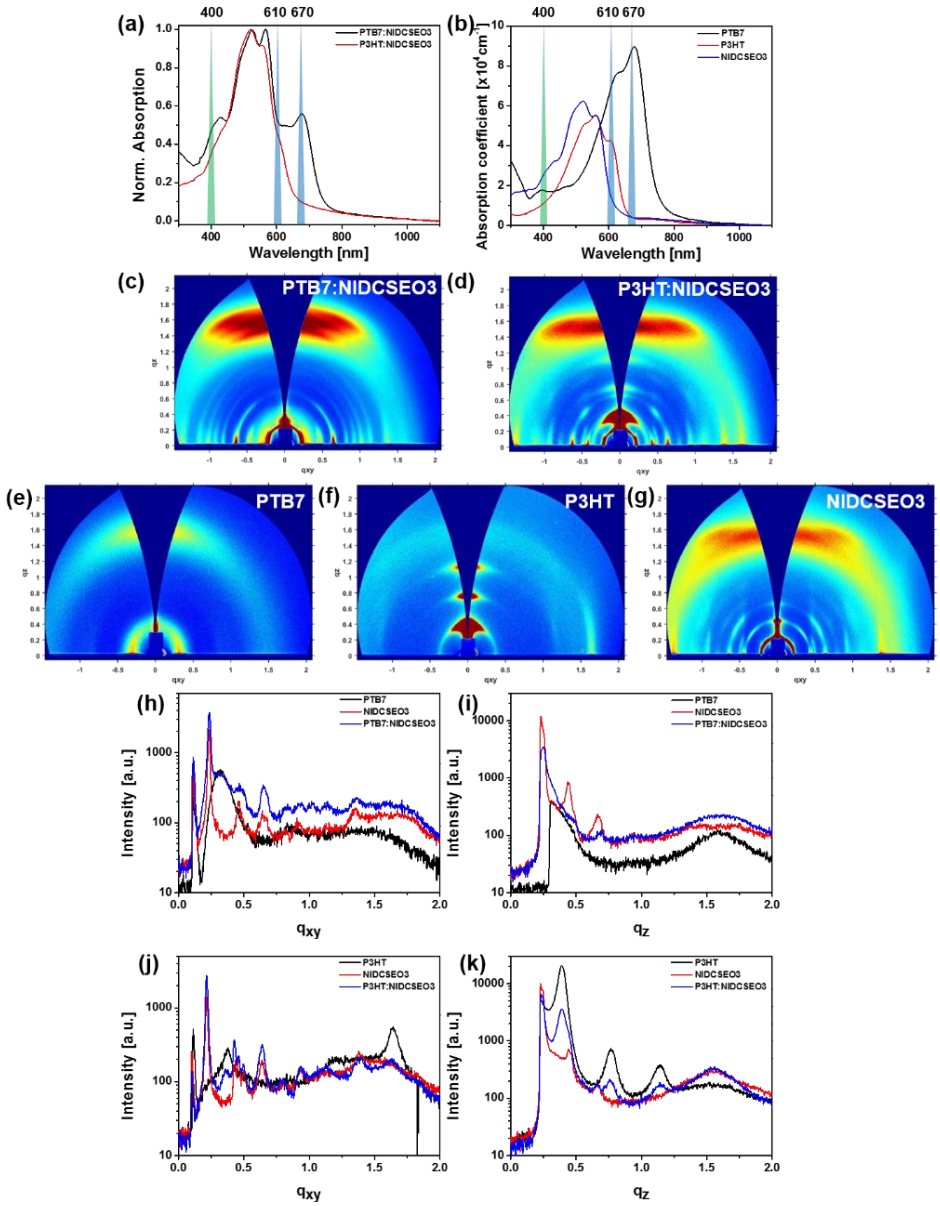

Figure 3-2 Steady-state absorption spectra of (a) PTB7:NIDCSEO3 and P3HT:NIDCSEO3 blend films and (b) PTB7, P3HT, and NIDCSEO3 neat films, and the GIWAXS images of (c) PTB7:NIDCSEO3 and (d) P3HT:NIDCSEO3. The GIWAXS images of (e) PTB7, (f) P3HT and (g) NIDCSEO3 neat films and the line cut of profiles in the (h,j) in-plane and (i,k) out-of-plane directions for the neat and blend films.

The steady-state absorption spectra of donor (PTB7, P3HT), acceptor (NIDCSEO3), and their blend (PTB7:NIDCSEO3 and P3HT:NIDCSEO3) films prepared under the same processing condition of optimized photovoltaic devices are shown in Figure 3-2a,b. Due to the push-pull structure and consequently strong ICT character, PTB7 has a narrower bandgap and a broader absorption spectrum maximum at 670 nm compared to those of P3HT possessing the 0-0 absorption vibronic band at 610 nm. The acceptor NIDCSEO3 film exhibits strong absorption in the wavelength range of 350-600 nm, which is more complementary to the PTB7 absorption spectrum. In consequence, PTB7:NIDCSEO3 blend exhibits broader absorption than P3HT:NIDCSEO3, beneficial for light absorbing property in PSCs. However, the photocurrent is affected not only by the light absorption but also by charge separation and collection efficiencies in BHJs. Therefore, understanding the charge generation mechanism in the blend system is very important for increasing short-circuit current (J_{SC}) and obtaining high efficiency photovoltaic devices.

To further understand the molecular stacking in the blend systems, the grazing-incidence wide-angle X-ray scattering (GIWAXS) measurements were performed in neat and blend films. (Figure 3-2) In the PTB7:NIDCSEO3 blend film, PTB7 exhibits the strong π-π scattering peak in the out-of-plane (OOP) direction ($q_z \sim 1.58$ Å^{-1}) with the face-on orientation, and NIDCSEO3 shows also strong π-π scattering peak in the OOP direction ($q_z \sim 1.67$ Å^{-1}) and lamellar peaks in the in-plane (IP) direction ($q_{xy} \sim 0.24$, 0.46, 0.65 Å^{-1}) owing to their highly crystalline property. The π-π stacked structures of D and

A materials in PTB7:NIDCSEO3 are favorable for the exciton delocalization within the domains. The P3HT:NIDCSEO3 blend also exhibits π-π ordered regions. Crystalline P3HT exhibits (*h*00) lamellar peaks in the OOP direction (q_z ~ 0.39, 0.77, 1.14 Å^{-1}) and π-π scattering peak in the IP direction (q_{xy} ~ 1.64 Å^{-1}) and NIDCSEO3 displays mixed edge-on and face-on bimodal orientation with π-π scattering peak in the OOP direction (q_z ~ 1.54 Å^{-1}) in P3HT:NIDCSEO3. Namely, both PTB7:NIDCSEO3 and P3HT:NIDCSEO3 films exhibit blend morphology possessing strong π-π ordered D and A regions, which is favorable for the exciton delocalization and charge separation at the D/A interface in PSCs. [26-27,30] Therefore, with the ideal blend morphology for exciton delocalization, we can rule out the morphological effect in comparing the charge separation in the BHJs, and thus the primarily generated exciton character in donor polymers based on their chemical structure is the dominant factor affecting the charge generation at the D/A interface.

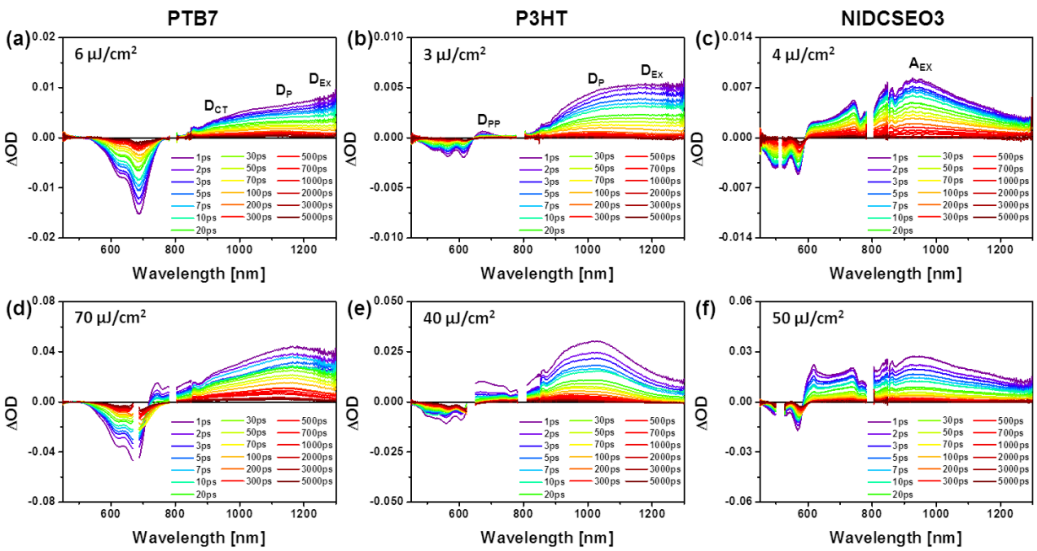

Figure 3-3 Femtosecond TA spectra of (a,d) PTB7, (b,e) P3HT, and (c,f) NIDCSEO3 films at different laser fluences.

To explore the exciton and charge carrier dynamics in the photoactive layer of BHJ PSCs, the femtosecond transient absorption (fs-TA) measurements were made for the neat and blend films using a time resolution of 200 fs laser. The TA spectra of the neat films are shown in Figure 3-3, which were measured upon the excitation at 670 nm for PTB7, 610 nm for P3HT, and 510 nm for NIDCSEO3 neat film to be in resonance with the $S_0 \rightarrow S_1$ transition, respectively. As the previous studies for PTB7 reported, the TA spectra of PTB7 exhibit broad excited state absorption (ESA) bands beyond 750 nm, where characteristic absorption bands for the singlet exciton (D_{EX}), polaron (D_P), and ICT state (D_{CT}) are centered at 1300 nm, 1150 nm, and 930 nm, respectively. [20,31] The assignment of TA spectra of P3HT was also reported in previous papers with ground-state bleaching (GSB) in the 450-630 nm and ESA over 630-1300 nm, with singlet exciton absorption (D_{EX}) centered at 1200 nm, polaron absorption (D_P) at 1000 nm and polaron pair absorption (D_{PP}) at around 670 nm. [32-33] The acceptor NIDCSEO3 film displays TA spectra composed of negative bands in the range of 450-600 nm and positive ESA bands in 600-1300 nm range. Negative bands in the visible region are well-matched with the steady-state absorption spectrum (Figure 3-2) and therefore are assigned to the GSB region. The main ESA band of NIDCSEO3 film is the singlet exciton absorption maximum at 930 nm, and there is also a weak absorption band at 740 nm, which is assigned to radical anion (polaron) absorption by the reduction in the spectro-electrochemistry measurement as shown in Figure 3-4. A weak absorption band at 610 nm is also shown in NIDCSEO3 TA spectra, probably due to the second transition of

acceptor radical anion, as demonstrated by the existence of the spectro-electrochemically measured absorption in the different reduction potentials. Due to the highly crystalline property and strongly π-π stacked structure of NIDCSEO3, radical anions are generated upon photoexcitation in the neat NIDCSEO3 film.

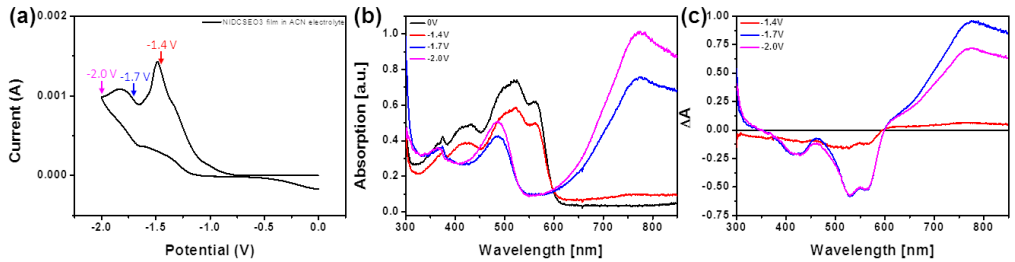

Figure 3-4 (a) Cyclic voltammogram of NIDCSEO3 film coated on ITO-coated glass in 0.1 M TBAHFP/acetonitrile electrolyte, (b) absorption and (c) absorbance difference spectra in the UV-vis range during the electrochemical reduction.

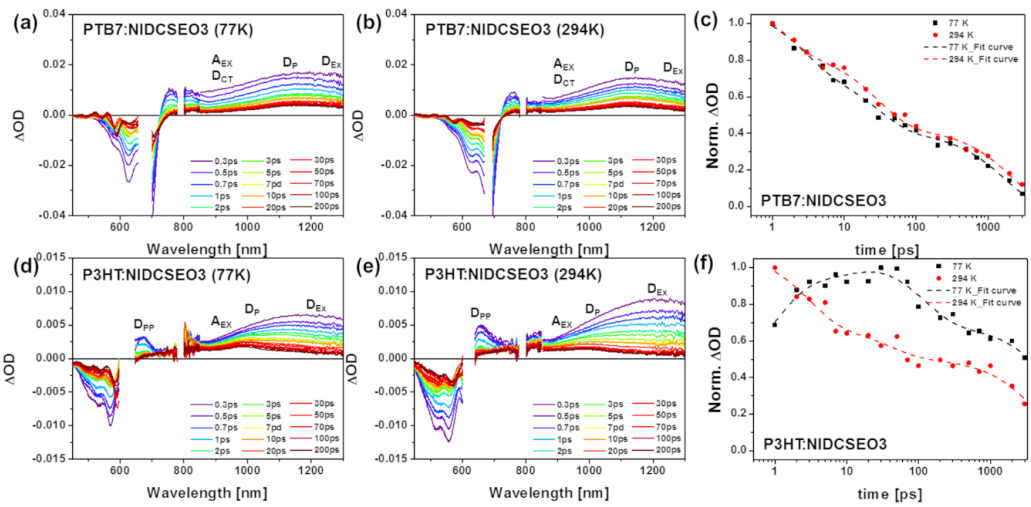

Figure 3-5 TA spectra of (a,b) PTB7:NIDCSEO3 at 77 K and 294 K (excited at 670 nm) and (d,e) P3HT:NIDCSEO3 at 77 K and 294 K (excited at 610 nm). Polaron decay profiles of (c) PTB7:NIDCSEO3 and (f) P3HT:NIDCSEO3 at 77 K and 294 K obtained by deconvolution of TA spectra at each delay time (D_{EX}, D_P, D_{CT}, D_{PP} and A_{EX} indicate the excited-state absorption of the donor exciton, donor polaron, donor ICT state, donor polaron pair state, and acceptor exciton, respectively).

By conducting transient absorption measurement of neat films, absorption spectra of each state in D and A materials were assigned, and the intrinsic electronic properties of PTB7 and P3HT were shown. To investigate whether the charge separation is following the hot or cold process in PSCs, we demonstrated the contribution of hot and relaxed CT states on charge separation at the D/A interface. The relaxed CT state is the bound state of charge carriers at the D/A interface with specific binding energy and thus can be separated into free charge carriers by the thermal activation after surviving geminate recombination. Therefore, to focus our discussion on the effect of hot and delocalized state on charge separation in BHJs, temperature-dependent TA measurements were conducted using PTB7:NIDCSEO3 and P3HT:NIDCSEO3 blend films at 77 K and 294 K. Figure 3-5 shows the TA spectra and donor polaron dynamics of PTB7:NIDCSEO3 and P3HT:NIDCSEO3 blend films upon selective photoexcitation of donor polymers at 670 nm and 610 nm, respectively. In the PTB7:NIDCSEO3 film, there is no significant difference in TA spectra at both 77 K and 294 K measurements. To clarify the temperature dependence on charge separation in PTB7:NIDCSEO3, it is required to extract the polaron absorption and decay dynamics from the overlapped ESA bands. Polaron decay dynamics were obtained by deconvolution of the TA spectra at each delay time based on the assignment of each state absorption at D and A neat films. The donor polaron decay profiles probed at 1150 nm (D_p in Figure 3-5a,b) are noticeably temperature-independent between 77 K and 294 K and exhibit no rise dynamics in PTB7:NIDCSEO3 blend, indicating that charge separation through the CT state is a

temperature-independent process and occurs within the ultrafast time scale. That is, the exciton dissociation via hot CT state is the dominant process in charge separation mechanism and polaron generation through the relaxed CT state is not significant in PTB7:NIDCSEO3.

However, P3HT:NIDCSEO3 shows a distinct trend of temperature dependence on charge separation. It is interesting to note that the rise-decay profile of P3HT polaron is clearly different between 77 K and 294 K. Polaron decay profiles of P3HT:NIDCSEO3 are obtained by deconvolution of TA spectra, as shown in Figure 3-5f. When probed at 1000 nm (D_p in Figure 3-5d,e), only ultrafast charge generation is shown at 294 K, whereas both ultrafast and delayed charge generation are shown at 77 K. The delayed charge generation is attributed to the charge generation through the relaxed state. Due to the Coulomb energy barrier, the charge generation through the relaxed state is much slower with the lifetime of 1 ps and 13 ps compared to the hot exciton dissociation. Interestingly, with the photoexcitation at 610 nm, delocalized P3HT excitons relax to the polaron pair state, as evidenced by the P3HT polaron pair absorption (D_{PP}) at 670 nm. Therefore, the delayed charge generation is based not only on the relaxed CT state but also on the P3HT polaron pair state. Previous papers reported that the lifetime of P3HT polaron pair dissociation is about 1 ps, which is consistent with our results in the decay of the P3HT polaron pair (Figure 3-6). [21,34] Therefore, the relaxed CT state dissociation is much slower with the lifetime of 13 ps at 77 K. That is, through the temperature dependence measurements, it is demonstrated that the charge separation

mechanisms of PTB7:NIDCSEO3 and P3HT:NIDCSEO3 are different, where PTB7:NIDCSEO3 exhibits a simple system with the hot exciton dissociation dominant charge generation, while P3HT:NIDCSEO3 shows the complex charge generation behavior with the combination of hot and relaxed CT states and P3HT polaron pair dissociation.

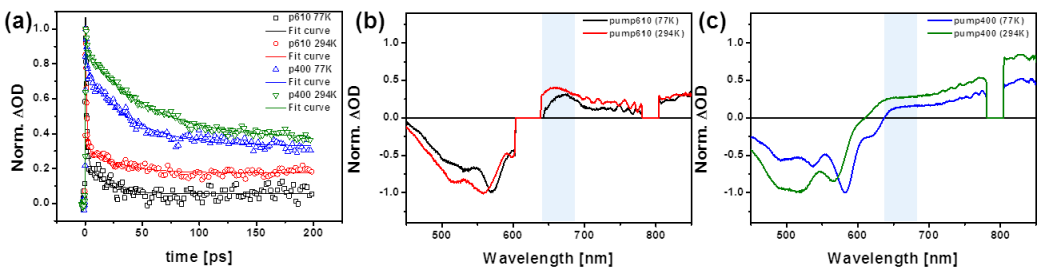

Figure 3-6 (a) Decay profiles of P3HT polaron pair absorption in P3HT:NIDCSEO3 blend films with different pump beams and temperatures within 200 ps and (b,c) transient absorption spectra at 0.3 ps in P3HT:NIDCSEO3 blend pumped at 610 nm and 400 nm (blue region is P3HT polaron pair absorption band).

PTB7, which has the copolymer structure of push-pull building blocks, exhibits initially photoexcited exciton with ICT characteristics by the spatial displacement of electron density. [20,35] With the excess energy, the delocalized exciton wave function is generated with still displaced electron and hole density, weakening the binding energy and facilitating the charge separation at the D/A interface. Consequently, efficient charge separation occurs via hot CT state at the D/A interface in PTB7:NIDCSEO3 blend with the aid of polarized and delocalized hot exciton, as demonstrated by the temperature-

independent ultrafast polaron generation. On the other hand, the temperature-dependent polaron generation of P3HT:NIDCSEO3 clearly shows a thermally assisted charge separation process. P3HT exhibits negligible ICT character of exciton and weakly bound inter-chain polaron pairs, already noted in several papers. [36-37] Due to the ultrafast polaron pair formation and relaxation of delocalized state of P3HT, although there is the contribution of ultrafast charge separation through the hot state on the charge separation, the excitons are mainly relaxed to the polaron pair within the polymer and localized CT state at D/A interface, and then separate into charge carriers through the temperature-assisted process. That is, the charge generation process in P3HT:NIDCSEO3 is a system combined with hot and relaxed states (interfacial CT state and polaron pair state) dissociation.

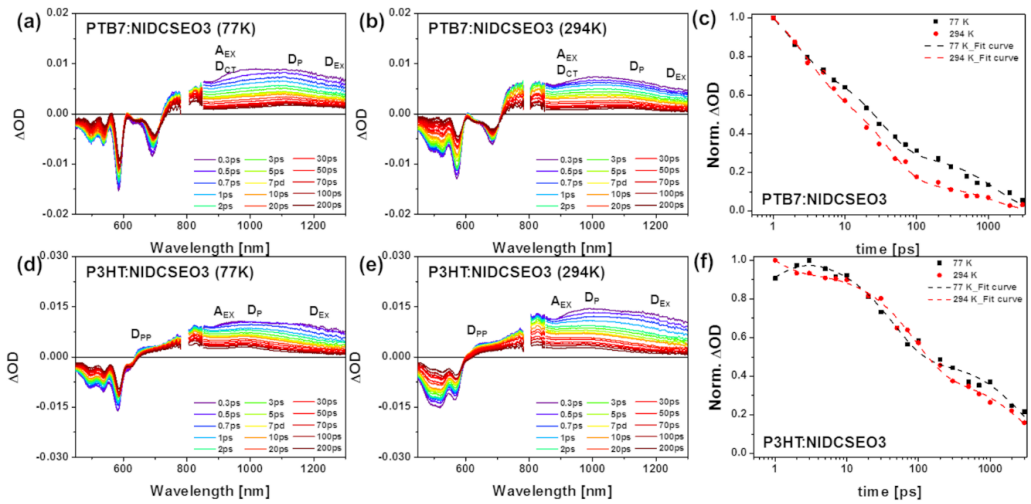

Figure 3-7 TA spectra of (a,b) PTB7:NIDCSEO3 at 77 K and 294 K (excited at 400 nm) and (d,e) P3HT:NIDCSEO3 at 77 K and 294 K (excited at 400 nm). Polaron decay profiles of (c) PTB7:NIDCSEO3 and (f) P3HT:NIDCSEO3 at 77 K and 294 K obtained by deconvolution of TA spectra at each delay time.

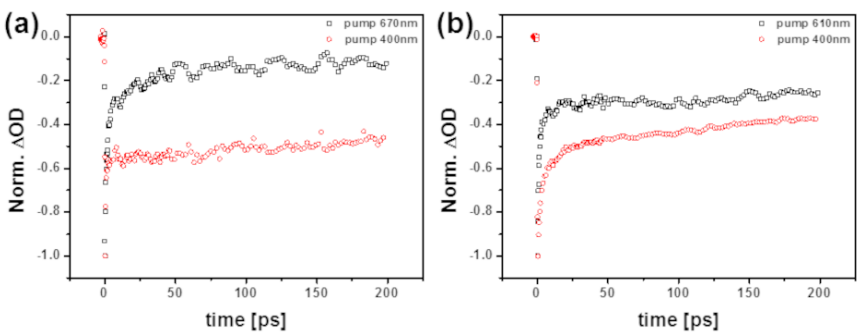

Figure 3-8 Decay profiles of GSB in (a) PTB7:NIDCSEO3 blend probed at 660 nm and (b) P3HT:NIDCSEO3 blend probed at 560 nm measured at 294 K.

Table 3-1 Exponential fitting parameters for the donor polaron dynamics corresponding to Figure 3 (c,f) obtained by deconvolution method (pumped by low excitation energy, 670 nm for PTB7:NIDCSEO3 and 610 nm for P3HT:NIDCSEO3).

	PTB7:NIDCSEO3		**P3HT:NIDCSEO3**	
	77 K	**294 K**	**77 K**	**294 K**
τ_1 [ps]	2.5 (32%)	1.2 (31%)	1 (-31%)	2.9 (38%)
τ_2 [ps]	29 (31%)	30 (34%)	13 (-10%)	39 (16%)
τ_3 [ps]	1720 (37%)	2190 (35%)	117 (21%)	> 3000 (46%)
τ_4 [ps]			> 3000 (38%)	

Table 3-2 Exponential fitting parameters for the donor polaron dynamics corresponding to Figure 4 (c,f) obtained by deconvolution method (pumped by high excitation energy, 400 nm for PTB7:NIDCSEO3 and P3HT:NIDCSEO3).

	PTB7:NIDCSEO3		**P3HT:NIDCSEO3**	
	77 K	**294 K**	**77 K**	**294 K**
τ_1 [ps]	1.6 (37%)	2.5 (42%)	0.9 (-22%)	0.7 (22%)
τ_2 [ps]	31 (39%)	38 (45%)	44 (41%)	89 (45%)
τ_3 [ps]	1340 (24%)	1200 (12%)	> 3000 (37%)	> 3000 (33%)

For further investigation on the effect of excitation energy on the charge generation, we also conducted the pump-dependent TA measurements with the photoexcitation at higher excited states using a 400 nm pump beam. By differing the excitation energy, the clear difference is shown at GSB recovery dynamics, which is known to correlate with the repopulation of the ground state. [38-39] In PTB7:NIDCSEO3, GSB region is shown at 450-750 nm range, and as depicted in GSB dynamics (Figure 3-8), GSB recovery is much slower when excited at higher energy states (pumped by 400 nm) than at lower energy states (pumped by 670 nm), because of the lack of the excited state population going back to the ground state. Therefore, slower GSB recovery indicates more efficient charge separation at higher excited states. Furthermore, the slower GSB recovery is consistent with the increased polaron absorption (D_P in Figure 3-7a,b) at the 1150 nm. By comparing the TA spectra at 0.3 ps (Figure 3-9), the polaron absorption intensity clearly increases compared to the singlet exciton absorption when excited by higher excitation energy, also supporting the efficient charge generation. Temperature-independent polaron decay feature (Figure 3-7c) supports this ultrafast and efficient charge generation at higher excited states is hot exciton dissociation dominant charge generation process.

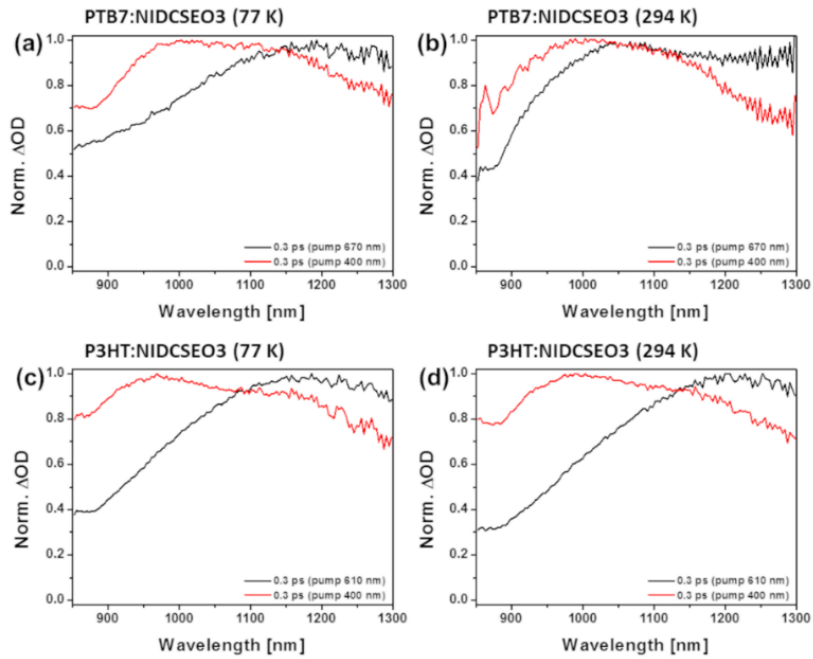

Figure 3-9 Femtosecond TA spectra at 0.3 ps of (a,b) PTB7:NIDCSEO3 and (c,d) P3HT:NIDCSEO3 blends.

In P3HT:NIDCSEO3, it is noteworthy that there are significant differences in TA spectra and the excited state dynamics depending on the excitation energy. The slower GSB recovery (450-600 nm) is also shown in P3HT:NIDCSEO3 when excited by higher energy (Figure 3-8), indicating incomplete recombination of excitons and more efficient charge generation at higher excited states. In addition, donor polaron (D_P) and polaron pair (D_{PP}) absorption features are significantly dependent on the excitation energy. Comparing the TA spectra at 0.3 ps (Figure 3-9), donor polaron absorption at 1000 nm is significantly enhanced with higher excitation energy, implying efficient charge generation at the D/A interface. Moreover, much smaller polaron pair absorption at 670 nm is displayed when excited with 400 nm pump beam (Figure 3-7d,e), indicative of less amount of relaxation of hot P3HT exciton to inter-chain polaron pair state, and thus enhanced hot charge separation at D/A interface. This change in TA spectra depending on the excitation energy is consistent with the polaron generation dynamics. Temperature dependence of polaron generation dynamics is also shown at higher excited states, however, the contributions of hot and relaxed charge separation processes are different. The lifetime of delayed charge generation is about 0.9 ps, which is consistent with the charge generation lifetime through the polaron pair state, and the P3HT polaron pair generation yield decreases at higher excited states (Figure 3-6), resulting in a smaller contribution on charge generation. Thus, the smaller contribution of delayed charge generation indicates that a larger amount of charge generation is through the hot CT state under high excitation energy. Namely, charge generation in P3HT:NIDCSEO3 excited

at higher electronic states is also the combination of the hot CT state at D/A interface and relaxed polaron pair state dissociation, where the contribution of ultrafast charge generation through the hot CT state is greatly increased with more delocalized exciton state.

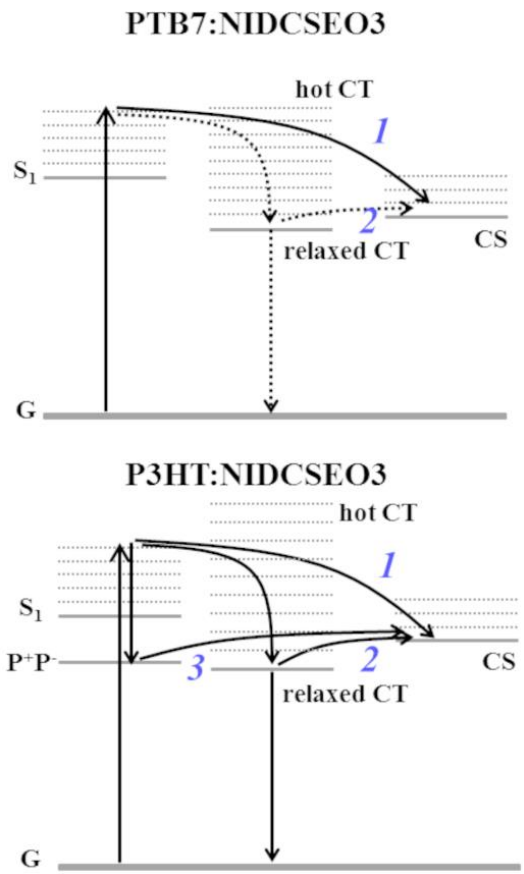

Figure 3-10 Schematic energy level diagram of charge separation dynamics in PTB7:NIDCSEO3 and P3HT:NIDCSEO3.

Consequently, through the temperature- and pump-dependent TA results, we explored the importance of excitonic characteristics of polymer and hot and delocalized state for charge separation at the D/A interface. The schematic energy diagram illustrating the charge separation in PTB7:NIDCSEO3 and P3HT:NIDCSEO3 is depicted in Figure 3-10. PTB7:NIDCSEO3 exhibits hot exciton dissociation dominant ultrafast charge generation due to the delocalized excitons with ICT characteristics with the aid of excess energy. On the other hand, P3HT:NIDCSEO3 exhibits a system combined with hot and relaxed charge generation due to the ultrafast relaxation of primary excited delocalized exciton state to polaron pair state. The portion of this cold process decreases with the photoexcitation of higher states because of the much more delocalized exciton wave function and weaker binding between charge carriers at the D/A interface of P3HT:NIDCSEO3, resulting in more efficient charge generation at the higher excited states.

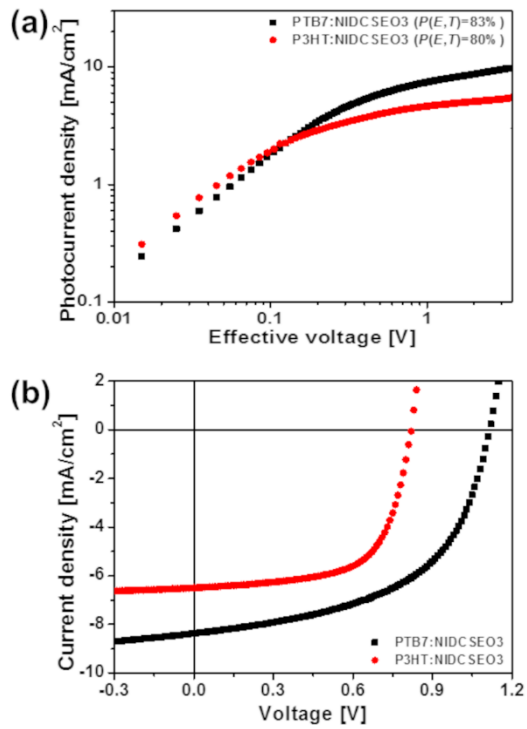

Figure 3-11 (a) Photocurrent density–effective voltage (J_{ph}–V_{eff}) characteristics and (b) the current density–voltage (J–V) curves for PTB7:NIDCSEO3 [25] and P3HT:NIDCSEO3 PSCs.

Table 3-3 Photovoltaic properties of PTB7:NIDCSEO3 and P3HT:NIDCSEO3 PSCs. [25]

	V_{OC} [V]	J_{SC} [mA/cm^2]	FF	PCE [%]
PTB7:NIDCSEO3	1.12	8.37	0.53	4.99
P3HT:NIDCSEO3	0.82	6.50	0.64	3.41

To understand the effect of different charge generation mechanisms on the device performance in more detail, the dependence of photocurrent density (J_{ph}) on effective voltage (V_{eff}) was analyzed for PTB7:NIDCSEO3 and P3HT:NIDCSEO3 PSCs. Figure 3-11a presents the J_{ph} versus V_{eff} curves for both PSCs. J_{ph} is defined as $J_{ph} = J_L - J_D$, where J_L and J_D are the current densities in illumination and darkness conditions, respectively, and V_{eff} is defined as $V_{eff} = V_0 - V_a$, where V_0 is the voltage at which J_{ph} is equal to zero and Va is the applied bias voltage. The exciton dissociation probability ($P(E,T)$) is determined by normalizing J_{ph} with J_{sat}, implying the fraction of the photogenerated excitons dissociate into the charge carriers collecting at the electrode. [40-42] The values of $P(E,T)$ for PTB7:NIDCSEO3 and P3HT:NIDCSEO3 PSCs are 83% and 80%, respectively, indicating the geminate recombination loss is relatively larger in P3HT:NIDCSEO3 PSC, and charge separation and collection to the electrode is efficient in PTB7:NIDCSEO3 PSC. Based on the Onsager-Braun model, relaxed CT states undergo the charge separation competing with the geminate recombination to the ground state. [7,33] Therefore, the charge separation via relaxed CT state at D/A interface in P3HT:NIDCSEO3 can raise the possibility for the geminate recombination, which is detrimental for the photocurrent in PSCs. This assumption is supported by the lower exciton dissociation efficiency in P3HT:NIDCSEO3 PSC. Consequently, through the exciton dissociation probability value and temperature- and pump-dependent TA analysis results, PTB7:NIDCSEO3 system exhibits efficient exciton dissociation through hot CT state because of the exciton with ICT characteristics with delocalized

wave functions, leading to the higher device performance than P3HT:NIDCSEO3 blend system.

As demonstrated by the efficient charge generation via hot CT state from fs-TA measurements and higher exciton dissociation efficiency from the photovoltaic device, efficient charge generation and suppressed geminate recombination are shown in PTB7:NIDCSEO3 compared to P3HT:NIDCSEO3 system. Efficient charge generation and collection with the broader light absorbing property of PTB7:NIDCSEO3 greatly affect the photocurrent in photovoltaic devices, leading to a higher J_{SC} than that of P3HT:NIDCSEO3 PSC. Furthermore, the deeper HOMO level of PTB7 leads to the higher open-circuit voltage (V_{OC}) in the PTB7:NIDCSEO3 PSC compared to P3HT:NIDCSEO3 PSC. Consequently, with the superior light absorbing and charge generation properties and deeper HOMO level, PTB7:NIDCSEO3 PSC exhibits a higher power conversion efficiency (PCE) value of 4.99% than P3HT:NIDCSEO3 with a PCE of 3.41%.

3.4. Conclusions

A comprehensive study through the temperature- and pump-dependent TA spectroscopy was conducted to unravel the charge separation mechanism in PSCs with different ICT characteristics of polymer exciton by comparing push-pull type copolymer

PTB7 and crystalline homopolymer P3HT. By using the highly crystalline NIDCSEO3 acceptor, both blend systems exhibit the strongly π-π stacked blend morphology, beneficial for efficient exciton delocalization. In PTB7:NIDCSEO3, initially generated exciton with ICT characteristics facilitates spatial separation of electron density. With the excess energy, ultrafast charge separation via hot CT state occurs at the D/A interface with the aid of polarized and delocalized PTB7 exciton, demonstrated by temperature-independent polaron generation dynamics. On the other hand, P3HT:NIDCSEO3 exhibits a complex charge separation mechanism with the hot and relaxed CT states and polaron pair dissociation despite the delocalized wave function of P3HT, supported by strongly temperature-dependent polaron generation. The cold charge separation in P3HT:NIDCSEO3 is because of the ultrafast polaron pair formation and relaxation of delocalized P3HT exciton. In this research, we could show that the separation of electron and hole in push-pull type materials does not contradict the wave function delocalization, and not only the delocalized state but also the displacement of delocalized charge carriers is important for the charge separation via hot CT state and suppressed geminate recombination in PSCs. Therefore, we believe our findings can provide the importance of the excess energy in the charge generation in BHJs and furthermore suggest valuable information for the donor polymer design for high performance PSCs.

3.5. References

[1] Clarke, T. M.; Durrant, J. R., Charge Photogeneration in Organic Solar Cells. *Chem. Rev*. **2010**, *110*, 6736-6767.

[2] Athanasopoulos, S.; Bässler, H.; Köhler, A., Disorder vs Delocalization: Which Is More Advantageous for High-Efficiency Organic Solar Cells? *J. Phys. Chem. Lett.* **2019**, *10*, 7107-7112.

[3] Bässler, H.; Köhler, A., "Hot or Cold": How Do Charge Transfer States at the Donor–Acceptor Interface of an Organic Solar Cell Dissociate? *Phys. Chem. Chem. Phys*. **2015**, *17*, 28451-28462.

[4] Park, K. H.; Son, S. Y.; Kim, J. O.; Kang, G.; Park, T.; Kim, D., Role of Disorder in the Extent of Interchain Delocalization and Polaron Generation in Polythiophene Crystalline Domains. *J. Phys. Chem. Lett*. **2018**, *9*, 3173-3180.

[5] Pensack, R. D.; Guo, C.; Vakhshouri, K.; Gomez, E. D.; Asbury, J. B., Influence of Acceptor Structure on Barriers to Charge Separation in Organic Photovoltaic Materials. *J. Phys. Chem. C* **2012**, *116*, 4824-4831.

[6] Boschetto, G.; Krompiec, M.; Skylaris, C.-K., Insights into the Charge-Transfer Mechanism of Organic Photovoltaics: Effect of Domain Size. *J. Phys. Chem. C* **2018**, *122*, 17024-17034.

[7] Jakowetz, A. C.; Böhm, M. L.; Zhang, J.; Sadhanala, A.; Huettner, S.; Bakulin, A. A.;

Rao, A.; Friend, R. H., What Controls the Rate of Ultrafast Charge Transfer and Charge Separation Efficiency in Organic Photovoltaic Blends. *J. Am. Chem. Soc*. **2016**, *138*, 11672-11679.

[8] Chen, K.; Barker, A. J.; Reish, M. E.; Gordon, K. C.; Hodgkiss, J. M., Broadband Ultrafast Photoluminescence Spectroscopy Resolves Charge Photogeneration via Delocalized Hot Excitons in Polymer:Fullerene Photovoltaic Blends. *J. Am. Chem. Soc*. **2013**, *135*, 18502-18512.

[9] Grancini, G.; Maiuri, M.; Fazzi, D.; Petrozza, A.; Egelhaaf, H. J.; Brida, D.; Cerullo, G.; Lanzani, G., Hot Exciton Dissociation in Polymer Solar Cells. *Nat. Mater*. **2013**, *12*, 29-33.

[10] Muraoka, A.; Fujii, M.; Mishima, K.; Matsunaga, H.; Benten, H.; Ohkita, H.; Ito, S.; Yamashita, K., Investigations on the Charge Transfer Mechanism at Donor/Acceptor Interfaces in the Quest for Descriptors of Organic Solar Cell Performance. *Phys. Chem. Chem. Phys*. **2018**, *20*, 12193-12199.

[11] Grancini, G.; Martino, N.; Antognazza, M. R.; Celebrano, M.; Egelhaaf, H.-J.; Lanzani, G., Influence of Blend Composition on Ultrafast Charge Generation and Recombination Dynamics in Low Band Gap Polymer-Based Organic Photovoltaics. *J. Phys. Chem. C* **2012**, *116*, 9838-9844.

[12] Bakulin, A. A.; Rao, A.; Pavelyev, V. G.; van Loosdrecht, P. H. M.; Pshenichnikov, M. S.; Niedzialek, D.; Cornil, J.; Beljonne, D.; Friend, R. H., The Role of Driving Energy and Delocalized States for Charge Separation in Organic Semiconductors. *Science* **2012**,

335, 1340-1344.

[13] Tamai, Y.; Fan, Y.; Kim, V. O.; Ziabrev, K.; Rao, A.; Barlow, S.; Marder, S. R.; Friend, R. H.; Menke, S. M., Ultrafast Long-Range Charge Separation in Nonfullerene Organic Solar Cells. *ACS Nano* **2017**, *11*, 12473-12481.

[14] Dimitrov, S. D.; Azzouzi, M.; Wu, J.; Yao, J.; Dong, Y.; Shakya Tuladhar, P.; Schroeder, B. C.; Bittner, E. R.; McCulloch, I.; Nelson, J. et al. Spectroscopic Investigation of the Effect of Microstructure and Energetic Offset on the Nature of Interfacial Charge Transfer States in Polymer: Fullerene Blends. *J. Am. Chem. Soc*. **2019**, *141*, 4634-4643.

[15] Albrecht, S.; Vandewal, K.; Tumbleston, J. R.; Fischer, F. S. U.; Douglas, J. D.; Fréchet, J. M. J.; Ludwigs, S.; Ade, H.; Salleo, A.; Neher, D., On the Efficiency of Charge Transfer State Splitting in Polymer:Fullerene Solar Cells. *Adv. Mater*. **2014**, *26*, 2533-2539.

[16] Vandewal, K.; Albrecht, S.; Hoke, E. T.; Graham, K. R.; Widmer, J.; Douglas, J. D.; Schubert, M.; Mateker, W. R.; Bloking, J. T.; Burkhard, G. F. et al. Efficient Charge Generation by Relaxed Charge-Transfer States at Organic Interfaces. *Nat. Mater*. **2014**, *13*, 63-68.

[17] Lee, J.; Vandewal, K.; Yost, S. R.; Bahlke, M. E.; Goris, L.; Baldo, M. A.; Manca, J. V.; Van Voorhis, T., Charge Transfer State Versus Hot Exciton Dissociation in Polymer−Fullerene Blended Solar Cells. *J. Am. Chem. Soc*. **2010**, *132*, 11878-11880.

[18] van der Hofstad, T. G. J.; Di Nuzzo, D.; van den Berg, M.; Janssen, R. A. J.; Meskers, S. C. J., Influence of Photon Excess Energy on Charge Carrier Dynamics in a Polymer-Fullerene Solar Cell. *Adv. Energy Mater*. **2012**, *2*, 1095-1099.

[19] Rolczynski, B. S.; Szarko, J. M.; Son, H. J.; Liang, Y.; Yu, L.; Chen, L. X., Ultrafast Intramolecular Exciton Splitting Dynamics in Isolated Low-Band-Gap Polymers and Their Implications in Photovoltaic Materials Design. *J. Am. Chem. Soc*. **2012**, *134*, 4142-4152.

[20] Szarko, J. M.; Rolczynski, B. S.; Lou, S. J.; Xu, T.; Strzalka, J.; Marks, T. J.; Yu, L.; Chen, L. X., Photovoltaic Function and Exciton/Charge Transfer Dynamics in a Highly Efficient Semiconducting Copolymer. *Adv. Funct. Mater*. **2014**, *24*, 10-26.

[21] Rana, D.; Donfack, P.; Jovanov, V.; Wagner, V.; Materny, A., Ultrafast Polaron-Pair Dynamics in a Poly(3-hexylthiophene-2,5-diyl) Device Influenced by a Static Electric Field: Insights into Electric-Field-Related Charge Loss. *Phys. Chem. Chem. Phys*. **2019**, *21*, 21236-21248.

[22] Kwon, O. K.; Park, J.-H.; Park, S. K.; Park, S. Y., Soluble Dicyanodistyrylbenzene-Based Non-Fullerene Electron Acceptors with Optimized Aggregation Behavior for High-Efficiency Organic Solar Cells. *Adv. Energy Mater*. **2015**, *5*, 1400929.

[23] Park, J.-H.; Kim, J.; Kim, J. H.; Kim, D. W.; Ryoo, C. H.; Kwon, O. K.; Lee, C.; Kwon, J. E.; Park, S. Y., Effect of Alkyl Chain Lengths of Highly Crystalline Nonfullerene Acceptors on Open-Circuit Voltage of All-Small-Molecule Organic Solar Cells. *ACS Appl. Energy Mater*. **2021**, *4*, 259-267.

[24] Kwon, O. K.; Uddin, M. A.; Park, J.-H.; Park, S. K.; Nguyen, T. L.; Woo, H. Y.; Park, S. Y., A High Efficiency Nonfullerene Organic Solar Cell with Optimized Crystalline Organizations. *Adv. Mater*. **2016**, *28*, 910-916.

[25] Cui, J.; Park, J.-H.; Kim, D. W.; Choi, M.-W.; Chung, H. Y.; Kwon, O. K.; Kwon, J. E.; Park, S. Y., Designing Nonfullerene Acceptors with Oligo(ethylene glycol) Side Chains: Unraveling the Origin of Increased Open-Circuit Voltage and Balanced Charge Carrier Mobilities (in press), *Chem. Asian J.* **2021,** https://doi.org/10.1002/asia.202100660.

[26] Nan, G.; Zhang, X.; Lu, G., Do "Hot" Charge-Transfer Excitons Promote Free Carrier Generation in Organic Photovoltaics? *J. Phys. Chem. C* **2015**, *119*, 15028-15035.

[27] Tamura, H.; Burghardt, I., Ultrafast Charge Separation in Organic Photovoltaics Enhanced by Charge Delocalization and Vibronically Hot Exciton Dissociation. *J. Am. Chem. Soc*. **2013**, *135*, 16364-16367.

[28] Liu, X.; Xie, B.; Duan, C.; Wang, Z.; Fan, B.; Zhang, K.; Lin, B.; Colberts, F. J. M.; Ma, W.; Janssen, R. A. J. et al. A High Dielectric Constant Non-Fullerene Acceptor for Efficient Bulk-Heterojunction Organic Solar Cells. *J. Mater. Chem. A* **2018**, *6*, 395-403.

[29] Meng, B.; Song, H.; Chen, X.; Xie, Z.; Liu, J.; Wang, L., Replacing Alkyl with Oligo(ethylene glycol) as Side Chains of Conjugated Polymers for Close π–π Stacking. *Macromolecules* **2015**, *48*, 4357-4363.

[30] He, X.; Zhu, G.; Yang, J.; Chang, H.; Meng, Q.; Zhao, H.; Zhou, X.; Yue, S.; Wang, Z.; Shi, J. et al. Photogenerated Intrinsic Free Carriers in Small-Molecule Organic

Semiconductors Visualized by Ultrafast Spectroscopy. *Sci. Rep*. **2015**, *5*, 17076.

[31] Matheson, A. B.; Ruseckas, A.; Pearson, S. J.; Samuel, I. D. W., Hole Delocalization as a Driving Force for Charge Pair Dissociation in Organic Photovoltaics. *Mater. Horiz.* **2019**, *6*, 1050-1056.

[32] Guo, J.; Ohkita, H.; Benten, H.; Ito, S., Charge Generation and Recombination Dynamics in Poly(3-hexylthiophene)/Fullerene Blend Films with Different Regioregularities and Morphologies. *J. Am. Chem. Soc*. **2010**, *132*, 6154-6164.

[33] Howard, I. A.; Mauer, R.; Meister, M.; Laquai, F., Effect of Morphology on Ultrafast Free Carrier Generation in Polythiophene:Fullerene Organic Solar Cells. *J. Am. Chem. Soc*. **2010**, *132*, 14866-14876.

[34] Ogata, Y.; Kawaguchi, D.; Tanaka, K., An Effect of Molecular Motion on Carrier Formation in a Poly(3-hexylthiophene) Film. *Sci. Rep*. **2015**, *5*, 8436.

[35] Carsten, B.; Szarko, J. M.; Son, H. J.; Wang, W.; Lu, L.; He, F.; Rolczynski, B. S.; Lou, S. J.; Chen, L. X.; Yu, L., Examining the Effect of the Dipole Moment on Charge Separation in Donor-Acceptor Polymers for Organic Photovoltaic Applications. *J. Am. Chem. Soc*. **2011**, *133*, 20468-20475.

[36] Cho, S.; Rolczynski, B. S.; Xu, T.; Yu, L.; Chen, L. X., Solution Phase Exciton Diffusion Dynamics of a Charge-Transfer Copolymer PTB7 and a Homopolymer P3HT. *J. Phys. Chem. B* **2015**, *119*, 7447-7456.

[37] Tautz, R.; Da Como, E.; Limmer, T.; Feldmann, J.; Egelhaaf, H.-J.; von Hauff, E.; Lemaur, V.; Beljonne, D.; Yilmaz, S.; Dumsch, I. et al. Structural Correlations in the

Generation of Polaron Pairs in Low-Bandgap Polymers for Photovoltaics. *Nat. Commun.* **2012**, *3*, 970.

[38] Dimitriev, O. P.; Blank, D. A.; Ganser, C.; Teichert, C., Effect of the Polymer Chain Arrangement on Exciton and Polaron Dynamics in P3HT and P3HT:PCBM Films. *J. Phys. Chem. C* **2018**, *122*, 17096-17109.

[39] Alsulami, Q. A.; Murali, B.; Alsinan, Y.; Parida, M. R.; Aly, S. M.; Mohammed, O. F., Remarkably High Conversion Efficiency of Inverted Bulk Heterojunction Solar Cells: From Ultrafast Laser Spectroscopy and Electron Microscopy to Device Fabrication and Optimization. *Adv. Energy Mater.* **2016**, *6*, 1502356.

[40] Lee, H.; Oh, S.; Song, C. E.; Lee, H. K.; Lee, S. K.; Shin, W. S.; So, W.-W.; Moon, S.-J.; Lee, J.-C., Stable P3HT: Amorphous Non-Fullerene Solar Cells with a High Open-Circuit Voltage of 1 V and Efficiency of 4%. *RSC Adv*. **2019**, *9*, 20733-20741.

[41] Lee, J. W.; Bae, S.; Jo, W. H., Synthesis of 6H-Benzo[c]chromene as a New Electron-Rich Building Block of Conjugated Alternating Copolymers and its Application to Polymer Solar Cells. *J. Mater. Chem. A* **2014**, *2*, 14146-14153.

[42] Hwang, H.; Sin, D. H.; Park, C.; Cho, K., Ternary Organic Solar Cells Based on a Wide-Bandgap Polymer with Enhanced Power Conversion Efficiencies. *Sci. Rep*. **2019**, *9*, 12081.

Chapter 4.

Femtosecond Transient Absorption Studies of Polymer Aggregation on Photovoltaic Performance: Role of an Integrated Aggregation Promotor in the Polymer Chain

4.1. Introduction

Polymer solar cells (PSCs) have been extensively investigated as a competitive technology for renewable energy due to their advantages of light weight, low cost of fabrication, and capability of flexible devices with large area and roll-to-roll method fabrication. [1-2] Based on these advantages of PSCs, power conversion efficiencies (PCEs) of over 17% have been achieved. [3-5] In decades, considerable attention has been paid to the fullerene derivatives in the early development stage of PSCs with their distinct advantages such as an isotropic electron transport in three dimension, high electron mobility, and multiple reversible electrochemical reductions. [6-7] However, fullerene derivatives also have inherent drawbacks of weak absorption in the region of the solar spectrum and restricted energy level tunability, which definitely limit the photocurrent in PSCs. [8-9] Recently, enormous progress has been reported for nonfullerene acceptor (NFA) PSCs with great advantages such as tunable energy levels

and strong absorption in the near-IR region, which are beneficial to cover the broad absorption range of PSCs by sharing with those of donor materials. [10-15] With the development of NFAs, the structure of donor polymers matching well with both fullerene and NFAs is much more important. [16-20] For the ideal donor:acceptor (D:A) blend morphology, too small domain or oversized phase segregation should be avoided for the efficient exciton dissociation, charge separation and transport in PSCs. [21-24] In order to obtain a morphology with an appropriate domain size, several strategies of material design have been studied on the donor characteristics by modifying the polymer backbone curvature, solution aggregation, and surface energy matching with the acceptor. [25-28] However, despite the importance of the donor polymer design and D:A blend morphology, their effects on the excited state dynamics and charge carrier generation have barely been investigated in the viewpoint of the professional photophysical study. Therefore, correlating the charge generation and recombination processes monitored by the time-resolved spectroscopic studies with those by the PSC device characteristics in terms of the blend morphology is greatly important to obtain high performance bulkheterojunction (BHJ) PSCs.

Nowadays, efficient strategies focusing on the appropriate blend morphology of PSCs are based on the polymer aggregation in fullerene and NFA PSCs. Polymer aggregation is the key factor to form an interpenetrating network of hole- and electron-transporting pathways with electron donating and electron accepting semiconducting materials, respectively. [29-30] For instance, famous donor polymers such as PBDB-T

and PffBT4T-2OD have attracted significant attention in terms of the polymer aggregation with several methods to control the aggregation and D:A blend morphology such as modifying molecular designs with changing backbone structures or side chains, and use of comonomers. [29,31-36] In particular, the polymer backbone curvature has a great influence on the polymer solubility, miscibility with the acceptor, and thus the domain purity and the D:A blend morphology, consequently. [37-42] Most importantly, the aggregate formation property is greatly affected by the polymer backbone structure, resulting in dramatic changes in the charge carrier mobility and photovoltaic properties. However, complication arises since acceptor interdigitation between donor polymers and D:A blend morphology are controlled by the polymer backbone curvature and planarity. [38-39, 43] Furthermore, another important factor influencing the blend morphology is the acceptor structure. Fullerene and NFA materials have different aggregation and percolation properties due to their distinct structures, resulting in different blend morphologies depending on the polymer property. Therefore, controlling polymer aggregation while keeping the same polymer backbone structure is an ideal way for the spectroscopic study of the BHJ with a given acceptor that focuses on the aggregation effect in general, which is targeted in this work and has been elusive so far. [43-44] Accordingly, we investigated the two donor – two acceptor pairing system possessing extremely different D:A blend morphologies through femtosecond transient absorption studies.

In this report, we sought to resolve how the charge carrier dynamics are different for

the pure domain system and intermixed system with respect to the charge generation and recombination. We intentionally induced a very small difference with the aggregation promotor (β-cyano groups) on the donor polymer backbones to compare the polymer aggregation property and their effect on the photovoltaic properties in the D:A blend films. In a previous study, β-DCS type polymer PBDCS exhibited a rigid and planar backbone and strong temperature-dependent aggregation properties due to the resonance structure induced by two cyano groups, resulting in the high photovoltaic performances in both fullerene and NFA PSCs. [45] When using PBDS possessing almost the same backbone structure as that of PBDCS except for the aggregation promotor as a control donor, aggregation properties were shown to be significantly different from those of the PBDCS blend systems. PBDCS and PBDS were used as donor polymers for the systematic study of the effect of polymer aggregation. A fullerene acceptor, [6,6]-phenyl-C_{71}-butyric acid methyl ester ($PC_{71}BM$), and NFA, 3,9-bis(2-methylene-(3-(1,1-dicyanomethylene)-indanone))-5,5,11,11-tetrakis(4-hexylphenyl)-dithieno[2,3-d:2′,3′-d′]-s-indaceno[1,2-b:5,6-b′]dithiophene (ITIC), were used with different aggregation and percolation properties to explore the difference of the blend morphology and aggregation effect of donor polymers in the PSCs. [46-48] In this report, we explored the effect of donor polymer aggregation on fullerene and NFA blend morphology and, in addition, photovoltaic properties and excited state dynamics of PSCs. Through transient absorption spectroscopy, we could explore the domain size and purity of blend morphologies of the two donor – two acceptor paring system from the exciton decay and

polaron generation dynamics. Furthermore, correlating the polaron lifetime in BHJ films and the light intensity-dependent charge recombination in the PSC device could provide important insights into polymer design rules for obtaining high-efficiency photovoltaic devices.

4.2. Experimental Section

4.2.1. Device fabrication and characterization

The fabrication of PBDCS:$PC_{71}BM$ and PBDCS:ITIC device cells was reported in previous paper. [45] The patterned indium tin oxide (ITO) glass substrates were cleaned in an ultrasonic bath with acetone and isopropanol, and then exposed to UV/O_3 for 20 min. PEDOT:PSS (Clavious P VP AI 4083) was spin-coated onto the ITO glass substrate at 5000 rpm for 30 s and the film was subsequently baked at 150 °C for 10 min. The PBDS:$PC_{71}BM$ (1:1.5 ratio) in chlorobenzene solution (totally 17.5 mg/mL concentration) or PBDS:ITIC (1:1 ratio) in chlorobenzene solution (totally 16 mg/mL concentration) was subsequently spin-coated (1500 rpm) on the PEDOT:PSS coated ITO glass to form an active layer (ca. 80 nm). After drying the resulting films in a N_2 glovebox at room temperature for 30 min., thermal annealing treatment was conducted at 100 °C for 10 min. Then, Ca (5nm) was thermally deposited on a photoactive layer under a

vacuum of 10^{-6} torr. Finally, Al (100 nm) was thermally deposited under a vacuum of 10^{-6} torr.

The current density–voltage (*J–V*) characteristics of the solar cells were measured using a Keithley 4200 source measurement unit. The solar cell performances were characterized under AM 1.5G conditions with an illumination intensity of 100 mW/cm^2, as generated using an Oriel Sol3A solar simulator (Oriel model 9023A). The measurements were carried out through a shadow mask with well-defined aperture area of 0.04 cm^2 under an ambient atmosphere.

Two-deminsional grazing incidence X-ray diffraction (2D-GIXD) measurements were performed at the 9A U-SAXS beam line (E = 11.08 keV) and 3C SAXS beam line (E = 10.00 keV) in the Pohang Accelerator Laboratory (PAL) in Korea.

4.2.2. Spectroscopic and electrochemical characterization

UV–vis absorption spectra were measured with a UV-1650 PC (Shimadzu) spectrometer. Photoluminescence emission spectra were measured using a Felix32 QM-40 (Photo Technology International) and a Cary Eclipse (Varian) fluorescence spectrophotometer; the emission spectra were corrected for the sensitivity of the photomultiplier. The cyclic voltammetry experiments were carried out using a 273A (Princeton Applied Research) with a three-electrode cell assembly including an ITO-

coated glass working electrode, a platinum wire counter electrode, and a quasi Ag^+/Ag electrode as a reference electrode. Measurements were performed in a 0.1 M acetonitrile solution with tetrabutylammonium hexafluorophosphate as the supporting electrolyte at a scan rate of 100 mV/s. The HOMO level was estimated based on the onset oxidation potential using ferrocene as a reference. The LUMO level was calculated from the band edge of the absorption spectra and the HOMO level from cyclovoltammetry measurements.

The femtosecond time-resolved transient absorption (fs-TA) spectrometer consisted of Optical Parametric Amplifiers (Palitra, Quantronix) pumped by a Ti:sapphire regenerative amplifier system (Integra-C, Quantronix) operating at a 1 kHz repetition rate and an optical detection system. The generated OPA pulses, which were used as pump pulses, had a pulse width of ~ 100 fs and an average power of 100 mW in the range 550-690 nm. White light continuum (WLC) probe pulses were generated using a sapphire window by focusing of a small portion of the fundamental 800 nm pulses which was picked off by a quartz plate before entering the OPA. The time delay between the pump and probe beams was carefully controlled by making the pump beam travel along a variable optical delay (ILS250, Newport). The intensities of the spectrally dispersed WLC probe pulses are monitored using a high Speed spectrometer (Ultrafast Systems). To obtain a time-resolved transient absorption difference signal at a specific time, the pump pulses were chopped at 500 Hz and absorption spectra intensities were saved alternately with or without a pump pulse. Typically, 6000 pulses excite samples to obtain

the fs-TA spectra at a particular delay time. The polarization angle between the pump and probe beam was set at the magic angle (54.7°) using a Glan-laser polarizer with a half-wave retarder in order to prevent polarization-dependent signals. Cross-correlation fwhm in pump-probe experiments was less than 200 fs and the chirp of WLC probe pulses was measured to be 800 fs in the 450-850 nm region. For anisotropy measurement, TA signals with the polarization of the pump and probe pulses being parallel and perpendicular were independently collected by controlling the polarization of the pump pulse with the half-wave plate and the wire-grid polarizer.

The sub-nanosecond time-resolved transient absorption spectrometer consists of Optical Parametric Amplifiers (Palitra, Quantronix) pumped by a Ti:sapphire regenerative amplifier system (Integra-C, Quantronix) operating at a 1 kHz repetition rate for excitation pulse, and a Ti:sapphire laser (Maitai BB, SpectraPhysics) which provides a repetition rate of 80 MHz with ~100 fs pulses and an optical detection system. The generated OPA pulses, which were used as pump pulses, had a pulse width of ~100 fs and an average power of 100 mW in the range 280–2700 nm. The 80 MHz pulse train in the range from 710–990 nm from the Ti:sapphire laser generates supercontinuum pulses, which were used as probe pulses, by photonic crystal fiber (FemtoWHITE 800, NKT Photonics). To obtain the transient absorption difference signal at a specific time, a randomly-interleaved-pulse-train method is used with photodiodes (FPD510-V, Menlosystems) and an oscilloscope.

4.2.3. Quantum chemical calculation

Theoretical molecular orbital calculation was carried out with the density functional theory (DFT) using the Gaussian09 program package at the B3LYP/6-311G(d,p) level to characterize optimized ground geometry and electron density of HOMO and LUMO states. In optimized ground-state geometry, the alkyl groups of the molecules were simplified to methyl groups to reduce to the cost of calculation.

4.3. Result and Discussion

Figure 4-1 shows the molecular structures of donor polymers (PBDCS, PBDS), and acceptors ($PC_{71}BM$, ITIC) used in this work. Both PBDCS and PBDS comprise identical planar backbone structures except for the presence of the aggregation promoter, β-cyano groups in PBDCS. This small difference in the molecular structure could induce significant differences in the aggregation property of polymers and the resulting D:A blend morphology. The unique resonance structure of PBDCS induces tight molecular stacking and strong temperature-dependent aggregation property compared to PBDS. [45] To optimize the geometry and compare the backbone structures at the ground state, computational studies using DFT calculations were conducted for the trimers of PBDCS and PBDS. The alkyl and alkoxy side chains were replaced by the methyl and methoxy

groups for computational simplicity. As shown in Figure 4-2, PBDCS and PBDS trimers have an identical backbone curvature with an almost planar structure at the ground state. Therefore, we believe that we can see the sole effect of 'aggregation' while excluding the effects of the backbone curvature and primary chemical structure on the miscibility between donor and acceptor molecules, blend morphology and resulting photovoltaic properties.

$PC_{71}BM$ and ITIC were selected as the fullerene and NFAs in PSCs, respectively, where $PC_{71}BM$ has a spherical structure and ITIC has a linear A-D-A architecture. Due to the different structure of acceptor molecules and polymer aggregation properties, the D:A blend systems using PBDCS and PBDS as a donor and $PC_{71}BM$ and ITIC as an acceptor could be an ideal model to correlate the blend morphology and photovoltaic properties.

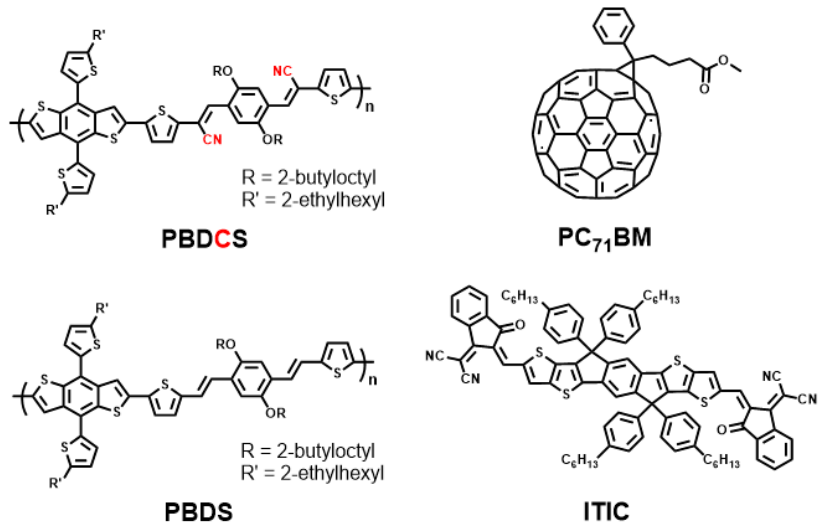

Figure 4-1 Molecular structures of PBDCS, PBDS, $PC_{71}BM$ and ITIC.

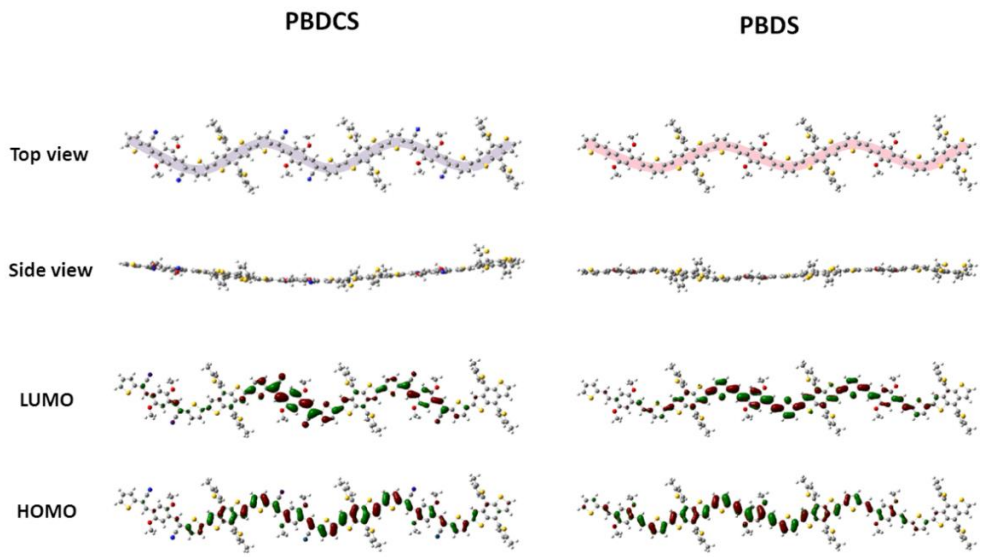

Figure 4-2 Optimized geometries and DFT-calculated HOMO and LUMO surfaces at the B3LYP/6-311G(d,p) level, and schematic showing the backbone curvatures of PBDCS [45] and PBDS.

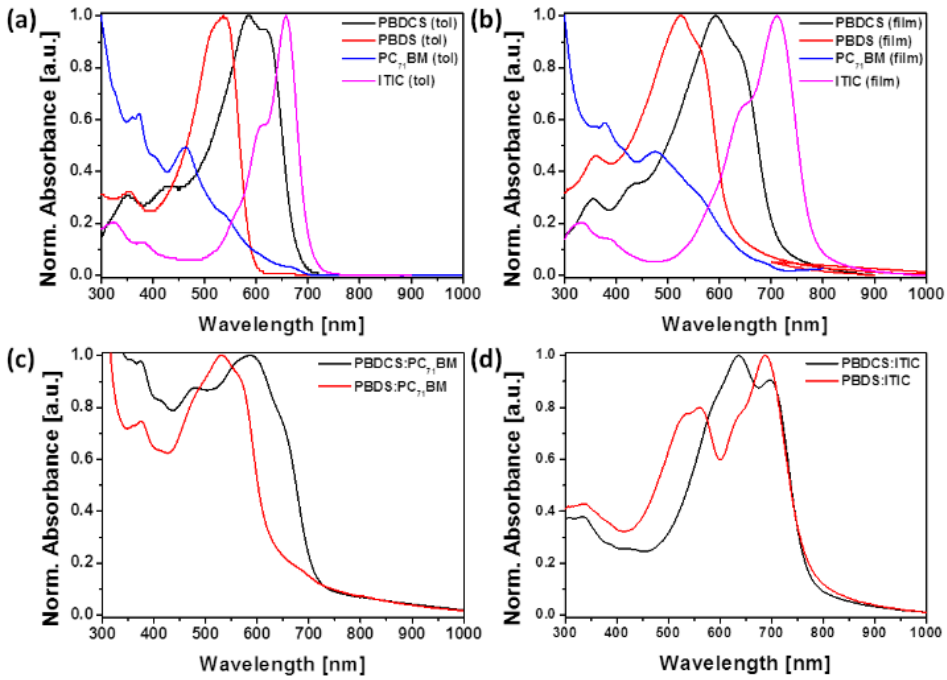

Figure 4-3 UV-vis absorption spectra of PBDCS, PBDS, $PC_{71}BM$ and ITIC (a) in toluene solutions, and (b) films, (c) PBDCS:$PC_{71}BM$ and PBDS:$PC_{71}BM$ films and (d) PBDCS:ITIC and PBDS:ITIC films.

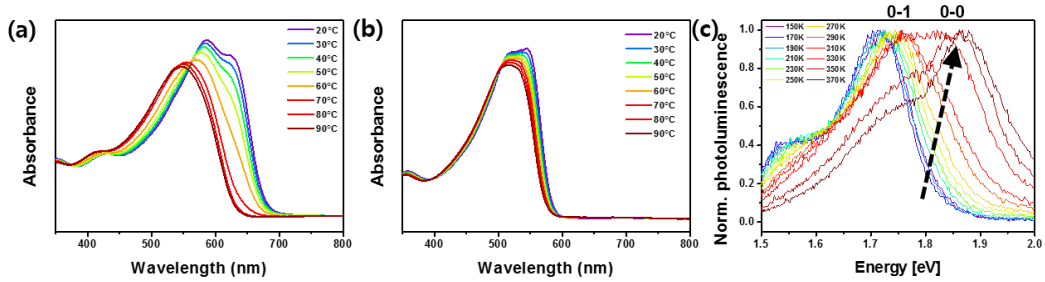

Figure 4-4 Temperature dependent absorption spectra of (a) PBDCS [45], (b) PBDS and (c) phoroluminescence spectra of PBDCS in diluted chlorobenzene.

To explore the effect of cyano group substitution as an aggregation promotor on the optoelectronic properties of the polymers, the UV-vis absorption spectra of PBDCS and PBDS were measured in the solution and film states as shown in Figure 4-3(a,b). While PBDS exhibits an unstructured maximum absorption peak at 530 nm, PBDCS exhibits a red-shifted absorption peak comprising clear vibrational progression at 620 nm (0-0) and 584 nm (0-1) in the solution state. This structured absorption peak of PBDCS suggests the interchain-interaction dominated aggregation in solution. Indeed, temperature-dependent absorption change of this vibrational progression was made in our earlier work. [45] From the temperature-dependent absorption and photoluminescence change (Figure 4-4) in diluted PBDCS solution, it was noted that excitons are formed mainly from the interchain chromophore coupling due to the strong interchain interaction in PBDCS aggregates. [49-51] The aggregation-induced absorption peak with vibrational progression was shown at room temperature and disappeared at high temperatures as the aggregation was broken by thermally activated vibrational and rotational motions of PBDCS in solution, while this temperature-dependent feature is much weakened in PBDS solution as shown in Figure 4-4. [45] Due to this strong aggregate formation property in solution, PBDCS is advantageous for making pure and larger polymer domains in film states. It is shown that the absorption spectra of PBDCS, PBDS, and ITIC in film states are all red-shifted by about 20-50 nm compared to the solution ones. In general, molecular structure is more planar in the solid

state than the solution, which enhances electron delocalization and intermolecular interaction, leading to the red-shift of absorption bands. [40,51-52]

The absorption spectra of the blend films are shown in Figure 4-3(c,d). Both PBDCS:$PC_{71}BM$ and PBDS:$PC_{71}BM$ blend films exhibit polymer absorption between 450-750 nm and $PC_{71}BM$ absorption below 450 nm, and ITIC blends also exhibit both polymer absorption and ITIC absorption. To estimate the extent of ITIC aggregation in the blend films, we compared the absorption maxima of ITIC with those of the solution and neat film states. ITIC exhibits maximum absorption at 711 nm in the neat film, whereas ITIC solution exhibits maximum absorption at 658 nm. Furthermore, PBDCS:ITIC exhibits ITIC absorption maximum at 696 nm, while PBDS:ITIC exhibits ITIC absorption maximum at 688 nm. The blue-shifted ITIC absorption in the blend films indicates the nanoscale phase-separated ITIC domains compared to the ITIC neat film. The relationship between the absorption property and blend phase separation has been reported through the morphology control strategy such as solvent additive processing. [52-53] Blend with the phase-separated domains exhibited a red-shifted absorption spectrum compared to that of the highly mixed blend system due to the stronger aggregation and intermolecular interaction between neighboring molecules. Therefore, the blue-shifted ITIC absorption spectra in PBDCS:ITIC and PBDS:ITIC blend films are due to the mixing of the donor and acceptor, and reduced aggregation of ITIC molecules than the ITIC neat film. In addition, the red-shifted ITIC absorption in PBDCS:ITIC compared to PBDS:ITIC originates from the different aggregation

properties of donor polymers, and consequent penetration feature of ITIC in polymer domains. From these results, we could confirm that ITIC molecules are much more aggregated in PBDCS:ITIC than in PBDS:ITIC. [52]

Table 4-1 Photovoltaic parameters and photoluminescence (PL) quenching efficiency of PBDCS:$PC_{71}BM$, PBDCS:ITIC, PBDS:$PC_{71}BM$ and PBDS:ITIC BHJ PSCs under AM 1.5G solar illumination.

	V_{oc} [V]	J_{sc} [mA/cm^2]	FF	PCE [%]	PL quenching [%]
PBDCS :$PC_{71}BM$[a]	0.94	14.3	0.65	8.75	92.2[b]
PBDCS : ITIC[a]	1.06	14.0	0.53	7.81	92.1[b], 69.8[c]
PBDS :$PC_{71}BM$	0.81	10.0	0.62	5.00	94.7[b]
PBDS : ITIC	0.86	2.68	0.33	0.76	98.1[b], 96.6[c]

[a] Data from previously reported paper [45] Reproduced by permission of The Royal Society of Chemistry

[b] PL quenching efficiency for the donor (PBDCS, PBDS) excitation

[c] PL quenching efficiency for the acceptor (ITIC) excitation

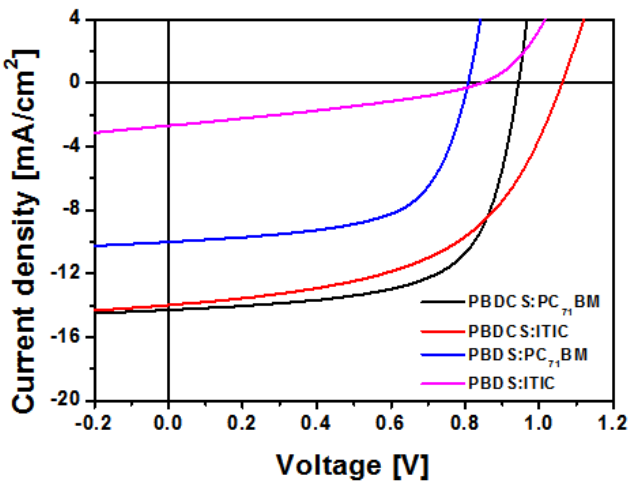

Figure 4-5 *J–V* curves of PBDCS:$PC_{71}BM$, PBDCS:ITIC, [45] PBDS:$PC_{71}BM$, and PBDS:ITIC solar cells illuminated under AM 1.5G, 100 mW/cm^2.

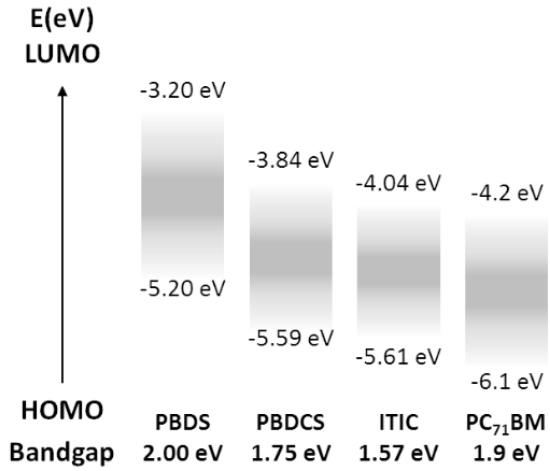

Figure 4-6 Schematic energy diagram of PBDCS, PBDS, ITIC and $PC_{71}BM$.

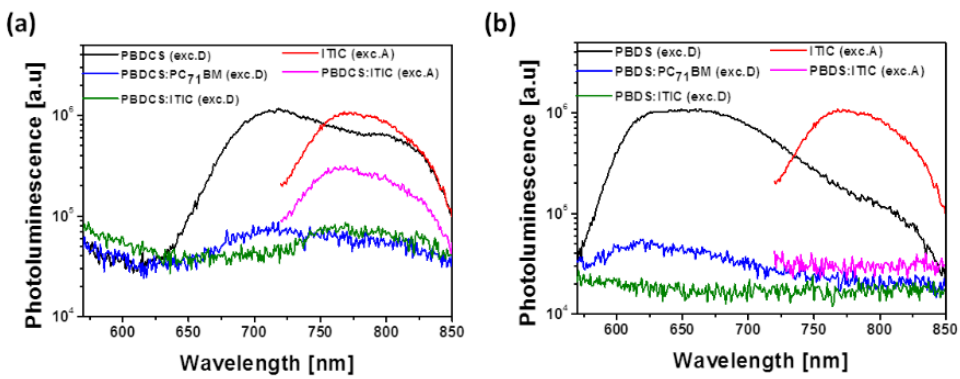

Figure 4-7 PL quenching spectra for blend films with respect to donor polymer films, where all films were excited at 550 nm and 720 nm wavelength and PL intensity corrected for the absorption intensity of the films at 550 nm and 720 nm.

To evaluate and compare the photovoltaic performances of the blend systems, BHJ PSCs were fabricated using PBDCS and PBDS as a donor polymer, and $PC_{71}BM$ and ITIC as an acceptor with the following device architecture: ITO/PEDOT:PSS/active layer/Ca or PFN/Al. The current density–voltage (*J*–*V*) curves are shown in Figure 4-5, and detailed photovoltaic parameters are listed in Table 4-1. The optimized PSCs using the PBDS donor polymer with $PC_{71}BM$ and ITIC acceptors exhibited a significant difference in PCE with 5.00 and 0.76%, respectively. On the other hand, PBDCS:$PC_{71}BM$ and PBDCS:ITIC PSCs exhibited similarly high PCEs of 8.75 and 7.81%, respectively. [45] When the donor polymer was changed from PBDCS to PBDS, V_{OC} is greatly reduced. From the film state energy levels of donor and acceptor materials estimated from the cyclic voltammetry analysis and optical bandgap as shown in Figure 4-6, the HOMO level of PBDS is higher-lying than that of PBDCS. Therefore, the energy offset between the HOMO of the donor and the LUMO of the acceptor is larger in PBDCS blend films, resulting in a higher V_{OC} value in photovoltaic devices. Furthermore, the PSCs using PBDCS exhibited a much higher J_{SC} value than the PSCs using PBDS, indicating significant differences in the charge generation and extraction ability of photoactive blends in the devices. Changing the acceptor material from $PC_{71}BM$ to ITIC also caused a significant difference in FF, resulting from the blend morphology and following photoinduced processes.

To investigate the difference in photo-induced charge transfer between donor and acceptor molecules in the blend system, steady-state photoluminescence (PL)

measurements were conducted. As shown in Figure 4-7, blend films exhibited a much lower PL intensity compared to donor neat films because excitons are converted to charge carriers at the D/A interface. PL quenching efficiencies were calculated using the maximum PL intensity of each neat polymer and blend films as listed in Table 4-1. After selective excitation of donor polymers at 550 nm, PBDCS blend films exhibited relatively smaller PL quenching efficiencies of 92.2 and 92.1% than PBDS films with those of 94.7 and 98.1% in the blends using $PC_{71}BM$ and ITIC, respectively, indicating less charge separation at the D/A interface in PBDCS blend films. In addition, the highest PL quenching efficiency of 98.1% for PBDS:ITIC indicates very efficient exciton dissociation and charge separation due to the extremely intermixed donor and acceptor molecules, which is beneficial for the exciton dissociation, but unfortunately disadvantageous for the charge transport in PSCs. Furthermore, for the ITIC excitation, PL quenching efficiencies are significantly different for PBDCS:ITIC and PBDS:ITIC blend films, with the values of 69.8 and 96.6%, respectively, also supporting the different morphology of blend films. In particular, upon the acceptor excitation, PBDS:ITIC exhibited a very high PL quenching efficiency consistently with the result of donor excitation. Such a significant increase in PL quenching efficiency is related to the extremely poor photovoltaic performance of the PBDS:ITIC device.

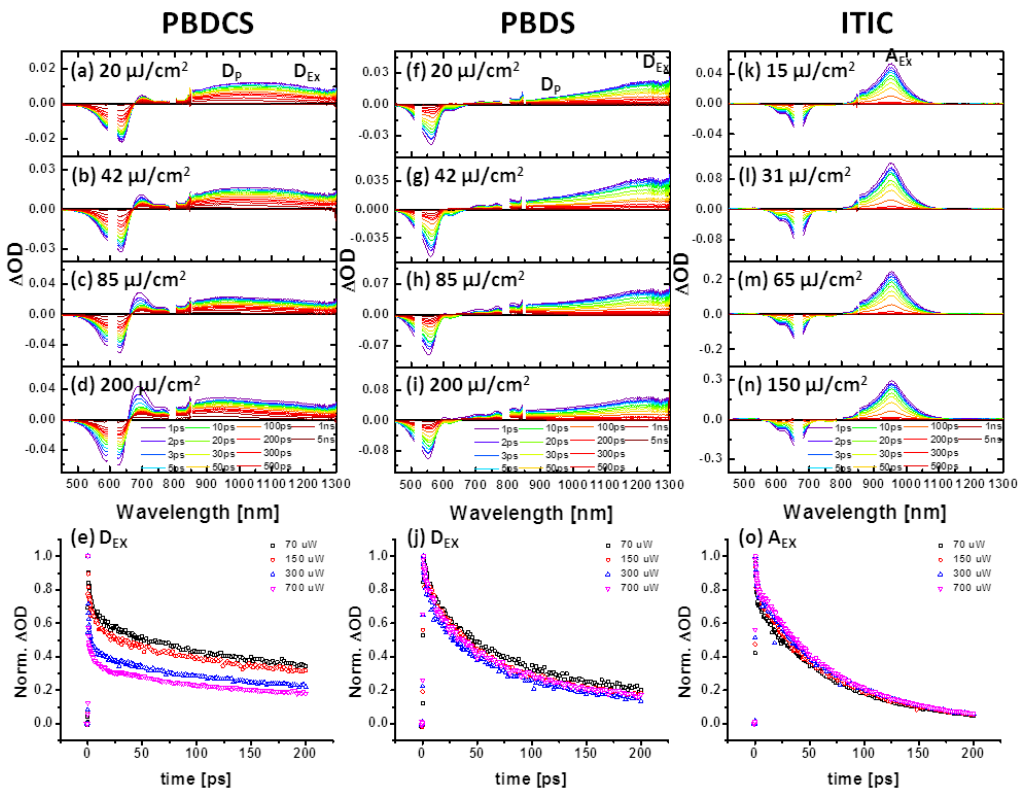

Figure 4-8 Femtosecond transient absorption spectra and decay profiles of singlet exciton of (a-e) PBDCS, (f-j) PBDS, and (k-o) ITIC in toluene at the different laser power. (D_{EX}, D_P and A_{EX} indicate the excited state absorption of donor exciton, donor polaron, and acceptor exciton, respectively).

Table 4-2 Time components of femtosecond transient absorption in PBDCS and PBDS solutions by fitting the decays to the multiexponential functions.

		τ_1 [ps]	τ_2 [ps]	τ_3 [ps]
PBDCS (tol)	**20 μJ/cm²**	1.5 ps (30%)	29 ps (17%)	470 ps (53%)
	42 μJ/cm²	0.80 ps (36%)	19 ps (20%)	480 ps (44%)
	85 μJ/cm²	0.80 ps (47%)	15 ps (13%)	370 ps (40%)
	200 μJ/cm²	0.20 ps (71%)	7.4 ps (9%)	321 ps (20%)
PBDS (tol)	**20 μJ/cm²**	20 ps (38%)	179 ps (62%)	
	42 μJ/cm²	24 ps (45%)	173 ps (55%)	
	85 μJ/cm²	14 ps (41%)	141 ps (59%)	
	200 μJ/cm²	17 ps (42%)	158 ps (58%)	
ITIC (tol)	**15 μJ/cm²**	5.2 ps (16 %)	74 ps (84 %)	
	31 μJ/cm²	1.6 ps (20 %)	71 ps (80 %)	
	65 μJ/cm²	2.0 ps (18 %)	74 ps (82 %)	
	150 μJ/cm²	1.0 ps (18 %)	74 ps (82 %)	

While the steady-state optical properties enabled us to predict the different morphology of blend films, a detailed study is required on the relationship between intrinsic polymer aggregation properties and excited-state dynamics in film states to understand photovoltaic properties. Now, we focus on the femtosecond transient absorption (fs-TA) measurements in toluene solutions using a laser with a time resolution of 200 fs to investigate the intrinsic aggregation property of donor polymers. The TA spectra of the solutions at various laser powers are shown in Figure 4-8, upon the excitation at 600 nm for PBDCS, 520 nm for PBDS, and 660 nm for ITIC solutions to be in resonance with the $S_0 \rightarrow S_1$ transition. For the PBDCS solution, the TA spectra have a ground-state bleach (GSB) in the visible 500-680 nm region and broad excited-state absorption (ESA) in the 700-1300 nm region, while the PBDS solution exhibited TA spectra composed of GSBs at 450-550 nm overlapping with stimulated emission (SE) in the visible 550-700 nm region, and broad ESA over the 700-1300 nm region. Through the power density-dependence measurements, ESA bands of the singlet exciton and polaron were assigned to both PBDCS and PBDS solutions. This is based on the assumption that the polaron absorption should increase at the cost of singlet excitons as laser power increases. [54] At the high laser fluence, singlet excitons possessing higher energy are formed via the exciton–exciton annihilation process, facilitating charge separation and polaron generation through the hot exciton dissociation such as rr-P3HT polymers. [55] Other nonlinear effects such as saturable absorption or two photon

absorption processes may also be possible at a high laser fluence within an ultrafast time range. [56] In addition, it is noted that the SE band decreases in PBDS solution as laser power increases due to exciton-exciton annihilation and following polaron formation. [57] In the PBDCS solution, singlet exciton absorption peaking at 1200 nm overlaps with polaron absorption at 930 nm. In the PBDS solution, singlet exciton peaking at 1250 nm overlapped with polaron absorption at 900 nm. Importantly, we could find differences induced by different aggregate formation properties of PBDCS and PBDS from their solution TA spectra and exciton decay dynamics (see Table 4-2 for the time constants). In the PBDCS solution, there was a remarkable increase in the polaron absorption band and fast decay in the singlet exciton dynamics with a lifetime of 0.2-1.5 ps, where the proportion of this fast decay term is gradually enhanced by increasing the number of photons, as shown in Figure 4-8. On the other hand, there was little increase in the polaron absorption, and no fast decay in the singlet exciton dynamics in the PBDS solution with different laser powers. These contrasting exciton decay dynamics unambiguously suggest the unique solution aggregation behavior of PBDCS. Considering the difference in the chemical structure, PBDCS has stronger π-π interactions than PBDS, and then, easily forms the aggregates even in the solution. Due to the tightly stacked structure and aggregation of PBDCS, excitons can easily diffuse through the aggregates and interact with each other with a higher probability, resulting in the increased exciton-exciton annihilation and exciton dissociation, which is less likely in PBDS solution. It is also noted from Figure 4-8 (a) that the more excitons of

PBDCS are generated and the more exciton-exciton annihilation process is reinforced under the higher laser fluence according to the quadratic kinetics of polaron generation. [58-59]

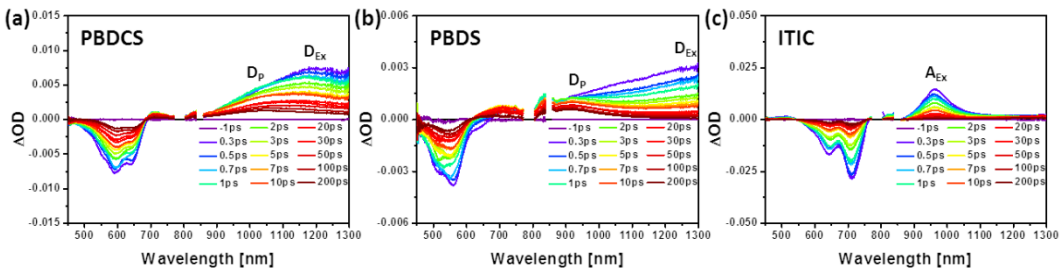

Figure 4-9 Femtosecond transient absorption spectra of (a) PBDCS, (b) PBDS excited at 550 nm and (c) ITIC films excited at 720 nm.

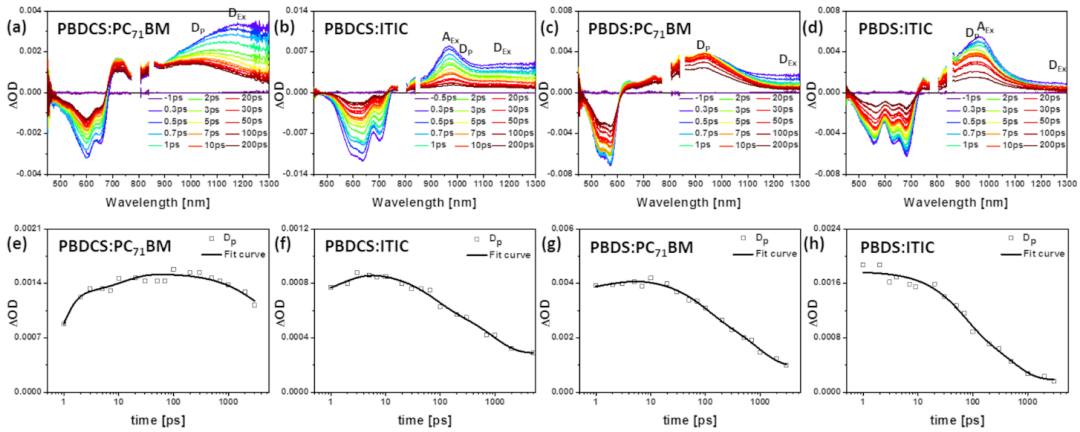

Figure 4-10 (a-d) Femtosecond transient absorption spectra and (e-h) rise-decay profiles of donor polaron absorption by deconvolution of TA spectra using Gaussian fitting of (a,e) PBDCS:PC$_{71}$BM, (b,f) PBDCS:ITIC, (c,g) PBDS:PC$_{71}$BM and (d,h) PBDS:ITIC blend films excited at 550 nm.

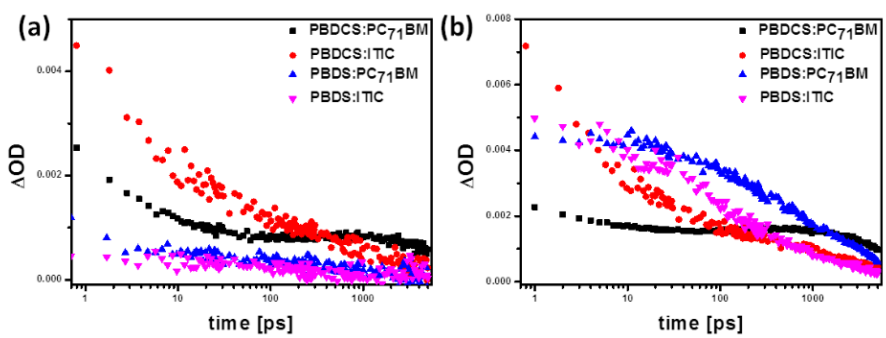

Figure 4-11 Decay profiles of (a) donor singlet exciton and (b) donor polaron absorption in PBDCS:PC$_{71}$BM, PBDCS:ITIC, PBDS:PC$_{71}$BM, and PBDS:ITIC blends within 5 ns.

Based on the solution fs-TA results, different aggregation properties of PBDCS and PBDS were observed. To focus our discussion on the intrinsic excited-state dynamics in solid states, neat films of PBDCS, PBDS, and ITIC were used in pump-probe experiments. TA spectra of PBDCS, PBDS, and ITIC neat films are shown in Figure 4-9, with the photoexcitation at 550 nm for both donor polymers, and 720 nm for ITIC. The PBDCS neat film shows a GSB signal at 450-700 nm with a broad ESA over 700-1300 nm, where the singlet exciton has absorption spectrum peaking at 1150 nm and polaron absorption at 1000 nm. PBDS neat film shows GSB in 450-600 nm with broad ESA over 600-1300 nm, where singlet exciton absorption maximum is 1300 nm and polaron absorption maximum is 930 nm. Both donor polymers exhibit efficient polaron formation in neat films owing to the interchain charge separation, which was absent in the solution of PBDS (*vide supra*). Very prominently, polaron absorption bands in PBDCS and PBDS are clearly correlated with a long-lived GSB signal, which is indicative of charge separation in polymer neat films comprising the energy transfer from the disordered region to the ordered region and formation of charge carriers through interchain charge separation. [41,60-61] TA results of ITIC were already reported in several papers, and the singlet exciton of ITIC was assigned with a sharp absorption peaking at 970 nm. [46,62] The average lifetimes of singlet excitons of PBDCS, PBDS, and ITIC are 106, 44, and 17 ps, respectively. Due to the tight π-π stacking and much more ordered regions, PBDCS exhibited the longest singlet exciton lifetime among the films.

To understand the excited-state dynamics in the photoactive layers of BHJ PSCs, blend films using PBDCS and PBDS as donor polymers and ITIC and $PC_{71}BM$ as acceptor molecules were made under the same conditions for the fabrication of optimized PSC devices, and the time-resolved absorption spectra of these films were measured using a laser with a time resolution of 200 fs. As shown in Figure 4-10, significant differences are noteworthy in the TA spectra and excited-state dynamics of the BHJ blend systems. First, the lifetime of the polymer singlet exciton is significantly different among the blend films. While early TA spectra of the PBDCS blend films are dominated by the polymer exciton absorption, those of PBDS blend films are highly suppressed. Thus, blend films using the PBDCS donor polymer exhibit a much larger and longer-lived exciton absorption with the absorption band at 1150 nm (D_{EX} in Figure 4-10 (a,b) and Figure 4-11) than PBDS blend films with singlet exciton absorption at 1300 nm (D_{EX} in Figure 4-10 (c,d) and Figure 4-11). In particular, it is noted that the PBDS:ITIC blend film has negligible PBDS singlet exciton absorption even at 0.3 ps after photoexcitation. The lifetime of the donor singlet exciton is related to the size and/or purity of donor domains in the blend films. The singlet excitons excited inside the domain diffuse to the D/A interface, hence the TA spectra represent the exciton absorption during the exciton diffusion. The larger and purer the polymer domains are, the longer-lived singlet excitons diffuse to reach the D/A interface. Therefore, longer-lived singlet excitons in PBDCS blend films indicate large and pure PBDCS domains as shown in Figure 4-11. On the other hand, ultrafast disappearance of PBDS singlet

exciton absorption in the PBDS:ITIC blend film indicates that almost all excitons are immediately quenched, and charges are separated on the ultrafast time scale at D/A interfaces because of excessively intermixed PBDS and ITIC molecules and negligible phase separation in the BHJ film. In addition, energy transfer from the donor to acceptor should occur in the ITIC blend films due to the spectral overlap between donor emission and ITIC absorption. After donor excitation with a 550 nm pump beam, fast energy transfer from the donor to acceptor competes with the charge transfer process. As a result, the sharp absorption of the ITIC singlet exciton (maximum at 970 nm, A_{EX} in Figure 4-10 (b,d)) simultaneously appears with the absorption of the donor singlet exciton in the TA spectra after donor excitation in both PBDCS:ITIC and PBDS:ITIC blend films. However, the disappearance rate of the ITIC acceptor exciton is quite different for both films. The sharp absorption band of ITIC clearly remains after 30 ps in the PBDCS:ITIC film, whereas the absorption of ITIC disappears within 3 ps in PBDS:ITIC. This result also came from the different film morphology of those films. As mentioned above using the steady-state absorption properties of ITIC (Figure 4-3), ITIC molecules aggregate more efficiently in PBDCS:ITIC, resulting in longer-lived ITIC excitons in PBDCS:ITIC than in the PBDS:ITIC blend. The different decay behavior of ITIC absorption is also shown in the case of ITIC excitation. For PBDCS:ITIC and PBDS:ITIC blend films, TA spectra were measured upon the acceptor excitation with a 720 nm pump beam. As shown in Figure 4-12, faster disappearance of sharp ITIC exciton absorption (maximum at 970 nm) in PBDS:ITIC compared to PBDCS:ITIC indicates much less aggregated

ITIC molecules and intermixed blend morphology in PBDS:ITIC, consistent with the difference in ITIC absorption and PL quenching efficiency from the steady-state absorption and PL results.

Second, the difference in blend morphology could also be monitored by the rise-decay profiles of polymer polarons. The loss of donor exciton absorption is synchronized by the rise of the polaron absorption band ranging over 900-1100 nm. Because the ESA spectra of each state of the donor and acceptor overlap in the near IR region, the rise-decay profile of the donor polaron was obtained by the deconvolution of the TA spectrum at each delay time. By plotting the maximum ESA intensity versus delay time, the rise-decay profile of donor polarons was obtained as shown in Figure 4-10 (e-h). It should be noted that the rise time constant of the donor polaron correlates well with its singlet exciton decay. Depending on the size and purity of domains, there are ultrafast polaron generation at the D/A interface and delayed polaron generation due to the exciton diffusion within the domain. In the PBDCS:$PC_{71}BM$, only a small fraction (20%) of the ultrafast polaron generation appears, and the delayed polaron generation time is the longest with a time constant of 0.5 and 12 ps because the phase separation is the largest among the blends. In the case of PBDCS:ITIC and PBDS:$PC_{71}BM$, a larger fraction of the ultrafast polaron generation (60 and 85%, respectively) appear, and the delayed polaron generation time constant is shortened to 1.6 and 2.0 ps, respectively, due to the relatively small and impure domains compared to PBDCS:$PC_{71}BM$. On the other hand, PBDS:ITIC only exhibited ultrafast polaron generation due to the excessively intermixed

D/A morphology over the entire film. In this case, phase separation is negligible and almost all excitons exist near the D/A interfacial area, resulting in ultrafast exciton dissociation, which is consistent with the PL quenching results (Table 4-1). Consequently, in the phase-separated blend films, the singlet excitons diffuse a longer distance in the large and pure domains, and then generate charge carriers at the D/A interface with the delayed charge separation time.

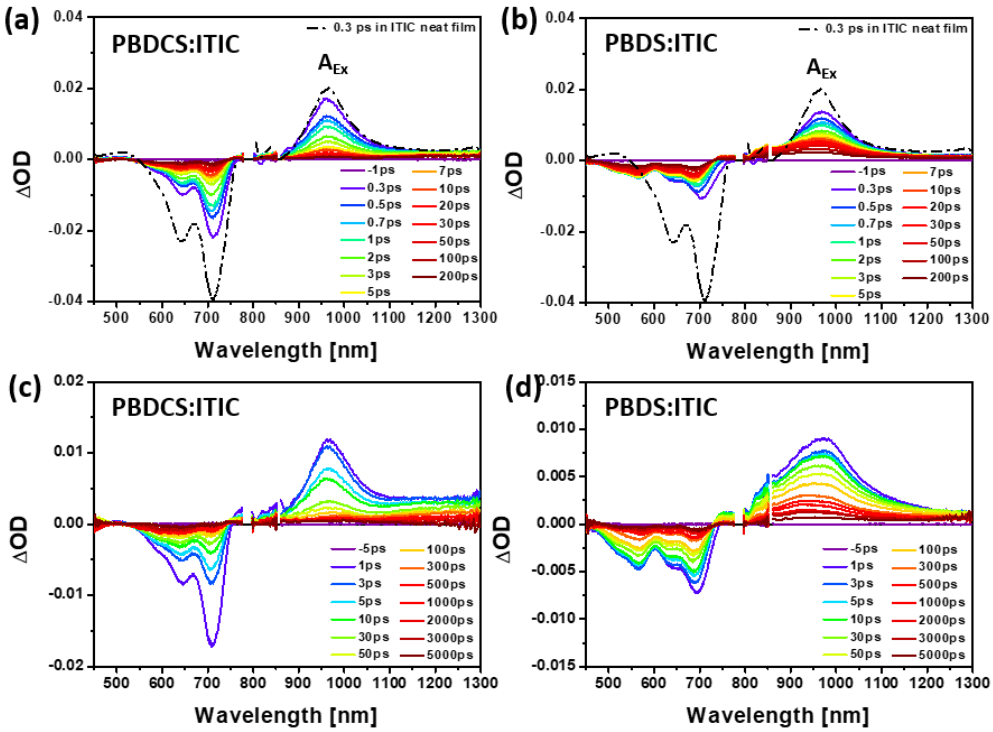

Figure 4-12 Femtosecond transient absorption spectra of (a,c) PBDCS:ITIC and (b,d) PBDS:ITIC blend films excited at 720 nm within 200 ps and 5 ns time scale. (dash-dotted line : 0.3 ps TA spectrum in ITIC neat film)

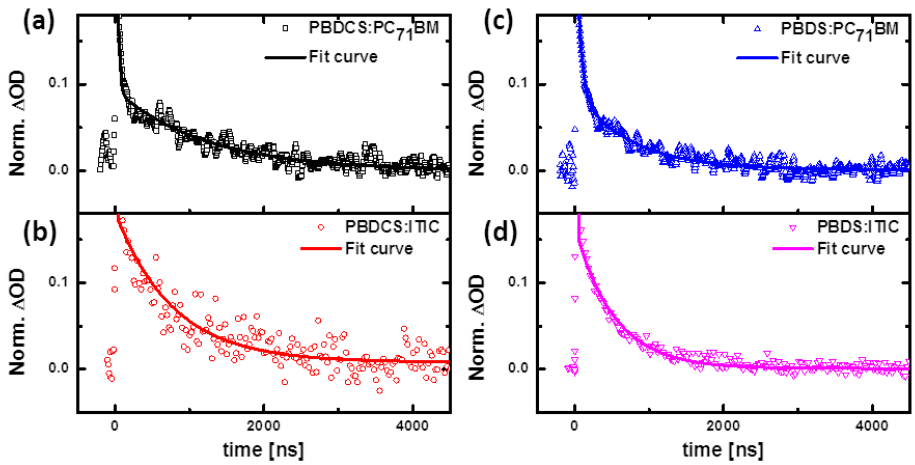

Figure 4-13 Decay profiles at polaron absorption using RIPT method in (a) PBDCS:$PC_{71}BM$, (b) PBDCS:ITIC, (c) PBDS:$PC_{71}BM$, and (d) PBDS:ITIC blend films.

Table 4-3 Time components of transient absorption using RIPT method in PBDCS:$PC_{71}BM$, PBDCS:ITIC, PBDS:$PC_{71}BM$, and PBDS:ITIC blend films by fitting the decays to the biexponential functions.

	τ_1 [ns]	τ_2 [ns]
PBDCS:$PC_{71}BM$	25	1200
PBDCS:ITIC	15	770
PBDS:$PC_{71}BM$	50	750
PBDS:ITIC	17	525

While the charge generation dynamics were studied by the fs-TA rise profile of polaron absorption in Figure 4-10, the charge recombination dynamics at the D/A interface were separately investigated over the 4.5 μs time range to compare the lifetime of long-lived extractable charges for the blends using the sub-nanosecond transient absorption measurements as shown in Figure 4-13. The polaron decay profiles of blend films all exhibited a biexponential decay (Table 4-3). The first decay term of each blend film has a lifetime of tens of nanoseconds, and exhibits power-dependent behavior, and this fast decay term is complex combination of short time scale processes such as exciton-exciton annihilation, exciton decay and geminate recombination. The second decay term with a lifetime in the range of several hundreds of nanoseconds to microseconds results from the charge carrier nongeminate recombination. PBDCS:$PC_{71}BM$ exhibited the longest lifetime of 1.2 μs due to the large and pure domains with the phase-separated blend morphology. The longer-lived polaron in the PBDCS:$PC_{71}BM$ blend film is beneficial for extracting charges to the electrodes, resulting in an increase of photocurrent. On the other hand, PBDS:ITIC has the shortest charge carrier lifetime of 520 ns due to its molecular-scale intermixed matrix with negligible phase separation, which is disadvantageous for the charge transport to the electrodes. Combining the results of charge generation and recombination, BHJ blend morphology has a significant impact on the excited state dynamics. The large and pure domain system in PBDCS:$PC_{71}BM$ exhibited delayed charge separation but polarons showed the longest lifetime among the blend films, while the excessively intermixed

system in PBDS:ITIC exhibited ultrafast and efficient charge generation but short polaron lifetime.

The transient absorption results indicate significantly different charge generation and polaron lifetime in BHJ blends due to distinct film morphologies. These results are also supported by the time-dependent anisotropy measurements. With the excitation using a 550 nm beam, the transient absorption spectra at each delay time were measured using a probe beam parallel and perpendicular to the pump beam polarization. The transient absorption anisotropy probed at donor polaron absorption (1000 nm for PBDCS blend films, and 930 nm for PBDS blend films) is calculated by the following equation: $r(t) = \frac{\Delta OD_{\parallel} - \Delta OD_{\perp}}{\Delta OD_{\parallel} + 2 \times \Delta OD_{\perp}}$, as shown in Figure 4-14. In the case of PBDCS:$PC_{71}BM$, the initial anisotropy value is 0.18, which drops to 0.10 after 1 ps, and then gradually decreases to 0.03 at 200 ps after photoexcitation. This anisotropy decay is due to the exciton dissociation and hopping of mobile charge carriers, which lose their memory of polarization, indicating a large domain size for exciton diffusion and charge transport. On the other hand, PBDS:ITIC exhibits a lower initial polarization anisotropy of 0.10, and the anisotropy decreases to 0.07 after 1 ps, and then virtually retains the value showing 0.06 up to 200 ps. Compared to PBDCS:$PC_{71}BM$, PBDS:ITIC has a lower initial anisotropy value due to the ultrafast charge separation, however, it maintains the anisotropy value within the initial 200 ps. This result is due to the trapped charges with the negligible phase separation of PBDS:ITIC, indicating the charge carriers are

immobile and retain their polarization at the D/A interface. PBDCS:ITIC and PBDS:$PC_{71}BM$ blends exhibit lower initial anisotropy than PBDCS:$PC_{71}BM$, however, they also exhibit a faster decay of the anisotropy value than PBDS:ITIC, indicating the moderate size of domains and film morphologies.

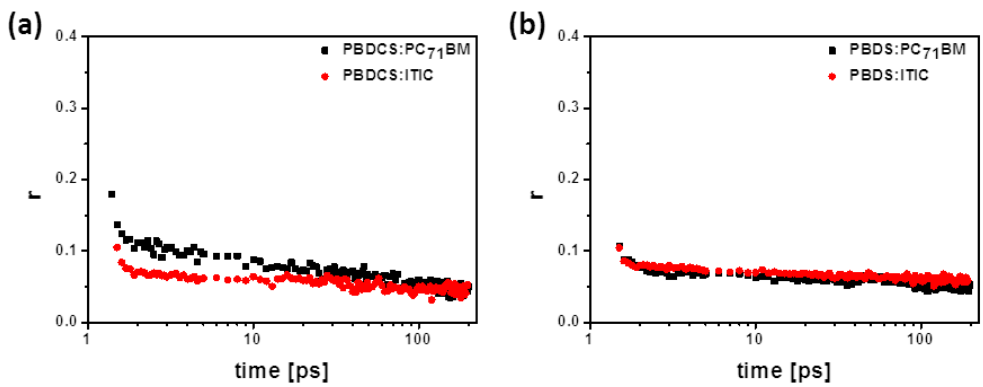

Figure 4-14 Femtosecond transient anisotropy decays of (a) PBDCS:$PC_{71}BM$ and PBDCS:ITIC at 1000 nm, (b) PBDS:$PC_{71}BM$ and PBDS:ITIC blend films at 930 nm. The excitation wavelengths were 550 nm.

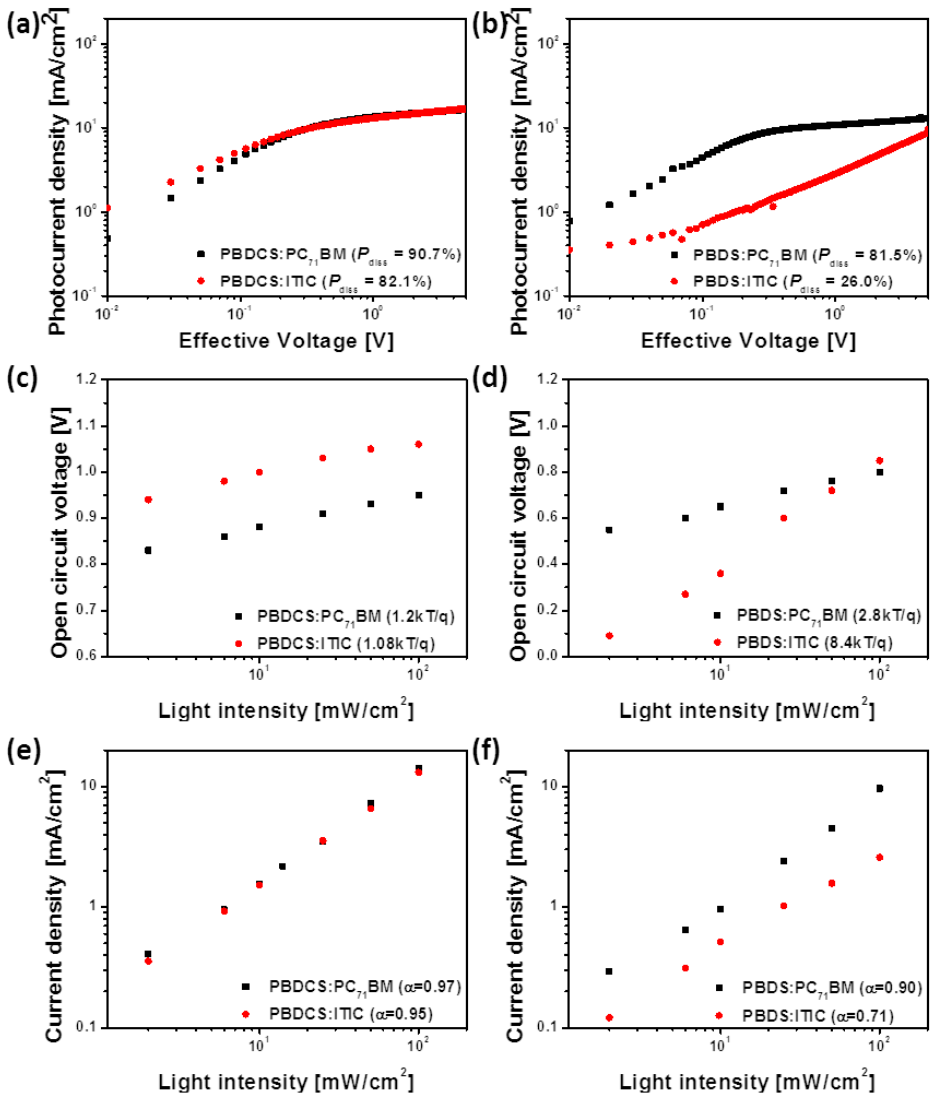

Figure 4-15 Photocurrent density (J_{ph}) as a function of the effective voltage (V_{eff}), light intensity (P_{light}) dependence of V_{OC} and J_{SC} in (a,c,e) PBDCS:PC$_{71}$BM and PBDCS:ITIC and (b,d,f) PBDS:PC$_{71}$BM and PBDS:ITIC BHJ PSCs.

From the transient absorption results, we can understand the process of charge generation and polaron decay dynamics in different BHJ systems. However, there is still a point to consider whether these different polaron dynamics can be correlated with the actual charge recombination processes in the active layer of real photovoltaic devices.

To get a better understanding of the relationship between the morphology of each BHJ film and exciton dissociation/charge recombination behavior in the OPV device, we measured the exciton dissociation efficiency (P_{diss}) and variation of the V_{oc} and J_{sc} depending on light intensity (P_{light}) as shown in Figure 4-15. Figure 4-15 (a,b) presents the dependence of photocurrent density (J_{ph}) on the effective voltage (V_{eff}). J_{ph} is defined as $J_{ph} = J_L - J_D$, where J_L and J_D are the current densities under illumination and dark conditions, respectively. V_{eff} is defined as $V_{eff} = V_0 - V_a$, where V_0 is the voltage when J_{ph} = 0 and V_a is the applied bias voltage. By normalizing J_{ph} (under short circuit conditions) with J_{sat} (using the J_{ph} value at V_{eff} = 5 V), exciton dissociation efficiency is calculated. [63] The P_{diss} values were 90.7% for PBDCS:$PC_{71}BM$, 82.1% for PBDCS:ITIC, 81.5% for PBDS:$PC_{71}BM$ and 26.0% for PBDS:ITIC, respectively. Large P_{diss} values in PBDCS PSCs present the efficient charge generation and transport to the electrodes compared to the PBDS PSCs. In particular, the PBDS:ITIC PSC exhibited a very low P_{diss} value due to the inefficient charge transport based on the very low extent of phase separation.

The relationship between V_{OC} and light intensity can be described as $V_{OC} \propto n(kT/q)\ln(P_{light})$, where n, k, T, q, and P_{light} refer to the ideal factor, the Boltzmann constant, the absolute temperature, the elementary charge, and the light intensity, respectively. The slope of the V_{OC} versus light intensity indicates the dominant recombination mechanism. If the monomolecular (trap-assisted) recombination is negligible in the device, the slope of the device is close to 1 kT/q. In contrast, strong bimolecular/trap-assisted recombination in devices exhibit large deviation of the slope from 1 kT/q. [64-66] For the OPV devices with the respective BHJ, the slope values were estimated as follows; 1.2 kT/q for PBDCS:$PC_{71}BM$, 1.08 kT/q for PBDCS:ITIC, 2.8 kT/q for PBDS:$PC_{71}BM$, and 8.4 kT/q for PBDS:ITIC. The device with the PBDCS donor exhibited a much less trap-assisted recombination. Unlike PBDCS-based devices, OPV devices using PBDS showed a larger slope and strong deviation, which indicates that not only the monomolecular but also the bimolecular recombination processes occur to the higher degree. Particularly, the very large deviation from the kT/q in the PBDS:ITIC device is indicative of strong trap-assisted recombination due to the excessively intermixed blend morphology with a negligible phase separation as described from the fs-TA and PL quenching results.

The dependence of the J_{SC} on the light intensity could explain the extent of non-geminate recombination losses in the devices. The relationship between J_{SC} and the light intensity is described as the equation: $J_{SC} \propto {P_{light}}^{\alpha}$. When α value is close to unity, the

bimolecular recombination is negligible and charge transport is ideal, where $\alpha<1$ indicates that the bimolecular recombination competes with the charge extraction. [66-67] For the devices using PBDCS, the α value is 0.97 and 0.95 for the PBDCS:$PC_{71}BM$ and PBDCS:ITIC, respectively, indicating weak bimolecular recombination throughout the device. This is well-correlated with the long-lived polaron lifetime of 1200 ns from subnanosecond TA experiments. On the other hand, the devices using PBDS polymer exhibited a stronger deviation with the α values of 0.90 and 0.71, which indicates that the photocurrent is limited by substantial bimolecular recombination losses resulting from small and impure domains of morphology. In particular, the α value in the PBDS:ITIC-based device is highly low due to the extremely poor blend morphology, and this large degree of bimolecular recombination is in line with the shortest polaron lifetime from the subnanosecond TA experiments. Consequently, from the light intensity dependence measurements using the photovoltaic device, strongly phase-separated blend morphology with large domains of the blend system using PBDCS induces a less bimolecular/trap-assisted recombination with longer-lived polarons, which is beneficial for extracting charges to the electrodes, despite the delayed charge separation. On the other hand, the PBDS:ITIC blend system exhibited very a efficient charge separation, but due to the shorter-lived polarons and a large amount of bimolecular/trap-assisted charge recombination, the charge transport is inefficient in excessively intermixed D:A morphology resulting in poor photovoltaic performances.

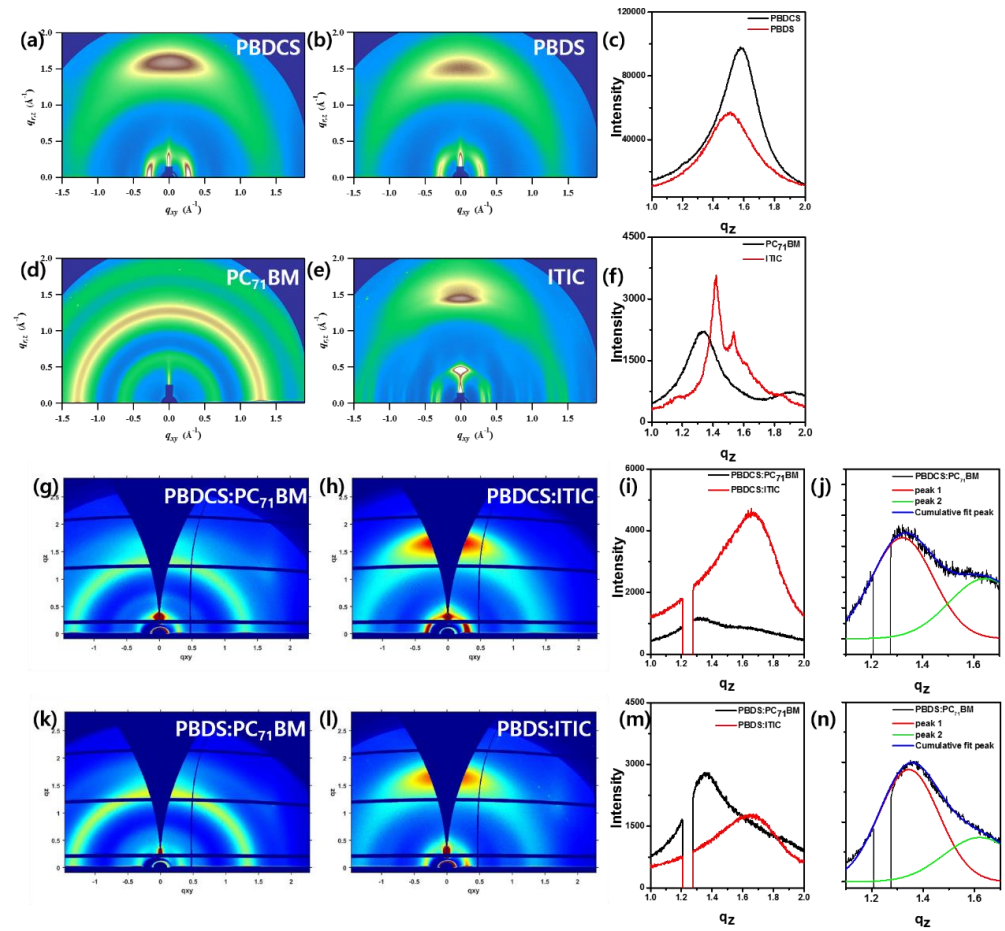

Figure 4-16 (a,b,d,e) 2D-GIXD images and (c,f) line-cut profiles (in the out-of-plane direction) of neat films (PBDCS [45], PBDS, $PC_{71}BM$ and ITIC). (g,h,k.l) 2D-GIXD images, (i,m) line-cut profiles (in the out-of-plane direction) of blend films (PBDCS:$PC_{71}BM$, PBDCS:ITIC, PBDS:$PC_{71}BM$ and PBDS:ITIC) and (j,n) deconvolution of PBDCS:$PC_{71}BM$ and PBDS:$PC_{71}BM$ blend films.

To gain insights into the morphological differences in films, 2D-GIXD measurements were performed for neat and blend films (Figure 4-16). PBDCS and PBDS neat films exhibited a π-π stacking peak in the out-of-plane direction, with the distances of 3.97 and 4.18 Å, respectively, indicating amuch tighter π-π stacking of PBDCS with the aid of an aggregation promoter. Furthermore, PBDCS:$PC_{71}BM$ and PBDS:$PC_{71}BM$ blend films exhibited a π-π stacking peak of PBDCS and PBDS at q_z ~ 1.58 and 1.53 $Å^{-1}$, respectively, with the anisotropic scattering peak of $PC_{71}BM$ at q_z ~ 1.30-1.33 $Å^{-1}$, indicating the coexistence of D and A regions. On the other hand, PBDCS:ITIC and PBDS:ITIC exhibited only a strong π-π scattering peak near q_z ~ 1.67 $Å^{-1}$. This is attributed to the overlap of π-π stacking peaks of polymers and ITIC, however, also indicating the well mixing of D and A regions, evidenced by the disappearance of the sharp ITIC peak at q_z ~ 1.42 $Å^{-1}$ in the blend films. The difference in the mixing ability of $PC_{71}BM$ and ITIC in the donor polymer regions is also supported by following analysis of contact angle measurements.

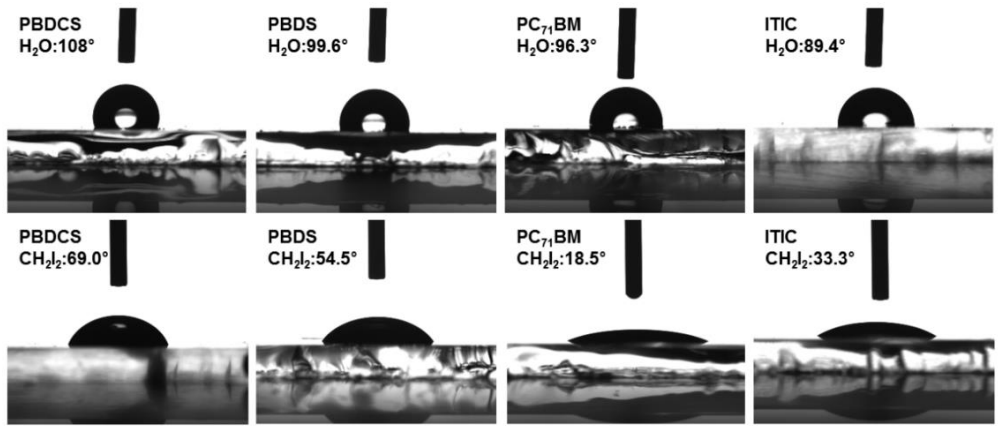

Figure 4-17 Images of surface contact angle measurements of PBDCS, PBDS, $PC_{71}BM$ and ITIC films. The measurements were carried out by using deionized water (upper layer) and diiodomethane (lower layer) as the wetting liquid.

Table 4-4 The contact angle and surface energy parameters of the PBDCS, PBDS, $PC_{71}BM$ and ITIC films.

	PBDCS	PBDS	$PC_{71}BM$	ITIC
$\theta_{DI\ water}$[a] [°]	108	99.6	96.3	89.4
θ_{DIM}[a] [°]	69.0	54.5	18.5	33.3
$\gamma_{disperse}$[b] [mN/m]	23.4	31.7	49.8	41.1
γ_{polar}[b] [mN/m]	0.11	0.32	0.01	1.17
γ_{total} [mN/m]	23.5	32.1	49.8	42.3

[a] $\theta_{DI\ water}$ and θ_{DIM} represent the contact angle using deionized water and diiodomethane, respectively. [b] $\gamma_{disperse}$ and γ_{polar} represent the surface free energies generated from the dispersion forces and the polar forces, respectively.

From the solution fs-TA results and previously reported temperature-dependent absorption property (shown in Figure 4-4), the strong aggregate formation property of PBDCS was already confirmed. However, there was a significant difference in TA spectra and dynamics of polarons in blend films using the same donor polymer. Therefore, we could speculate that the different morphology of blend films is also caused by the different miscibility of donor and acceptor molecules. Contact angle measurements of each donor and acceptor material were conducted to measure the surface energy and compare the miscibility of blend films. The deionized water and diiodomethane were used to measure the contact angle and the surface energies of each material using the Owens-Wendt equation. Relevant images and values are shown in Figure 4-17 and Table 4-4. The surface energies of donor and acceptor materials were 23.5 mN/m for PBDCS, 32.1 mN/m for PBDS, 49.8 mN/m for $PC_{71}BM$ and 42.3 mN/m for ITIC, respectively. In the case of PBDCS blend systems, PBDCS has formerly formed aggregates in the solution due to strong π-π stacking and intermolecular interaction, making it difficult for acceptor molecules to penetrate into the polymer region, resulting in large and pure PBDCS domains for efficient charge transport in blend films. Furthermore, as the surface energy difference between the donor and acceptor is larger in PBDCS:$PC_{71}BM$ than in PBDCS:ITIC, an appropriate phase-separated morphology is formed in PBDCS:$PC_{71}BM$. On the contrary, PBDS has a lack of aggregate formation ability, which induces a small domain size and results in an excessively miscible D/A blend. In addition, the difference of surface energy between

PBDS and $PC_{71}BM$ is much larger than that of PBDS and ITIC, which causes relatively larger domains. [68] In particular, the surface energy difference between the donor and acceptor is the smallest in PBDS:ITIC, causing the largest miscibility among the blends, and ITIC molecules are easy to penetrate and diffuse into the PBDS polymer. Consequently, due to the large difference in surface energies between PBDCS and acceptor molecules, the phase separation between PBDCS and the acceptor molecule is more appropriate than that of PBDS and acceptors, which is beneficial for charge collection in the device. Therefore, PBDCS blends exhibited much large and pure domains than PBDS blends and their phase-separated morphologies are important to suppress the charge recombination by separating charges into spatially segregated domains. These morphological differences are consistent with the previous steady-state PL properties.

4.4. Conclusions

In this paper, we compared the difference in the blend morphology, excited state dynamics, and resulting photovoltaic properties using the PBDCS and its analogue polymer PBDS as a donor polymer in the fullerene and NFA PSCs. Depending on the presence of an aggregation promotor (β-cyano groups) on the molecular backbones, PBDCS and PBDS have significantly different aggregation properties, resulting in

different morphologies in the blends with fullerene and NFAs. In the PBDCS blends, film morphology with pure and large domains was obtained due to the formerly formed aggregates of the donor polymer and relatively poor miscibility between donor and acceptor molecules, exhibiting efficient charge extraction. However, aggregates of the donor polymer were poorly formed in PBDS blends and the domain is significantly smaller and less pure than that of PBDCS blends. In the pure domain BHJ system using PBDCS, charge generation is delayed, but bimolecular and trap-assisted recombination are suppressed with long-lived polarons, beneficial for the charge extraction in the device. On the contrary, the BHJ system using PBDS exhibits intermixed blend morphology due to large miscibility between donor and acceptor materials, resulting in efficient charge separation, but poor charge collection with excessive bimolecular/trap-assisted recombination and short polaron lifetime. In this work, we could compare the aggregate formation property of donor polymers and the D:A blend morphology using donor polymers with nearly identical backbone structures, leading to a significant difference in excited-state dynamics in photoactive layer and photovoltaic performances.

4.5. References

[1] Li, G.; Zhu, R.; Yang, Y., Polymer Solar Cells. *Nature Photonics* **2012**, *6*, 153-161.

[2] Wang, Q.; Xie, Y.; Soltani-Kordshuli, F.; Eslamian, M., Progress in Emerging

Solution-Processed Thin Film Solar Cells – Part I: Polymer Solar Cells. *Renewable and Sustainable Energy Reviews* **2016**, *56*, 347-361.

[3] Meng, L.; Zhang, Y.; Wan, X.; Li, C.; Zhang, X.; Wang, Y.; Ke, X.; Xiao, Z.; Ding, L.; Xia, R.; et al., Organic and Solution-Processed Tandem Solar Cells with 17.3% Efficiency. *Science* **2018**, *361*, 1094-1098.

[4] Zhan, L.; Li, S.; Lau, T.-K.; Cui, Y.; Lu, X.; Shi, M.; Li, C.-Z.; Li, H.; Hou, J.; Chen, H., Over 17% Efficiency Ternary Organic Solar Cells Enabled by Two Non-Fullerene Acceptors Working in an Alloy-Like Model. *Energy & Environmental Science* **2020**, *13*, 635-645.

[5] Liu, Q.; Jiang, Y.; Jin, K.; Qin, J.; Xu, J.; Li, W.; Xiong, J.; Liu, J.; Xiao, Z.; Sun, K.; et al., 18% Efficiency Organic Solar Cells. *Science Bulletin* **2020**, *65*, 272-275.

[6] Ganesamoorthy, R.; Sathiyan, G.; Sakthivel, P., Review: Fullerene Based Acceptors for Efficient Bulk Heterojunction Organic Solar Cell Applications. *Solar Energy Materials and Solar Cells* **2017**, *161*, 102-148.

[7] Zhao, J.; Li, Y.; Yang, G.; Jiang, K.; Lin, H.; Ade, H.; Ma, W.; Yan, H., Efficient Organic Solar Cells Processed from Hydrocarbon Solvents. *Nature Energy* **2016**, *1*, 15027.

[8] He, Y.; Li, Y., Fullerene Derivative Acceptors for High Performance Polymer Solar Cells. *Physical Chemistry Chemical Physics* **2011**, *13*, 1970-1983.

[9] He, Y.; Chen, H.-Y.; Hou, J.; Li, Y., Indene−C60 Bisadduct: A New Acceptor for High-Performance Polymer Solar Cells. *Journal of the American Chemical Society* **2010**,

132, 1377-1382.

[10] Nielsen, C. B.; Holliday, S.; Chen, H.-Y.; Cryer, S. J.; McCulloch, I., Non-Fullerene Electron Acceptors for Use in Organic Solar Cells. *Accounts of Chemical Research* **2015**, *48*, 2803-2812.

[11] Zhan, C.; Zhang, X.; Yao, J., New Advances in Non-Fullerene Acceptor Based Organic Solar Cells. *RSC Advances* **2015**, *5*, 93002-93026.

[12] Yuan, J.; Zhang, Y.; Zhou, L.; Zhang, G.; Yip, H.-L.; Lau, T.-K.; Lu, X.; Zhu, C.; Peng, H.; Johnson, P. A.; et al., Single-Junction Organic Solar Cell with over 15% Efficiency Using Fused-Ring Acceptor with Electron-Deficient Core. *Joule* **2019**, *3*, 1140-1151.

[13] Cui, Y.; Yao, H.; Zhang, J.; Zhang, T.; Wang, Y.; Hong, L.; Xian, K.; Xu, B.; Zhang, S.; Peng, J.; et al., Over 16% Efficiency Organic Photovoltaic Cells Enabled by a Chlorinated Acceptor with Increased Open-Circuit Voltages. *Nature Communications* **2019**, *10*, 2515.

[14] Sun, H.; Chen, F.; Chen, Z.-K., Recent Progress on Non-Fullerene Acceptors for Organic Photovoltaics. *Materials Today* **2019**, *24*, 94-118.

[15] Zhang, J.; Tan, H. S.; Guo, X.; Facchetti, A.; Yan, H., Material Insights and Challenges for Non-Fullerene Organic Solar Cells Based on Small Molecular Acceptors. *Nature Energy* **2018**, *3*, 720-731.

[16] Li, Z.; Jiang, K.; Yang, G.; Lai, J. Y.; Ma, T.; Zhao, J.; Ma, W.; Yan, H., Donor Polymer Design Enables Efficient Non-Fullerene Organic Solar Cells. *Nat Commun*

2016, *7*, 13094.

[17] Zhang, K.; Qin, Y.; Li, F.; Yu, L.; Sun, M., Two-Dimensional BDT-Based Wide Band Gap Polymer Donor for Efficient Non-Fullerene Organic Solar Cells. *The Journal of Physical Chemistry C* **2017**, *121*, 19634-19641.

[18] Awartani, Omar M.; Gautam, B.; Zhao, W.; Younts, R.; Hou, J.; Gundogdu, K.; Ade, H., Polymer Non-Fullerene Solar Cells of Vastly Different Efficiencies for Minor Side-Chain Modification: Impact of Charge Transfer, Carrier Lifetime, Morphology and Mobility. *Journal of Materials Chemistry A* **2018**, *6*, 12484-12492.

[19] Cha, H.; Zheng, Y.; Dong, Y.; Lee, H. H.; Wu, J.; Bristow, H.; Zhang, J.; Lee, H. K. H.; Tsoi, W. C.; Bakulin, A. A.; et al., Exciton and Charge Carrier Dynamics in Highly Crystalline PTQ10:IDIC Organic Solar Cells. *Advanced Energy Materials* **2020**, *10*, 2001149.

[20] Holliday, S.; Ashraf, R. S.; Wadsworth, A.; Baran, D.; Yousaf, S. A.; Nielsen, C. B.; Tan, C.-H.; Dimitrov, S. D.; Shang, Z.; Gasparini, N.; et al., High-Efficiency and Air-Stable P3HT-Based Polymer Solar Cells with a New Non-Fullerene Acceptor. *Nature Communications* **2016**, *7*, 11585.

[21] Mori, D.; Benten, H.; Ohkita, H.; Ito, S., Morphology-Limited Free Carrier Generation in Donor/Acceptor Polymer Blend Solar Cells Composed of Poly(3-hexylthiophene) and Fluorene-Based Copolymer. *Advanced Energy Materials* **2015**, *5*, 1500304.

[22] Collado-Fregoso, E.; Hood, S. N.; Shoaee, S.; Schroeder, B. C.; McCulloch, I.;

Kassal, I.; Neher, D.; Durrant, J. R., Intercalated vs Nonintercalated Morphologies in Donor–Acceptor Bulk Heterojunction Solar Cells: PBTTT:Fullerene Charge Generation and Recombination Revisited. *The Journal of Physical Chemistry Letters* **2017**, *8*, 4061-4068.

[23] Etzold, F.; Howard, I. A.; Forler, N.; Cho, D. M.; Meister, M.; Mangold, H.; Shu, J.; Hansen, M. R.; Müllen, K.; Laquai, F., The Effect of Solvent Additives on Morphology and Excited-State Dynamics in PCPDTBT:PCBM Photovoltaic Blends. *Journal of the American Chemical Society* **2012**, *134*, 10569-10583.

[24] Guo, Z.; Lee, D.; Schaller, R. D.; Zuo, X.; Lee, B.; Luo, T.; Gao, H.; Huang, L., Relationship between Interchain Interaction, Exciton Delocalization, and Charge Separation in Low-Bandgap Copolymer Blends. *Journal of the American Chemical Society* **2014**, *136*, 10024-10032.

[25] Clarke, T. M.; Durrant, J. R., Charge Photogeneration in Organic Solar Cells. *Chemical Reviews* **2010**, *110*, 6736-6767.

[26] Yoon, N.; Jeong, J.-Y.; Oh, S.; Song, C. E.; Lee, H. K.; Shin, W. S.; Lee, J.-C.; Moon, S.-J.; Lee, S. K., Effects of Electron-Donating and Electron-Accepting Substitution on Photovoltaic Performance in Benzothiadiazole-Based A–D–A′–D–A-Type Small-Molecule Acceptor Solar Cells. *ACS Applied Energy Materials* **2020**, *3*, 12327-12337.

[27] Xue, X.; Weng, K.; Qi, F.; Zhang, Y.; Wang, Z.; Ali, J.; Wei, D.; Sun, Y.; Liu, F.; Wan, M.; et al., Steric Engineering of Alkylthiolation Side Chains to Finely Tune Miscibility in Nonfullerene Polymer Solar Cells. *Advanced Energy Materials* **2019**, *9*,

1802686.

[28] Hoon Lee, B.; Shim, J.; Kim, G.; Kim, H.; Song, S.; Suh, H.; Lee, K., Homogeneous Bulk Heterojunction Networks via Surface Energy Matching at Polymer/Fullerene Interfaces. *Applied Physics Letters* **2012**, *101*, 083304.

[29] Liu, Y.; Zhao, J.; Li, Z.; Mu, C.; Ma, W.; Hu, H.; Jiang, K.; Lin, H.; Ade, H.; Yan, H., Aggregation and Morphology Control Enables Multiple Cases of High-Efficiency Polymer Solar Cells. *Nature Communications* **2014**, *5*, 5293.

[30] Wang, G.; Eastham, N.; Aldrich, T. J.; Ma, B.; Manley, E. F.; Chen, Z.; Chen, L. X.; Olvera de la Cruz, M.; Chang, R. P. H.; Melkonyan, F. S.; et al., Photoactive Blend Morphology Engineering through Systematically Tuning Aggregation in All-Polymer Solar Cells. *Advanced Energy Materials* **2018**, *8*, 1702173.

[31] Qian, D.; Ye, L.; Zhang, M.; Liang, Y.; Li, L.; Huang, Y.; Guo, X.; Zhang, S.; Tan, Z. a.; Hou, J., Design, Application, and Morphology Study of a New Photovoltaic Polymer with Strong Aggregation in Solution State. *Macromolecules* **2012**, *45*, 9611-9617.

[32] Li, S.; Ye, L.; Zhao, W.; Zhang, S.; Mukherjee, S.; Ade, H.; Hou, J., Energy-Level Modulation of Small-Molecule Electron Acceptors to Achieve over 12% Efficiency in Polymer Solar Cells. *Advanced Materials* **2016**, *28*, 9423-9429.

[33] Fei, Z.; Eisner, F. D.; Jiao, X.; Azzouzi, M.; Röhr, J. A.; Han, Y.; Shahid, M.; Chesman, A. S. R.; Easton, C. D.; McNeill, C. R.; et al., An Alkylated Indacenodithieno[3,2-b]thiophene-Based Nonfullerene Acceptor with High Crystallinity

Exhibiting Single Junction Solar Cell Efficiencies Greater Than 13% with Low Voltage Losses. *Advanced Materials* **2018**, *30*, 1705209.

[34] Huang, C.; Liao, X.; Gao, K.; Zuo, L.; Lin, F.; Shi, X.; Li, C.-Z.; Liu, H.; Li, X.; Liu, F.; et al., Highly Efficient Organic Solar Cells Based on S,N-Heteroacene Non-Fullerene Acceptors. *Chemistry of Materials* **2018**, *30*, 5429-5434.

[35] Cha, H.; Wheeler, S.; Holliday, S.; Dimitrov, S. D.; Wadsworth, A.; Lee, H. H.; Baran, D.; McCulloch, I.; Durrant, J. R., Influence of Blend Morphology and Energetics on Charge Separation and Recombination Dynamics in Organic Solar Cells Incorporating a Nonfullerene Acceptor. *Advanced Functional Materials* **2018**, *28*, 1704389.

[36] Cha, H.; Wu, J.; Wadsworth, A.; Nagitta, J.; Limbu, S.; Pont, S.; Li, Z.; Searle, J.; Wyatt, M. F.; Baran, D.; et al., An Efficient, "Burn in" Free Organic Solar Cell Employing a Nonfullerene Electron Acceptor. *Advanced Materials* **2017**, *29*, 1701156.

[37] Li, H.; Zheng, X.; Wang, X.; Liu, F.; Fu, H., Effect of Chain Curvature on the Performance of Diketopyrrolopyrrole-Based Polymer Solar Cells. *Polymer Chemistry* **2015**, *6*, 6637-6643.

[38] Lee, W.; Kim, G.-H.; Ko, S.-J.; Yum, S.; Hwang, S.; Cho, S.; Shin, Y.-H.; Kim, J. Y.; Woo, H. Y., Semicrystalline D–A Copolymers with Different Chain Curvature for Applications in Polymer Optoelectronic Devices. *Macromolecules* **2014**, *47*, 1604-1612.

[39] Li, Y.; Lee, J.-W.; Kim, M.; Lee, C.; Lee, Y. W.; Kim, B. J.; Woo, H. Y., Regioisomeric Wide-Band-Gap Polymers with Different Fluorine Topologies for Non-

Fullerene Organic Solar Cells. *Polymer Chemistry* **2019**, *10*, 395-402.

[40] Lee, T. H.; Kim, D. H.; Lee, E. J.; Moon, D. K., Significant Impact of Monomer Curvatures for Polymer Curved Shape Composition on Backbone Orientation and Solar Cell Performances. *Journal of Industrial and Engineering Chemistry* **2018**, *65*, 195-204.

[41] Gallaher, J. K.; Prasad, S. K. K.; Uddin, M. A.; Kim, T.; Kim, J. Y.; Woo, H. Y.; Hodgkiss, J. M., Spectroscopically Tracking Charge Separation in Polymer : Fullerene Blends with a Three-Phase Morphology. *Energy & Environmental Science* **2015**, *8*, 2713-2724.

[42] Yi, X.; Peng, Z.; Xu, B.; Seyitliyev, D.; Ho, C. H. Y.; Danilov, E. O.; Kim, T.; Reynolds, J. R.; Amassian, A.; Gundogdu, K.; et al., Critical Role of Polymer Aggregation and Miscibility in Nonfullerene-Based Organic Photovoltaics. *Advanced Energy Materials* **2020**, *10*, 1902430.

[43] Zhang, S.; Qin, Y.; Uddin, M. A.; Jang, B.; Zhao, W.; Liu, D.; Woo, H. Y.; Hou, J., A Fluorinated Polythiophene Derivative with Stabilized Backbone Conformation for Highly Efficient Fullerene and Non-Fullerene Polymer Solar Cells. *Macromolecules* **2016**, *49*, 2993-3000.

[44] Zhang, S.; Qin, Y.; Zhu, J.; Hou, J., Over 14% Efficiency in Polymer Solar Cells Enabled by a Chlorinated Polymer Donor. *Advanced Materials* **2018**, *30*, 1800868.

[45] Park, J.-M.; Kim, D. W.; Chung, H. Y.; Kwon, J. E.; Hong, S. H.; Choi, T.-L.; Park, S. Y., A Stereoregular β-Dicyanodistyrylbenzene (β-DCS)-Based Conjugated Polymer for High-Performance Organic Solar Cells with Small Energy Loss and High Quantum

Efficiency. *Journal of Materials Chemistry A* **2017**, *5*, 16681-16688.

[46] Yi, X.; Gautam, B.; Constantinou, I.; Cheng, Y.; Peng, Z.; Klump, E.; Ba, X.; Ho, C. H. Y.; Dong, C.; Marder, S. R.; et al., Impact of Nonfullerene Molecular Architecture on Charge Generation, Transport, and Morphology in PTB7-Th-Based Organic Solar Cells. *Advanced Functional Materials* **2018**, *28*, 1802702.

[47] Choi, J.; Kim, W.; Kim, S.; Kim, T.-S.; Kim, B. J., Influence of Acceptor Type and Polymer Molecular Weight on the Mechanical Properties of Polymer Solar Cells. *Chemistry of Materials* **2019**, *31*, 9057-9069.

[48] Angmo, D.; Peng, X.; Cheng, J.; Gao, M.; Rolston, N.; Sears, K.; Zuo, C.; Subbiah, J.; Kim, S.-S.; Weerasinghe, H.; et al., Beyond Fullerenes: Indacenodithiophene-Based Organic Charge-Transport Layer toward Upscaling of Low-Cost Perovskite Solar Cells. *ACS Applied Materials & Interfaces* **2018**, *10*, 22143-22155.

[49] Ziffer, M. E.; Jo, S. B.; Liu, Y.; Zhong, H.; Mohammed, J. C.; Harrison, J. S.; Jen, A. K. Y.; Ginger, D. S., Tuning H- and J-Aggregate Behavior in π-Conjugated Polymers via Noncovalent Interactions. *The Journal of Physical Chemistry C* **2018**, *122*, 18860-18869.

[50] Bencheikh, F.; Duché, D.; Ruiz, C. M.; Simon, J.-J.; Escoubas, L., Study of Optical Properties and Molecular Aggregation of Conjugated Low Band Gap Copolymers: PTB7 and PTB7-Th. *The Journal of Physical Chemistry C* **2015**, *119*, 24643-24648.

[51] Namepetra, A.; Kitching, E.; Eftaiha, A. a. F.; Hill, I. G.; Welch, G. C., Understanding the Morphology of Solution Processed Fullerene-Free Small Molecule

Bulk Heterojunction Blends. *Physical Chemistry Chemical Physics* **2016**, *18*, 12476-12485.

[52] Laventure, A.; Welch, G. C., A Tetrachlorinated Molecular Non-Fullerene Acceptor for High Performance near-IR Absorbing Organic Solar Cells. *Journal of Materials Chemistry C* **2018**, *6*, 9060-9064.

[53] Yuan, J.; Xu, Y.; Shi, G.; Ling, X.; Ying, L.; Huang, F.; Lee, T. H.; Woo, H. Y.; Kim, J. Y.; Cao, Y.; et al., Engineering the Morphology via Processing Additives in Multiple All-Polymer Solar Cells for Improved Performance. *Journal of Materials Chemistry A* **2018**, *6*, 10421-10432.

[54] Guo, J.; Ohkita, H.; Benten, H.; Ito, S., Near-IR Femtosecond Transient Absorption Spectroscopy of Ultrafast Polaron and Triplet Exciton Formation in Polythiophene Films with Different Regioregularities. *Journal of the American Chemical Society* **2009**, *131*, 16869-16880.

[55] Cook, S.; Furube, A.; Katoh, R., Analysis of the Excited States of Regioregular Polythiophene P3HT. *Energy & Environmental Science* **2008**, *1*, 294-299.

[56] Wang, C.; Fan, C.; Yuan, C.; Yang, G.; Li, X.; Ju, C.; Feng, Y.; Xu, J., Third- and High-Order Nonlinear Optical Properties of an Intramolecular Charge-Transfer Compound. *RSC Advances* **2017**, *7*, 4825-4829.

[57] Holzer, W.; Penzkofer, A.; Stockmann, R.; Meysel, H.; Liebegott, H.; Hörhold, H. H., Energy Density Dependent Fluorescence Quenching of Diphenyl Substituted Phenylene-Vinylene and Diphenylene-Vinylene Polymers by Exciton–Exciton

Annihilation. *Synthetic Metals* **2001**, *125*, 343-357.

[58] Völker, S. F.; Schmiedel, A.; Holzapfel, M.; Renziehausen, K.; Engel, V.; Lambert, C., Singlet–Singlet Exciton Annihilation in an Exciton-Coupled Squaraine-Squaraine Copolymer: A Model toward Hetero-J-Aggregates. *The Journal of Physical Chemistry C* **2014**, *118*, 17467-17482.

[59] Daniel, C.; Herz, L. M.; Silva, C.; Hoeben, F. J. M.; Jonkheijm, P.; Schenning, A. P. H. J.; Meijer, E. W., Exciton Bimolecular Annihilation Dynamics in Supramolecular Nanostructures of Conjugated Oligomers. *Physical Review B* **2003**, *68*, 235212.

[60] Dimitriev, O. P.; Blank, D. A.; Ganser, C.; Teichert, C., Effect of the Polymer Chain Arrangement on Exciton and Polaron Dynamics in P3HT and P3HT:PCBM Films. *The Journal of Physical Chemistry C* **2018**, *122*, 17096-17109.

[61] Herrmann, D.; Niesar, S.; Scharsich, C.; Köhler, A.; Stutzmann, M.; Riedle, E., Role of Structural Order and Excess Energy on Ultrafast Free Charge Generation in Hybrid Polythiophene/Si Photovoltaics Probed in Real Time by near-Infrared Broadband Transient Absorption. *Journal of the American Chemical Society* **2011**, *133*, 18220-18233.

[62] Eastham, N. D.; Logsdon, J. L.; Manley, E. F.; Aldrich, T. J.; Leonardi, M. J.; Wang, G.; Powers-Riggs, N. E.; Young, R. M.; Chen, L. X.; Wasielewski, M. R.; et al., Hole-Transfer Dependence on Blend Morphology and Energy Level Alignment in Polymer: ITIC Photovoltaic Materials. *Advanced Materials* **2018**, *30*, 1704263.

[63] Lee, J. W.; Bae, S.; Jo, W. H., Synthesis of 6H-benzo[c]chromene as a New

Electron-Rich Building Block of Conjugated Alternating Copolymers and Its Application to Polymer Solar Cells. *Journal of Materials Chemistry A* **2014**, *2*, 14146-14153.

[64] Cowan, S. R.; Roy, A.; Heeger, A. J., Recombination in Polymer-Fullerene Bulk Heterojunction Solar Cells. *Physical Review B* **2010**, *82*, 245207.

[65] Lee, H.; Oh, S.; Song, C. E.; Lee, H. K.; Lee, S. K.; Shin, W. S.; So, W.-W.; Moon, S.-J.; Lee, J.-C., Stable P3HT: Amorphous Non-Fullerene Solar Cells with a High Open-Circuit Voltage of 1 V and Efficiency of 4%. *RSC Advances* **2019**, *9*, 20733-20741.

[66] Kyaw, A. K. K.; Wang, D. H.; Gupta, V.; Leong, W. L.; Ke, L.; Bazan, G. C.; Heeger, A. J., Intensity Dependence of Current–Voltage Characteristics and Recombination in High-Efficiency Solution-Processed Small-Molecule Solar Cells. *ACS Nano* **2013**, *7*, 4569-4577.

[67] Alqahtani, O.; Babics, M.; Gorenflot, J.; Savikhin, V.; Ferron, T.; Balawi, A. H.; Paulke, A.; Kan, Z.; Pope, M.; Clulow, A. J.; et al., Mixed Domains Enhance Charge Generation and Extraction in Bulk-Heterojunction Solar Cells with Small-Molecule Donors. *Advanced Energy Materials* **2018**, *8*, 1702941.

[68] Wu, H.; Fan, H.; Xu, S.; Ye, L.; Guo, Y.; Yi, Y.; Ade, H.; Zhu, X., Isomery-Dependent Miscibility Enables High-Performance All-Small-Molecule Solar Cells. *Small* **2019**, *15*, 1804271.

초 록 (Korean Abstract)

유기반도체 재료는 저비용 제조, 유연성, 화학적 다기능성 등 다양한 장점들로 인해 실리콘 기반 반도체의 대안으로 많은 관심을 이끌었다. 이러한 유기 반도체의 장점들을 바탕으로 다양한 광전자 애플리케이션이 개발됐으며, 이 중 유기 태양전지는 지난 20년 동안 차세대 에너지 전환 유망 소자로 매우 큰 관심을 받아왔다. 유기 태양전지의 구조는 두 전극 사이에 여러 층이 적층된 구조로 구성되어 있으며, 이 중 빛을 흡수하는 광활성층은 고성능 유기 태양전지를 얻기 위한 전자 주개 물질(donor)과 전자 받개 물질(acceptor)의 이종접합구조로 되어있다. 그러므로 유기 태양전지의 작동 과정 중 광활성층의 광 흡수, 전하 전달, 전하 운반 및 재결합과 같은 광유도 공정의 각 단계들은 소자의 효율에 매우 큰 영향을 미치며, 각 공정들은 유기 반도체 물질의 광학적, 전기적 특성, 에너지 레벨 및 전자 주개물질/받개물질 (D/A)의 블렌드 모폴로지 등의 여러 요소에 의해 영향을 받는다.

특히 광활성층 내에서의 광유도 전하 발생은 유기 태양전지의 광전류에 상당한 영향을 미친다. 하지만 이러한 전하 분리 프로세스의 중요성에도 불구하고, 전하 분리의 광물리적 프로세스에 대한 포괄적인 연구가 아직

부족하여, 전하 분리 메커니즘과 태양 전지 성능에 미치는 영향에 대한 분광학적 연구가 필요하다. 따라서, 본 연구에서는 시간 분해 분광법을 이용한 유기 태양전지의 광유도 전하 분리 메커니즘에 대한 광물학적 연구를 수행하여, 다양한 전자 주개, 받개 유기 반도체 물질을 활용해 전하 분리와 그에 따른 소자 성능 등을 연구하였고, 고효율 유기 태양전지 구현에 필요한 재료의 구조적 특성에 대하여 탐구하였다.

먼저 단분자 전자 주개 물질의 전자 주개 및 받개 단위의 효과적인 배열을 확인하기 위해 두개의 triad 전자 주개 물질을 합성하여 분석하였다. 인돌로[3,2-b]인돌(IDID)과 디케토피롤로피롤(DPP)을 각각 전자 주개 및 받개 단위로 사용하는 ADA와 DAD 타입의 triad 전자 주개 물질들을 전자 받개 물질($PC_{61}BM$)와 함께 사용하였으며 유기 태양전지를 구현하였다. ADA와 DAD 는 두 물질 사이의 구조적 차이로 인해 각 단분자 도너 물질과 주변의 물질간의 상호작용으로 인한 대칭성-파괴 전하 이동 특성 또한 차이를 보였다. 결과적으로, ADA 타입의 단분자 주개 물질은 공간적으로 더 비편재화된 LUMO로 인해 더 강한 분자내 전하 이동(ICT) 특성을 보였으며, 이로 인해 D/A 계면에서의 폴라론 생성이 유리해지고 전하 재결합은 억제되어, ADA:$PC_{61}BM$ 소자에서 DAD:$PC_{61}BM$ 소자에 비해 높은 단락회로 전류 (J_{SC})와 높은 전력 변환 효율을 보였다. (제 2장)

다음으로, 잉여 에너지 역할의 관점에서 고분자 태양전지 (PSC)의 전하 분리 메커니즘을 이해하기 위해 push-pull 유형 공중합체 (PTB7)와 단일중합체 (P3HT)을 각각 전자 주개 물질로 사용하여 고결정성 비풀레렌 전자 받개 물질 (NIDCSO3)과 함께 고분자 태양전지를 구현하였다. PTB7은 분자내 전하 이동 특성을 가진 비편재화된 엑시톤을 보였고, 따라서 D/A 계면에서 높은 charge transfer (CT) 준위를 통한 초고속 전하 분리가 전하 생성의 지배적인 경로임을 확인하였다. 반면에 P3HT는 비편재화된 엑시톤을 보이는데, 이로 인해 매우 빠른 시간 내에서 폴라론 쌍 상태로 이완된다. 즉, P3HT:NIDCSEO3의 전하 분리 현상은 폴라론 쌍과 낮은 CT 준위로의 빠른 이완으로 인해 높은 에너지 준위와 낮은 에너지 준위를 통한 전하 생성이 복합적으로 일어나는 시스템을 갖는다. 결과적으로 PTB7:NIDCSEO3 고분자 태양전지는 높은 에너지를 갖는 엑시톤 분리를 통한 전하 생성으로 인해 높은 소자 효율을 보이고, 낮은 CT 상태를 통한 전하 재결합이 억제되어 전하 생성에 유리하여 높은 소자 효율을 보인다. (제 3장)

마지막으로 블렌드 모폴로지 (blend morphology)와 전하 생성 및 재결합의 관점에서 들뜬 상태 동역학을 비교하여, 고효율 유기 태양전지를 구현하기 위한 고분자의 특성과 블렌드 모폴로지의 조건을 확인하였다.

뭉침(aggregation) 특성이 서로 다른 두 개의 push-pull 유형 고분자(PBDCS, PBDS)와 두 개의 전자 받개 (풀러렌형 받개, $PC_{71}BM$, 비풀러렌형 받개, ITIC)를 사용하여 고분자 태양전지에서 고분자의 뭉침 특성이 소자 효율에 미치는 영향을 파악하였다. 블렌드 모폴로지는 고분자의 뭉침 촉진자 (PBDCS의 β-시아노 그룹)의 여부와 받개 물질의 뭉침 및 침투 특성에 따라 크게 달라진다. 그러므로 들뜬 상태의 동역학 및 이에 따른 소자 특성도 전자 주개 및 받개 물질의 화학 구조에 따라 크게 영향을 받는다. PBDCS 기반 고분자 태양전지는 순도 높은 도메인 시스템으로 인해 전하 재결합이 억제되어 PBDCS:$PC_{71}BM$과 PBDCS:ITIC의 고분자 태양전지에서 각각 8.75, 7.81%의 PCE를 보이며 높은 소자 성능을 보였다. 반면, PBDS 기반 고분자 태양 전지는 전자 받개 물질에 따라 들뜬 상태 동역학과 소자 특성이 크게 달라지며 PBDS:$PC_{71}BM$과 PBDS:ITIC 고분자 태양전지에서 각각 5.00, 0.76%의 PCE를 보였다. 특히, PBDS:ITIC 고분자 태양전지는 과도하게된 블렌드 모폴로지로 인해 초고속 전하생성과 함께 전자 재결합이 매우 많이 일어나며 매우 낮은 소자 특성을 보였다. 이러한 결과로 인해 블렌드 모폴로지가 고분자 태양전지의 소자 특성에 매우 중요한 영향을 미치고, 뭉침 특성을 갖는 고분자가 고효율 고분자 태양전지에 이상적인 블렌드 모폴로지를 구현하기에 유리하다는 것을 확인하였다. (제 4장)

주요어: 유기 반도체, 유기 태양전지, 순간 흡수 분광법, 광유도 전하생성, 전하 재결합, 단분자 전자 주개, 고분자 뭉침, 분자내 전하 이동 특성

학생 번호: 2015-30185